The role of magnetic fields in the interstellar medium

Cetin Can Evirgen

Thesis submitted for the degree of
Doctor of Philosophy

School of Mathematics, Statistics & Physics
Newcastle University
Newcastle upon Tyne
United Kingdom

September 2019

Dedecim, keşke sen de görebilseydin benim bu tuhaf hieroglifl erimi...

Acknowledgements

It is a true privilege to be in this position. I want to acknowledge this before I begin to thank those who have supported me throughout the past four years.

I would like to start by thanking my PhD supervisors, Professor Anvar Shukurov, Dr Andrew Fletcher, and Paul Bushby. I have benefited tremendously from your collective wisdom and knowledge, as well as your willingness to allow me to explore the possibilities in a research area that I have enjoyed thoroughly. I would also like to thank my colleague, collaborator and friend Dr Frederick Gent. It has been an honour to continue the work you started, and to have the pleasure of continuing it alongside you. My visits to Finland have been possible, productive and very fun thanks to you, Maija and Maija's lovely family.

I started my PhD a year after two of my friends, who happened to be PhD students in the same research group. Dr James Hollins and Dr Amit Seta, it makes me very proud to be able to refer to your by your proper academic titles. Your friendship and support have been a true joy throughout the years. A particular highlight was when I (and a few other kindred souls) managed to get lost on the French Alps on a particularly foolhardy 'field trip' during the Les Houches conference, and received a text from James saying "Are you alive?". I worry, retrospectively, that some of my conference misadventures may have aged James unduly.

There are a number of lovely people with whom I have shared this experience: Jack Walton, Laura Wadkin, Liam Dobson, Alex Hindle, Jack Kennedy, Rathish Ratnasignam, Robert Bickerton, Francesca Fedele, Sophie Harbisher, Joe Reid, Marios Bounakis, Cameron Williams, Em Rickinson, Dr Thomas Bland, Clarissa Barratt, Hayley Moore, Ryan Doran, Devika Tharakkal, Dimitris Chiotis, Horacio Guerra, Yameng Ji. Thank you for making the experience all the more enjoyable and worthwhile.

I have met a number of postdoctoral researchers who have given me hope that it is possible to survive a PhD; Dr Luiz Rodrigues, Dr Chris Hales, Dr Irina Makarenko, Dr Ilke Canakci, Dr Philipp Edelmann, Dr Sirio Orozco Fuentes. Thank you for the discussions, ideas and for bestowing the hope of survival.

I would like to say a huge thank you to Dr Michael Beaty, John Nicholson and Dr George Stagg for all the help you have given me with the numerous computational challenges (some self-inflicted) that I have faced throughout my studies. I would also like to thank the school office and admin Jackie Martin, Jackie Williams, Helen Green, Lauren Daley, Maria Adair, Lauren Thompson, who work tirelessly to ensure that the ship always runs smoothly.

People sometimes say "last but not least" at this stage. I will have to start with something a little stronger. Last and most certainly the most, I owe an infinite debt of gratitude to my parents Sabri Mertol Evirgen and Amanda Evirgen, and my brothers Selcuk Mert Evirgen and Berker Kaan Evirgen. It is a worn-out phrase but there are truly very few words capable of conveying my feelings as I write this. Suffice to say, this would simply not be possible without your endless love and tireless support.

P.S Mert, it's your turn to enjoy the PhD experience now...

Abstract

The dynamical role of magnetic fields in the interstellar medium (ISM) of galaxies has been widely debated since their discovery approximately seventy years ago. I investigate the possible dynamical role of magnetic fields in the ISM, using numerical simulations of both a region of a spiral galaxy and of individual supernova (SN) explosions. In the galaxy simulations, the magnetic field evolves from a weak seed-field via *dynamo action*, in a manner consistent with the internal gas dynamics of the simulated ISM. I find that the magnetic field, and particularly its coherently-structured large-scale component, evolves spatially in such a way as to avoid the hottest, most violently turbulent regions of the ISM, where SN explosions inject large amounts of energy and produce strong shocks in the surrounding gas. The large-scale magnetic field is especially sensitive to the hot gas, strongly preferring to reside in the more hospitable warm gas.

I also find that the magnetic field produces feedback on the local gas dynamics. The main effect is that large-scale outflows, characterised by the mean vertical velocity of gas which represents gas flowing vertically out of the galactic disc, are damped by magnetic pressure gradient close to the galactic midplane, as the magnetic field becomes dynamically significant. This also effects the vertical distribution of gas density and gas pressure; gas density becomes more homogeneous close to the midplane but decays more strongly, with vertical distance away from the midplane, further away from the midplane. I also find that while the fractional volume of hot gas decreases by up to an order of magnitude from the early to the late stage of the numerical simulation, the hot gas becomes more dense.

Following this, I present results from high-resolution numerical simulations of individual SN remnants to understand possible effects of the magnetic field on the main energy injection mechanism for galaxies. I use models that are purely hydrodynamical (HD) as a baseline for comparison with magnetohydrodynamical (MHD) simulations, to ascertain the effects of magnetic fields. I find that magnetic fields alter both physical and thermodynamical properties of these simulated SN remnants. The remnant shocks propagate faster perpendicular to the magnetic field, resulting from magnetic pressure gradient. Inward momentum injection is also enhanced for

MHD remnants, resulting in mass loss from the shock inwards towards the remnant core. As a result, the remnant core is magnetically confined, which reduces the efficiency of heat loss due to adiabatic expansion. Thus, the hot, diffuse gas in the remnant core remains hotter and becomes more dense throughout the evolution of the remnant. This in agreement with the change to the fractional volume and density of hot gas found in the larger-scale simulations of the ISM presented in this Thesis.

Contents

List of Figures

List of Tables

Part I

Introduction

Chapter 1

Introduction

1.1 Motivation

The aim of my doctoral research has been to understand the dynamical role of magnetic fields within spiral galaxies, such as the Milky Way or M51. Some important outstanding questions are:

I. By what process are galactic magnetic fields generated?

II. What is the likely spatial configuration of dynamically significant large-scale galactic magnetic fields?

III. What are the main transport processes for galactic magnetic fields?

IV. Do magnetic fields have a feedback effect on interstellar gas dynamics? Is it possible for galactic winds to be altered by the presence of a dynamically significant magnetic field?

V. How are, if at all, supernova remnants affected by large-scale magnetic fields?

These questions are central to the motivation behind this work. I hope that the results, and subsequent discussion, presented here might provide valuable contributions to the ongoing debate. The analysis is based predominantly on numerical simulations of the ISM, which feature a number of essential physical processes conducive to the evolution of magnetic field up to micro gauss strengths from a nano gauss seed field, via *dynamo action*. These numerical simulations aim to model in-

terstellar physics as realistically as possible with existing computational resources. However, even the most sophisticated supercomputers are still not capable of modelling such a complicated physical and chemical system required for robust, one-to-one comparison with real galaxies. Therefore, it is perhaps better to view results from such simulations as qualitative physical effects which one might expect to observe in *real* physical systems, such as spiral galaxies. The key aspect of these results is the analysis of a numerical simulation in which magnetic fields are initially dynamically insignificant but gradually become dynamically significant through the self-consistent amplification of the magnetic field. The changes to the simulated ISM are essential to isolating possible dynamical effects of magnetic fields.

1.2 Thesis structure

1.2.1 Overview

In the remainder of this Chapter, I introduce physical concepts which underpin the work presented in the Thesis, and aim to provide context for the results.

In Chapter 2, I provide an overview of relevant numerical studies of the ISM and its various dynamical processes. I aim to provide details on processes which are particularly relevant to the questions considered in this Thesis. In addition, details of the ISM simulations used for this Thesis are also provided in this chapter.

Chapter 3 explores effects of interstellar gas dynamics, particularly hot gas structures, on the spatial configuration of the large-scale magnetic field in a simulation of the ISM, with particular reference to the distribution of the magnetic field within the multi-phase structure of the ISM.

Chapter 4 focuses on the 'other side of the coin': whether a *dynamo-evolved* magnetic field has a back-reaction on interstellar gas dynamics. This chapter focuses particularly on how the multi-phase and vertical structure of the galactic disc is affected by the magnetic field in the simulated ISM.

In Chapter 5, I delve further into effects of a large-scale magnetic field on hot gas in the ISM. I present analysis of numerical simulations of individual supernova explosions (SNe).

I present a summary of conclusions, with a discussion of possible improvements and an outline of plans for future work in Chapter 6.

Appendix A extends the discussion presented in the previous chapter by introducing random magnetic fields into the SNe simulations. However, the results presented in this chapter are preliminary and require further analysis and checks. It has been included as an appendix, instead of a main chapter, for this reason.

Appendix B provides a comparison of two important averaging methods: Gaussian smoothing and horizontal averaging. Simulation data is used to illustrate then differences.

In Appendix C, I present a derivation of the horizontally averaged momentum equation used in Chapter 4.

I discuss the method I use to calculate the time profile of SN radii, and subsequently the SN shock velocity, in Appendix D.

In Appendix E, I discuss the effects of physical parameters on the evolution of SN remnants in numerical simulations presented in Chapter 5.

1.2.2 Publications

Chapter 3

The results presented in this chapter were published in the Monthly Notices of the Royal Astronomical Society (MNRAS), with full details given below:

Evirgen, C. C., Gent, F. A., Shukurov, A., Fletcher, A. & Bushby, P. 2017 *The distribution of mean and fluctuating magnetic fields in the multiphase interstellar medium.* MNRAS 464, L105-L109.

Chapter 4

The results presented in this chapter were published in the Monthly Notices of the Royal Astronomical Society (MNRAS), with full details given below:

Evirgen, C. C., Gent, F. A., Shukurov, A., Fletcher, A. & Bushby, P. J. 2019 *The supernova-regulated ISM - VI. Magnetic effects on the structure of the interstellar*

medium. MNRAS 488 (4), 5065-5074.

A part of these results were also presented in:

Proceedings of FM8 "New Insights in Extragalactic Magnetic Fields", XXXth General Assembly of the IAU, Vienna, August 20-31, 2018.

The text for this is available on arXiv, with the following details:

Shukurov, A., Evirgen, C. C., Fletcher, A., Bushby, P. J. & Gent, F. A. 2018 Magnetic field effects on the ISM structure and galactic outflows. arXiv e-prints p. arXiv:1810.01202

Chapter 5

The results presented in this chapter are curently under review with the Astrophysical Journal (ApJ). The details are given below:

Evirgen, C. C. & Gent, F. A. 2019 MHD supernova explosions Large-scale magnetic field effects. arXiv e-prints p. arXiv:1908.08781.

Appendix B

I have contributed Section 7 to the following manuscript, which is currently in preparation for submission to Astronomy & Astrophysics (A&A):

J.F. Hollins, G. R. Sarson, C. C. Evirgen, A. Shukurov, A. Fletcher & F. A. Gent, (in prep.) *Mean fields and fluctuations in simulations of a compressible interstellar medium*

1.3 The multi-phase interstellar medium (ISM)

The interstellar medium (ISM) refers to the space within galaxies surrounding stars. While the ISM contains only $\sim 10\%$ of galactic mass (Ferrière, 2001), it plays a vital role in galactic dynamics. Particularly dense and cold clouds of molecular gas provide an environment suitable for star formation. Meanwhile, dying stars and

supernova explosions inject momentum into the surrounding ISM and drive turbulence. Enriched material, deposited by dying stars, also play an important role in formation of planetary systems (Klessen & Glover, 2016). The current understanding is that the ISM hosts and regulates a number of important physical processes occuring in the galaxy.

The overall picture which has been uncovered since the 1900s, is that the ISM is a highly inhomogeneous medium, in terms of gas density and temperature (Ferrière, 2001; Klessen & Glover, 2016). It is also considered a 'multi-phase' gaseous medium, in that it comprises a number of characteristically distinct types of gas. These phases have gas densities ranging from dense 10^{-18} g cm^{-3} to very diffuse 10^{-28} g cm^{-3} gas, with typical temperatures ranging from $T \sim 10 - 100\,\mathrm{K}$ to $T \sim 10^6\,\mathrm{K}$, respectively. The generally accepted view of the multi-phase structure is that there are three distinct phases:

- Dense cold molecular gas clouds with typical temperatures of $T \sim 10^2\,\mathrm{K}$ and number density 10 – $1000\,\mathrm{cm}^{-3}$. These molecular clouds contain a large fraction of the total mass of interstellar gas, despite occupying a negligible fraction of the total volume. They play a key role in star formation (Kalberla & Kerp, 2009).
- Warm gas has typical temperatures of order $T \sim 10^4\,\mathrm{K}$ and number densities in the range $0.1 - 1\,\mathrm{cm}^{-3}$.
- Hot gas typical temperatures of order $T \sim 10^6\,\mathrm{K}$ and number densities typically in the range $0.001 - 0.01\,\mathrm{cm}^{-3}$. Energy and hot gas is typically injected into the ISM by SNe and stellar winds Mac Low & Klessen (2004).

Within this gaseous medium, there are also magnetic fields, which pervade the galaxy, and cosmic rays which are dynamically coupled to the magnetic fields. It is generally accepted that kinetic (or turbulent) motions, magnetic fields and cosmic rays are in energy equipartition globally. This suggests that all ingredients play a role in galactic dynamics. Much work has been carried out on developing an understanding of interstellar dynamics, which presents both a technical and theoretical challenge on physical and time scales which span from the molecular to the galactic. Much of the progress has been due to rapid developments in observational astronomy since the 1900s (Ferrière, 2001), with theory developing alongside to enable interpretation of observations. The more recent development, particularly over the

last two decades, of sophisticated three-dimensional numerical simulations (Caunt & Korpi, 2001; Mac Low & Klessen, 2004; de Avillez & Breitschwerdt, 2005; Gressel *et al.*, 2008; Gent, 2012; Gressel *et al.*, 2013; Bendre *et al.*, 2015; Walch *et al.*, 2015; Girichidis *et al.*, 2016; Gatto *et al.*, 2017; Li *et al.*, 2017, 2019) have enabled further testing of theory and observations.

1.4 Galactic magnetic fields

Galactic magnetic fields are present at most physical scales, and their energies are comparable to thermal, kinetic and cosmic ray energies. Even though this suggests that magnetic fields are dynamically important, there remain a number of important unanswered questions. In this Section, I present a brief overview of the contemporary understanding of the dynamical role played by magnetic fields in spiral galaxies, with reference to theory and observational evidence.

1.4.1 Observational evidence

The first observational discovery of galactic magnetic fields originates from *stellar polarimetry*, which interprets the polarisation of starlight by interaction with interstellar dust grains. This has been used to infer that the large scale magnetic field is largely parallel to the galactic midplane. Moreover, the magnetic field was found to be at an 7.2° inclination angle to the azimuthal direction (Heiles, 1996).

A typical spiral galaxy, as seen in Figure 1.1, comprises a 'flattened' disk with a central spherical bulge, and a galactic halo, comprised of gas outflows which eventually fall back towards the galaxy under the gravitational force. The flattened, quasi two-dimensional, structure of the disc is inherently connected to rotation of the disc. Consequently, these observations also evidence a connection between differential rotation and the galactic magnetic field.

Observations of *synchotron polarisation* are used to make inferences regarding the strength and structure of galactic magnetic fields, by using polarised radio emissions from cosmic ray (CR) electrons spiralling around magnetic fields (Beck, 2007). Studies of synchotron polarisation have shown that

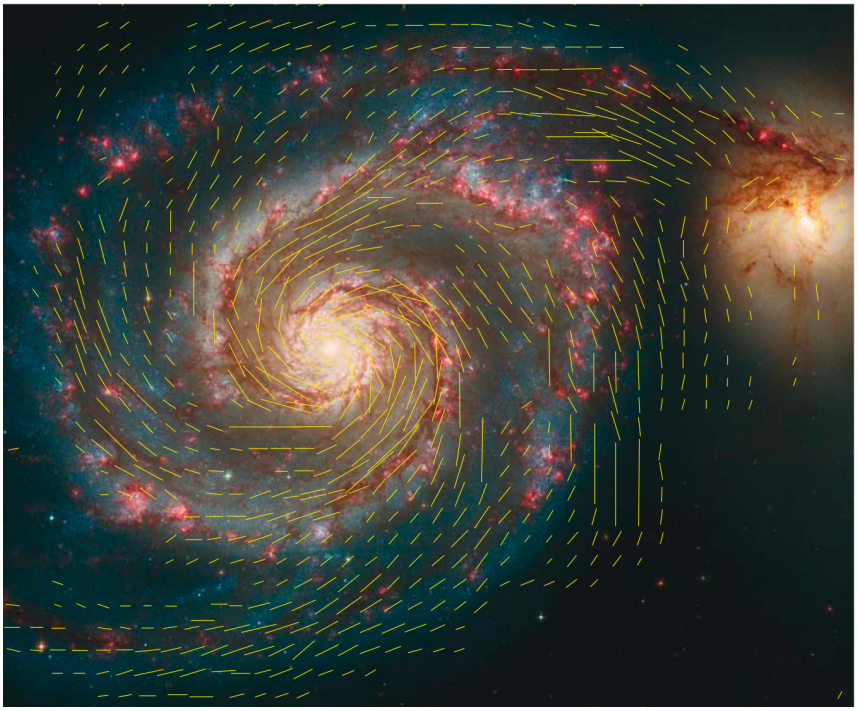

Figure 1.1: The M51 (Whilrpool) galaxy. The background optical image comes from the Hubble Space Telescope Space Science Team, while the magnetic field lines are from radio polarization observations made with the Very Large Array. The image is taken from Fletcher *et al.* (2011*a*).

1. Galactic magnetic fields have strengths ranging from the order of a few microgauss to tens of microgauss (Klein *et al.*, 1988; Niklas, 1995; Chyży & Beck, 2004; Fletcher *et al.*, 2004, 2011*b*; Mao *et al.*, 2017).

2. Magnetic energy density is comparable to thermal, turbulent and CR energy densities (Boulares & Cox, 1990; Beck, 2007).

3. Galactic magnetic fields have been found to have coherent, large-scale structure at a kiloparsec scale, as well as a random (or tangled), small-scale component. The small-scale field is often strongest in the spiral arms of the galaxy, while the large-scale field is often strongest in the interarm regions (Beck, 2015).

4. Magnetic field strength decays slowly with galactocentric radius, particularly compared with rotational energy density. Subsequently, magnetic fields can affect local rotation curves far away from the galactic centre (Elstner *et al.*, 2014).

1.4.2 Origins

The origin of galactic magnetic fields has been a widely debated topic since the discovery of interstellar magnetic fields approximately 70 years ago. The debate features two competing theories: *primordial* and *dynamo-evolved* magnetic fields.

Primordial field theory proposes that proto-galaxies inherit primordial magnetic fields, which existed in the early Universe, and that these fields are amplified rapidly through compression as matter collapses gravitationally during the formation of the galaxy. This theory produces estimates of magnetic field strength up to two orders of magnitude larger than those observed in galaxies (Ferrière, 2005). Proponents of primordial theory have suggested magnetic diffusion to explain the difference between prediction and observation. However, this requires the assumption that diffusion is strongly anisotropic, and much more efficient parallel to the field. It is unclear that such an assumption is physically motivated. Under the assumption of isotropic magnetic diffusion, we would not expect to observe large-scale, coherently structured magnetic fields in the galactic plane. The worst-case scenario would be complete decay of the galactic magnetic field (Rosner & Deluca, 1989). Kulsrud & Zweibel (2008, (see Chapter 15) discuss the possibility of a magnetic field (strong enough to be considered a pre-galactic field) being generated in proto-galaxies but they note that this is more important as a 'starting point' for the dynamo process, as opposed to a full explanation for the fully-evolved strength or structure of galactic magnetic fields.

An additional difficulty with this theory is that the amplification mechanism proposed would produce spiral structures wound much more tightly than in observed galaxies (Widrow, 2002). Widrow (2002) suggests that in the absence of a feasible *ab initio* galactic magnetic field theory, it is more likely that the field is generated continuously.

It is possible that seed-fields within galaxies could be primordial (Durrer & Neronov, 2013). However, seed fields can originate from other processes, such as the Weibel instability later in cosmological structure formation (Lazar *et al.*, 2009), by plasma fluctuations in protogalaxies (Schlickeiser & Felten, 2013), or by jets produced by early black holes (Rees, 2005).

These seed-fields can be amplified efficiently by turbulent flows driven by SNe

(Ferrière, 1996) or spiral shocks (Kim *et al.*, 2006) by the *small-scale dynamo*, which is capable of amplifying the (weak) seed-fields up to a strength of several micro gauss within a time scale of order 10^8 years (Kulsrud *et al.*, 1997; Beck *et al.*, 2012; Rieder & Teyssier, 2016). This produces a turbulent (or disordered) magnetic field. The evolution of the large-scale, ordered magnetic field takes longer, up to a few giga years (Beck *et al.*, 1994; Arshakian *et al.*, 2009; Rodrigues *et al.*, 2015). Numerical simulations have shown that differential rotation and SN-driven turbulence (Ferrière, 1996) can produce such magnetic fields (Gressel *et al.*, 2008; Wang & Abel, 2009; Kotarba *et al.*, 2009; Gent, 2012; Pakmor *et al.*, 2017).

This leads to the more plausible theory that primordial magnetic fields may seed physical processes which amplify magnetic field strength as the galaxy evolves. *Dynamo* theory proposes that random, turbulent motions and differential rotation of the galactic disk leads to the amplification of the primordial seed field consistently with the gas dynamics of the galaxy.

1.4.3 Dynamo action

As the primary focus of this Thesis is the potential effect of dynamo-evolved magnetic field on interstellar gas dynamics and hot gas structures, I discuss dynamo theory very briefly. Comprehensive discussions of this important topic are provided in a number of works (Steenbeck *et al.*, 1966; Moffatt, 1978; Ruzmaikin *et al.*, 1989; Krause & Wielebinski, 1991; Kulsrud, 1999). The governing equation for the dynamo process is

$$\frac{\partial \boldsymbol{B}}{\partial t} = \nabla \times (\boldsymbol{v} \times \boldsymbol{B}) + \eta \nabla^2 \boldsymbol{B} \tag{1.1}$$

where $\boldsymbol{B}$ is the magnetic field, $\boldsymbol{v}$ is the velocity field and η is the magnetic resistivity. The first term on the RHS of Equation (1.1) describes the effect of gas motions, and the interaction of gas motions with the magnetic field, on the evolution of the magnetic field. The second term describes diffusion of the magnetic field. The relative importance of either term can be established using typical or characteristic values for the magnetic field strength B_0, velocity U and length scale of the system L, and expressed as

$$\mathcal{R}m = \frac{|\nabla \times (\boldsymbol{v} \times \boldsymbol{B})|}{|\eta \nabla^2 \boldsymbol{B}|} \sim \frac{(UB_0)/L}{\eta B_0/L^2} = \frac{UL}{\eta},$$

where $\mathcal{R}m$ is the magnetic Reynolds number. Large $\mathcal{R}m$ indicates that interaction with gas motions is the dominant term, or that the magnetic field has become 'frozen-in' to the flow, whereas small $\mathcal{R}m$ shows that magnetic diffusion is dominant. Klein & Fletcher (2015) show that characteristic values of U, L and η for a spiral galaxy predict $\mathcal{R}m \sim 10^8$ and $\mathcal{R}m \sim 10^{11}$ for turbulent and large-scale coherent magnetic fields, respectively. In both cases, we expect the magnetic field to be frozen-in to the gas flow, which means that the spatial configuration and topology of the magnetic field is likely to be heavily influenced by gas motions. However, Klein & Fletcher (2015) also state that magnetic diffusivity will become significant on smaller scales, and that topological re-organisation of the magnetic field can only take place in the case of non-zero magnetic diffusivity.

Mean-field dynamo equation

As discussed previously, galactic magnetic fields have both a large-scale and turbulent magnetic field structure, denoted by $\boldsymbol{B_0}$ and $\boldsymbol{b}$, such that $\boldsymbol{B} = \boldsymbol{B_0} + \boldsymbol{b}$. The velocity field can be represented as a sum of two components in a similar manner, $\boldsymbol{v} = \boldsymbol{V} + \boldsymbol{u}$, where $\boldsymbol{V}$ and $\boldsymbol{u}$ are the large-scale and turbulent gas flows, respectively. There are a number of methods for separating the large and small-scale part of such fields but discussion of these methods is deferred for now. It can be shown that the mean-field (or large-scale) dynamo equation is

$$\frac{\partial \boldsymbol{B_0}}{\partial t} = \nabla \times (\boldsymbol{V} \times \boldsymbol{B_0}) + \nabla \times \boldsymbol{\varepsilon} + \eta \nabla^2 \boldsymbol{B_0}, \tag{1.2}$$

where $\boldsymbol{\varepsilon} = \langle \boldsymbol{u} \times \boldsymbol{b} \rangle$ is the electromotive force, and $< \cdot >$ refers to the averaging method used to separate the large-scale component of a field from the small-scale component[1]. The first term on the RHS describes the effect of interactions between the large-scale velocity and magnetic field terms. In a spiral galaxy, this is typically due to differential rotation of the galaxy and subsequent large-scale shear. Systematic large-scale gas flows such as galactic winds or superbubbles can also

[1]For example, $\boldsymbol{B_0} \equiv \langle \boldsymbol{B} \rangle$

have an effect on dynamo action. The second term represents the effect of interactions between turbulent flows and the small-scale magnetic field on the evolution of the large-scale magnetic field, whilst the third term refers to the diffusion of the large-scale magnetic field.

The most remarkable aspect of this equation is that the evolution of the large-scale dynamo depends on both large-scale and small-scale gas motions. While it is physically remarkable that motions chaotic and tangled up on a much smaller scale can produce ordered magnetic fields, it also poses an interesting challenge in modelling the large-scale dynamo within the galactic context. A simulation which focuses on the large-scale dynamics of the galaxy is unlikely to have the spatial resolution to capture turbulent effects on the mean-field dynamo, which occur at much smaller scales; a simulation which focuses on the small-scale dynamics is unlikely to capture important large-scale processes such as differential rotation.

Stages of dynamo action

In the early stages of dynamo action, known as the *kinematic* stage, the magnetic field will not be strong enough to have a dynamical effect on gas flow through the Lorentz force. In this stage, the magnetic field will grow exponentially. However, as the magnetic field strength increases, the Lorentz force will start to become dynamically significant, creating a magnetic back-reaction on gas flows, and slowing down magnetic field growth until the field strength reaches a statistically steady state. This phase is known as the *non-linear* or *saturated* phase of dynamo action.

The α effect and turbulent diffusivity

There are two important aspects of dynamo action which arise from analysis of the electromotive force (EMF). Klein & Fletcher (2015) show, using a first-order smoothing approximation, that the EMF can be expressed as a sum of two terms:

$$\langle \boldsymbol{u} \times \boldsymbol{b} \rangle = \alpha_{ij} \boldsymbol{B_0}_{,j} - \eta_{ijk} \frac{\partial \boldsymbol{B_0}_{,k}}{\partial x_j}. \tag{1.3}$$

In the case of isotropic turbulence, we have

$$\alpha_{ij} = \alpha\delta_{ij}, \quad \alpha = -\frac{\tau}{3}\left\langle \boldsymbol{b} \cdot (\nabla \times \boldsymbol{u}) \right\rangle,$$

and

$$\eta_{ijk} = \eta_T \epsilon_{ijk}, \quad \eta_T = \frac{\tau}{3}\left\langle \boldsymbol{u}^2 \right\rangle.$$

Here, δ_{ij} is the Kronecker delta, ϵ_{ijk} is the Levi-Civitta tensor, and τ is the turbulent eddy turnover time.

The α-effect refers to how stratification of the gas and rotation of the disc combine to produce non-zero average helicity of turbulence. Physically, this effect can be summarised by considering a parcel of buoyant gas in the galactic disc. As it rises, moving away from the midplane, it will advect magnetic field lines. A straight magnetic field would would be distorted and 'warped' around the rising parcel of gas. Then, Coriolis force induced by rotation will twist this magnetic field line, producing the α-effect.

Klein & Fletcher (2015) further re-write the mean-field dynamo equation as

$$\nabla \times \langle \boldsymbol{u} \times \boldsymbol{b} \rangle = \nabla \times (\alpha \boldsymbol{B_0}) + \eta_T \nabla^2 \boldsymbol{B_0},$$

which shows the role of turbulent diffusion in in the diffusion of the large-scale magnetic field.

Saturation of the mean-field dynamo

There is a dimensionless parameter called the Dynamo number, $\mathcal{D} = \mathcal{R}_\alpha \mathcal{R}_\Omega$, where

$$\mathcal{R}_\alpha = \frac{\alpha_0 h}{\eta_T}, \quad \mathcal{R}_\Omega = \frac{\Omega_0 h^2}{\eta_T}.$$

Here, α_0 and Ω_0 are characteristic values of the alpha-effect and angular velocity, h is the scale height of the galactic disc, and η_T is the turbulent diffusivity as previously introduced. Klein & Fletcher (2015) show that the critical dynamo number, $\mathcal{D}_c$, close to the Solar neighbourhood of the Milky Way is of the order of 10.

If the dynamo number exceeds the critical value, magnetic field strength will grow exponentially. However, as previously discussed, as the magnetic field becomes

stronger, the Lorentz force become dynamically significant. Therefore, we cannot expect the magnetic field strength to grow in an unbounded manner, and it must reach an equilibrium strength at which it begins to self-regulate. This stage is called non-linear since the presence of the magnetic term in both the induction and momentum equation cannot be considered dynamically insignificant. Once the magnetic field strength becomes large enough, gas flows will not solely determine the evolution of the magnetic field (neither in terms of spatial configuration nor in terms of strength); the magnetic field will be strong enough to have a back-reaction on gas flows, thus altering gas flows directly and itself indirectly.

One mechanism that has been proposed for the saturation of the dynamo is called "α-quenching":

$$\alpha = \frac{\alpha_0}{1 + B^2/B_{\mathrm{eq}}^2},$$

where $B_{\mathrm{eq}^2} = 4\pi\rho u^2$ is the equipartition magnetic field strength.

Small-scale magnetic fields and the Fluctuation Dynamo

The ISM contains random magnetic fields with much smaller correlation scales than the large-scale magnetic field. There are two possible mechanisms which produce small-scale fields: tangling up of large-scale scale magnetic fields or by random stretching of magnetic field lines by turbulent flows (Klein & Fletcher, 2015).

Klein & Fletcher (2015) further outline two important aspects:

1. As the growth time of the fluctuation dynamo is of the order of turbulent eddy turnover time, the growth rate of the small-scale field is up to two orders of magnitude faster than the large-scale dynamo.

2. Small-scale fields generated by the fluctuation dynamo will have an intermittent structure, whereas tangling up of the large-scale field will produce small-scale fields uniformly distributed in space.

Chapter 2

Review of numerical simulations of the ISM

2.1 Overview of numerical models of the interstellar medium

Physical processes in the ISM occur over a large range of spatial and temporal scales. These processes play an important role in galactic dynamics. Recent developments in numerical simulations have advanced our understanding significantly.

These simulations can be useful for a number of purposes: we can test existing theory and assumptions, develop a deeper understanding of observational data, and investigate the effects of subsets of physical processes. As with all tools, numerical simulations have limitations. Subsequently, it is crucial to maintain a clear vision of both the capabilities and limitations of a numerical model, as well as the physical motivation for running a numerical simulation.

In this Thesis, the primary motivation is to develop an understanding of the role played by magnetic fields in the vertical and multi-phase structure of spiral galaxies, particularly relating to the structure of the disc. This requires analysis of the dynamical coupling between the magnetic field and velocity field, which is included explicitly in the MHD equations. Given the non-linearity of the dynamical coupling, it is necessary to explore both the effects of gas flows on magnetic fields, and magnetic feedback on gas dynamics. These topics are explored using both simulations of

the local galaxy and individual supernova remnants (SNr) in a magnetised medium, hereafter referred to as ISM models and SNr models, for ease of distinction. In this Section, I provide a summary and discussion of existing numerical models, and how results presented in this thesis fit into the bigger picture.

2.1.1 Physical ingredients of interstellar modelling

The complexity of interstellar physics, and the accompanying numerical challenge, demands a pragmatic approach to numerical interstellar modelling. This work aims to pose a clear question and determine the physical processes essential to understanding the question. Since the various physical processes have spatial and time scales varying over many orders of magnitude, it is not numerically possible to model processes at every dynamically significant scale directly in a single numerical model. This requires either a simplifying assumption, relevant sub-grid model, or exclusion of a physical process where appropriate.

In this work, the central topic is the dynamical role of a magnetic field which has evolved in a self-consistent manner, coupled dynamically to the interstellar gas in a spiral galaxy. In this section, an overview of physical processes required for interstellar modelling is presented. In addition to a general overview, I outline processes of particular significance to the central topic, and provide general information on their numerical implementation. I also discuss processes which have been excluded from the numerical models, with a focus on the physical justification for exclusion.

Supernova explosions

Supernova explosions (SNe) play a significant role in galactic dynamics. They provide pressure support and inject energy, driving turbulence and large-scale outflows (McKee & Ostriker, 1977; Chevalier & Clegg, 1985; Mac Low & Klessen, 2004; Murray *et al.*, 2005; Girichidis *et al.*, 2016). Isolated SNe can significantly impact their local ambient environment, whether evacuating or fragmenting a dense molecular cloud from within, or expansion into, and advection through, less dense hot gas regions. Clusters of SNe can form larger hot gas structures (superbubbles or chimneys), spanning typically hundreds of parsecs, and feeding the galactic fountain.

Both individual SNe and SNe clusters, such as superbubbles arising from OB associations, have been studied analytically (Taylor, 1950; Sedov, 1959; Tomisaka *et al.*, 1981; Cioffi *et al.*, 1988) and numerically (Chevalier, 1974; Ferrière *et al.*, 1991; Slavin & Cox, 1992; Jun & Norman, 1996; Tomisaka, 1998; Caunt & Korpi, 2001; Hanayama & Tomisaka, 2006; Zirakashvili & Ptuskin, 2008; Kim & Ostriker, 2015; Yadav *et al.*, 2017). SNe evolution is spherically symmetric in a non-magnetized uniform ambient ISM (Spitzer, 1978; Cioffi *et al.*, 1988).

In our ISM model, each supernova explosion (SNe) injects 10^{51} erg of energy at the explosion site, with the energy distributed within a spherical region around the explosion site. The radius of the site is chosen large enough to ensure that velocity and temperature gradients can be resolved, in order to avoid numerical instabilities while simultaneously being small enough such that the remnant is still within the Sedov-Taylor, or at most the early snowplough phase. In practice, this usually requires a sphere radius spanning 4-6 points on the uniform simulation grid. Another consideration is loss of energy due to radiative cooling prior to shell formation. This can happen if the injection site satisfies the previously mentioned criteria but remains small enough to feature high temperatures (typically $T \sim 10^8$ K). Joung & Mac Low (2006) solve this issue by adjusting the injection site radius to ensure a minimum mass is contained within the injection site ($60 M_\odot$).

The energy injection is fully thermal if the remnant is still within the adiabatic expansion phase. If the remnant is in the early pressure-driven phase, then a proportion of the energy injection comprises kinetic energy, following (Simpson *et al.*, 2015). Energy injection by SNe in our simulations is discussed further in Gent (2012) and Hollins *et al.* (2017*b*).

Rotation

Differential rotation of spiral galaxies, with shear, lead to spiral arm structures. The coherent large-scale structure of the galactic magnetic field is strongly aligned with the spiral arms. Thus, if the large-scale structure is to evolve in a self-consistent manner, rotation and shear are essential processes. Many adaptive mesh refinement (AMR) codes do not implement large-scale shear. Indeed, if the main interest in understanding gas density and temperature distributions in the ISM, differential rotation is not necessary. Kim *et al.* (2001); Mac Low *et al.* (2005*a*,*b*); Wood

et al. (2010); Hill *et al.* (2012); Girichidis *et al.* (2016) explore the gas density and temperature distributions and structures in the simulated ISM without inclusion of differential rotation.

In terms of magnetic fields in galaxies, and particularly with reference to dynamo-evolved magnetic fields, differential rotation is an essential ingredient. Gressel *et al.* (2008) finds no dynamo action with solid body rotation. In contrast, with differential rotation, they are able to evolve a micro gauss strength field from a nano gauss seed field, via dynamo action.

A number of local ISM simulations, which do not implement differential rotation, circumvent the absence of dynamo action by using *a priori* assumptions about the strength and configuration of the fully-evolved magnetic field (de Avillez & Breitschwerdt, 2004; Mac Low *et al.*, 2005*a*; de Avillez & Breitschwerdt, 2005; Hill *et al.*, 2012; Girichidis *et al.*, 2016). A typical configuration for such models is the use of a micro gauss strength field with a physical configuration uniform parallel to the galactic disk and decaying with gas density vertically away from the mid-plane[1]. While this *a priori* configuration may seem reasonable, it is not clear that simulating the galaxy with such a magnetic field as an initial condition is quite the same as a magnetic field which has evolved, both in strength and spatial configuration, self-consistently and coupled with the gas dymamics of the galaxy. This topic is discussed by Cox (2005), with a particular focus on explaining the pressure and vertical distribution that the ISM has. The author outlines the possibility of feedback from the dynamo process on large-scale gas motions, and further discusses the role of magnetic fields and cosmic rays. Perhaps the most important aspect is the admission that there is no clear consensus on the question of why the ISM has the pressure and vertical distribution that it does.

Indeed, this absence of consensus is apparent within the context of numerical models of the ISM. Whilst some argue that magnetic field have no clear impact on thermal pressure (Mac Low *et al.*, 2005*a*), galactic outflows (Girichidis *et al.*, 2016) or fractional volumes of hot gas (de Avillez & Breitschwerdt, 2005), Bendre *et al.* (2015) finds that magnetic fields do affect vertical velocity. Indeed, suggestions that magnetic fields play a dynamical role were made by Vazquez-Semadeni *et al.* (1995), who found that HII regions did not expand as freely as in purely hydrodynamical simulations, due to magnetic effects. Moreover, magnetic fields control the propagation of

[1]Typically $B(z) \propto \sqrt{n(z)}$, where n is gas number density.

Cosmic Rays (CRs) which provide an additional pressure term in equipartition with (or at least comparable to) other gas pressure terms. Birnboim *et al.* (2015) show that magnetic field and CR pressure regulates the star formation rate. Hanasz *et al.* (2013) also finds that the combination of magnetic and CR pressure can drive fast outflows of hot gas; such outflows, particularly in starburst galaxies, are capable of magnetizing the intergalactic medium (IGM) (Bertone *et al.*, 2006).

One of the key simplifying assumptions made in numerical models which impose a strong initial magnetic field is that magnetic fields are secondary to understanding thermodynamic aspects of the simulated ISM, such as the multi-phase structure. In other words, the magnetic field acts as a *passenger* in large-scale gas dynamics. However, in addition to the aforementioned effects of the magnetic field, Wiener *et al.* (2013) find that CR propagating along magnetic fields lines could heat warm ionized gas. It is plausible that magnetic fields, on vertical and multi-phase structure of the ISM, is subtle and non-linear.

Under these circumstances, it seems more robust to allow the magnetic field to evolve from a weak seed-field, via dynamo action, consistently with the gas dynamics within the simulation, even though this increases the simulation run-time significantly. A possible compromise solution is the use of magnetic field strength and spatial configuration obtained from large-scale dynamo simulations as an initial condition for the magnetic field in numerical models which exclude differential rotation. If this produces the same (or similar) qualitative results, then this leads to a significant reduction in computational cost, since the large-scale dynamo process is expected to evolve on time scales of order $100 - 1000\,\mathrm{Myr}$.

Self-gravity

Hunter *et al.* (1986) and Elmegreen (1993) have both suggested that dense molecular clouds can form from converging, turbulent self-gravitational gas streams. However, the simulations of Nordlund & Padoan (2003) have shown that such dense clouds can form from intersecting shocks in the ISM. While self-gravity will accelerate formation of high-density structures in the ISM, other physical processes, such as thermal instability, also play a role. However, Brandenburg *et al.* (2007) and Slyz *et al.* (2005) find separately that the effects of turbulence and compression are dominant at higher resolutions.

Within the context of large-scale ISM simulations, it is not feasible to model both larger-scale physics, and processes such as star formation and self-gravity. Subsequently, self-gravity is not included in our ISM simulations.

Star formation

Star formation occurs in dense molecular clouds in the ISM, which typically span a few parsecs. However, important stages of this process take place in a physical scale many orders of magnitude smaller (Gent, 2012). Crucially, these physical scales are much smaller than larger-scale processes such as galactic rotation and spiral arm structure, which renders the simultaneous modelling of these processes very computationally expensive. The problem is twofold: the evolution time of a single star requires time resolution below 1 year but the larger-scale dynamics of galaxies involve time scales of order 10^2-10^3 Myr. Time resolution below 1 year is a severe constraint on the timestep of the overall simulation, and will require at least 10^8 time steps for a single simulation; Moreover, if we assume that the spatial resolution of a typical ISM model is $\Delta x \sim 1\,\mathrm{pc}$, a modest local simulation of a $1 \times 1 \times 2\,\mathrm{kpc}^3$ region requires a $1000 \times 1000 \times 2000$ uniform grid structure. This will require continuous use of a powerful computer cluster for a long period of time, most likely months. This is before we start to consider the data storage and post-processing difficulties associated with such large datasets. Now, imagine improving the spatial resolution by two orders of magnitude; a single snapshot will be 10^6 larger than what we already consider the practical limit[2].

An additional layer of complexity is that there is not a single prescription for the process of star formation (Paron, 2018). An important trigger process is the "collect and collapse" (CC) mechanism, first proposed by Elmegreen & Lada (1977) and studied numerically by Whitworth *et al.* (1994*b*,*a*), with further treatment of the topic by Zavagno *et al.* (2010); Duronea *et al.* (2017). Walch *et al.* (2015) and Deharveng *et al.* (2015) show that this mechanism can work in conjunction with other trigger mechanisms, such as radiative implosion which was first proposed by Reipurth (1983), or cloud-cloud collisions first presented by Loren (1976).

It is possible to use AMR methods to "zoom-in" on regions which require higher spatial resolution but this method also has its limitations. It is not clear whether

[2]Most numerical simulations of this kind have at most 1000^3 grid size.

AMR can be used to improve local spatial resolution by many orders of magnitude. If we simply A more common approach is to study star formation at its own physical and time resolution scale and to incorporate sub-grid models of this physical process. The ISM simulations presented in this Thesis exclude explicit star formation. Further discussion of star formation, particularly in relation to our Model, is provided in Gent (2012).

2.2 Overview of numerical simulations

Results presented in Part II are based on analysis of numerical simulations of the interstellar medium, hereafter referred to as (the) ISM simulations. The data are taken from the simulations and PhD work of Gent (2012), with the express permission of my colleague and collaborator Dr Frederick Gent. All analysis of this data presented in this Thesis originate from my doctoral research. These results can be found in Evirgen *et al.* (2017), Shukurov *et al.* (2018) and Evirgen *et al.* (2019).

Results presented in Part III are based on numerical simulations of supernova explosions performed by the author at the *Department of Computer Science at Aalto University*, on the *taito*, *sisu* and *puhti* supercomputers hosted by the *CSC-IT Center for Science Ltd*, with financial support from the *HPC-Europa transnational access grant*[3]. The motivation for these simulations originate from a question regarding the effect of magnetic fields on hot gas in the galactic disk, which we first encountered in the larger-scale ISM simulations. I provide a description of the numerical model in Chapter 5.

2.3 ISM simulation

Gent (2012) performed a large suite of numerical simulations of the local Galaxy, which are also presented in Gent *et al.* (2013) and Gent *et al.* (2013). The data used here are from Model B2Ω, which is a non-ideal MHD shearing box simulation, featuring compressible turbulence driven by supernova explosions, on a uniform

[3]Grants HPC170UMEV and HPC17KH3CP, with additional access to Grand Challenge project GDYNS. Initial allocation was a total of 200,000 CPU hours, which has since been extended. Total usage to date is in excess of 1,000,000 CPU hours.

grid with 4 pc spatial resolution. This model features an initial, seed magnetic field of nano gauss strength. Differential rotation is included as it is an important component of dynamo action (Widrow, 2002).

In the following subsections, I provide a description of this model to ensure that the Thesis is self-contained, and that the reader can avoid the need to search external sources for the necessary basic information. However, I would like to emphasise that the following description is a truncated version of Section 3.1 in Gent (2012). I do not claim any intellectual ownership for this description.

2.3.1 Governing equations

A system of equations is solved using PENCIL[4] code. Cosmic rays are not included in these simulations. The governing equations of the simulation are the mass conservation, Navier–Stokes, heat, and induction equations. The Navier–Stokes equation is written in the rotating frame.

$$\frac{\mathrm{D}\rho}{\mathrm{D}t} = -\nabla\cdot(\rho\boldsymbol{u}) + \dot{\rho}_{\mathrm{SN}}, \tag{2.1}$$

$$\begin{aligned}\frac{\mathrm{D}\boldsymbol{u}}{\mathrm{D}t} &= -\rho^{-1}\nabla\sigma_{\mathrm{SN,kin}} - c_{\mathrm{s}}^2\nabla\left(s/c_{\mathrm{p}} + \ln\rho\right) - \nabla\Phi - Su_x\hat{\boldsymbol{y}} - 2\boldsymbol{\Omega}\times\boldsymbol{u} \\ &\quad + \rho^{-1}\boldsymbol{j}\times\boldsymbol{B} + \nu\left(\nabla^2\boldsymbol{u} + \frac{1}{3}\nabla\nabla\cdot\boldsymbol{u} + 2\boldsymbol{W}\cdot\nabla\ln\rho\right) + \zeta_\nu\left(\nabla\nabla\cdot\boldsymbol{u}\right),\end{aligned} \tag{2.2}$$

$$\begin{aligned}\rho T\frac{\mathrm{D}s}{\mathrm{D}t} &= \dot{\sigma}_{\mathrm{SN,th}} + \rho\Gamma - \rho^2\Lambda + \nabla\cdot(c_{\mathrm{p}}\rho\chi\nabla T) + \eta\mu_0\boldsymbol{j}^2 \\ &\quad + 2\rho\nu|\boldsymbol{W}|^2 + \zeta_\chi\left(\rho T\nabla^2 s + \nabla\ln\rho T\cdot\nabla s\right) + \rho T\nabla\zeta_\chi\cdot\nabla s,\end{aligned} \tag{2.3}$$

$$\begin{aligned}\frac{\partial\boldsymbol{A}}{\partial t} &= \boldsymbol{u}\times\boldsymbol{B} - SA_y\hat{\boldsymbol{x}} - Sx\frac{\partial\boldsymbol{A}}{\partial y} + \left(\eta+\zeta_\eta\right)\nabla^2\boldsymbol{A} \\ &\quad + \nabla\cdot\boldsymbol{A}\left(\nabla\eta + \nabla\zeta_\eta\right).\end{aligned} \tag{2.4}$$

Here, ρ, T and s are the gas density, temperature and specific entropy, respectively. The variable $\boldsymbol{u}$ is the deviation from the background rotation profile, referred to as a *velocity perturbation* by Gent (2012). However, this perturbation is not purely random gas motions, it includes coherently large-scale flows driven by other processes,

[4] http://pencil-code.nordita.org/

such as supernova explosions. The fields $\boldsymbol{A}$ and $\boldsymbol{B}$ are the magnetic potential and field, respectively. The equations are solved for the magnetic potential to ensure *solenoidality* throughout the simulation. The magnetic field can obtained from the magnetic potential using $\boldsymbol{B} = \nabla \times \boldsymbol{A}$. The current density is given by $\boldsymbol{j} = \nabla \times \boldsymbol{B}$. The adiabatic speed of sound is, $c_{\rm s}$, and the specific heat capacity at constant pressure is $c_{\rm p}$. S is the velocity shear rate associated with Galactic differential rotation at angular velocity $\boldsymbol{\Omega}$. Viscosity is given by ν and the rate of strain tensor, $\boldsymbol{W}$, is given by

$$2W_{ij} = \frac{\partial u_i}{\partial x_j} + \frac{\partial u_j}{\partial x_i} - \frac{2}{3}\delta_{ij}\nabla \cdot \boldsymbol{u}.$$

Shock-capturing viscosity is denoted by ζ_ν. Shock-capturing methods and their numerical implementation are discussed in Section 3.4 of Gent (2012). The variables $\dot{\sigma}_{\rm SN,th}$ and $\dot{\sigma}_{\rm SN,kin}$ refer to the SN energy injection per volume in the form of thermal and kinetic energy, respectively.

2.3.2 Initial conditions

I briefly present the initial conditions used in the ISM simulations of Gent (2012), particularly in reference to the B2Ω model used in this Thesis. The initial gas density distribution corresponds to isothermal hydrostatic equilibrium in the gravitational field (following Kuijken & Gilmore (1989))

$$g_z = -\frac{\partial \Phi}{\partial z} = -\frac{a_1 z}{\sqrt{z_1^2 + z^2}} - a_2 \frac{z}{z_2}, \tag{2.5}$$

where $a_1 = 4.4 \times 10^{-14}$ km s^{-2}, $a_2 = 1.7 \times 10^{-14}$ km s^{-2}, $z_1 = 0.2$ kpc, and $z_2 = 1$ kpc. The resullting initial gas density distribution is

$$\rho(z) = \rho_0 \exp\left[a_1 \left(z_1 - \sqrt{z_1^2 + z^2} - \frac{a_2}{2a_1}\frac{z^2}{z_1}\right)\right], \tag{2.6}$$

where $\rho_0 = 3.0 \times 10^{-24}$ g cm^{-3}.

A non-uniform initial gas temperature distribution is used to avoid long transients while keeping the imposed condition close to static equilibrium:

$$T(z) = \frac{T_0}{z_1}\left(\sqrt{z_1^2 + z^2} + \frac{a_2}{2a_1}\frac{z^2}{z_2}\right), \tag{2.7}$$

where T_0 is obtained from

$$\Gamma(0) = \rho_0 \Lambda(T_0) \approx 0.0147 \text{erg g}^{-1}\text{ s}^{-1}.$$

Here the value of T_0 depends on both the choice of ρ_0 and the choice of cooling function, Λ.

The initial magnetic field configuration is chosen such that $B_{\text{rms}} = 1\text{nG}$ and the spatial configuration is purely azimuthal (or in the y direction locally). The initial field is $\boldsymbol{B} = (0, B_I n(z), 0)$, where $B_I = 0.05\mu\text{G cm}^3$ and $n(z = 0) = 1.8\text{ cm}^{-3}$.

2.3.3 Boundary conditions

As the ISM has a statistically homogeneous structure, periodic boundary conditions are applied in the azimuthal (y) direction. This neglects the differences between arm and inter-arm regions but is a reasonable simplifying assumption since the horizontal domain is a small region ($1.024 \times 1.024\text{ kpc}^2$) compared with the horizontal extent of a galactic disc. The x direction is analogous to the cylindrical radius and sliding periodic boundary conditions are implemented in this direction to model differential rotation.

The boundary conditions at the top and bottom of the simulation domain ($z = \pm 1.088$) are more demanding, since the galactic halo extends up to 10 kpc away from the galactic midplane with gas dynamics that is not trivial to model. de Avillez & Breitschwerdt (2007) extend their vertical domain up to 10 kpc away from the midplane. Despite using a non-uniform grid (with resolution coarsening further away from the galactic midplane), their simulation domains are effectively 800^3 or 1600^3 depending on the model. This incurs a significant computational cost which is offset by using a strong initial magnetic field ($4.5\mu\text{G}$) which reduces the run-time required for the simulation. Simulations which start with a weak seed magnetic field, and allow the magnetic field to evolve via dynamo action, require in excess of 1 Gyr. The results of de Avillez & Breitschwerdt (2007) indicate that a vertical extent of at least ± 5 kpc is required for hot gas to cool and fall back towards

the midplane. Given the computational cost of attempting to use both a high spatial resolution and include the galactic halo, Gent (2012) uses a vertical extent $\pm 1\,\mathrm{kpc}$ from the midplane. Such a vertical extent allows modelling of the galactic disc and the disc-halo interaction region.

The vertical extent used by de Avillez & Breitschwerdt (2007) excludes significant mass loss from the system due to outflows, despite the computational cost incurred. However, since SNe within the galactic disc drive systematic outflows (such as galactic winds), it is important to take care with the vertical boundary conditions when using a reduced vertical extent, particularly for long run-times. For HD runs, Gent (2012) finds that the simulation reaches a statistically steady turbulent state within a few Myr. However, given the more extensive run-time required for MHD runs (with a weak seed magnetic field), and that the hot gas cools long after leaving the simulation domain, there is no physical mechanism to replace mass lost through the vertical boundaries. Subsequently, lost mass needs to be replaced numerically. The details of this are provided in Appendix C of Gent (2012).

The various vertical boundary conditions are implemented using 'ghost zones' outside the vertical boundaries, which is effectively a continuation of the numerical grid by three horizontal planes at the top and bottom of the simulation domain.

Mass

A weak negative gradient of gas density is implemented in the ghost zones to avoid artificial mass loss. Density in the ghost zones is defined as follows:

$$\rho\left(x, y, \pm Z \pm k\Delta\right) = (1 - \Delta/0.1\mathrm{kpc})\rho(x, y, \pm Z \pm (k-1)\Delta)$$

for all horizontal coordinates (x, y), $z = +Z$ and $z = -Z$ are the top and bottom boundaries of the simulation domain. The value Δ refers to the grid spatial resolution and $k = 1, 2, 3$ refers to the ghost zone layers.

Temperature

Gas temperature is kept constant in the ghost zone and set equal to the value at the boundary, such that

$$T\left(x, y, \pm Z \pm k\Delta\right) = T\left(x, y, \pm Z\right).$$

This is implemented in terms of the value of gas entropy, with reference to the gas density prescription for the ghost zones given above.

Velocity

For vertical velocity, the ghost zone values are kept equal to the boundary value if the boundary value is direct outwards from the box. Otherwise, a prescription (see Section 3.5 of Gent (2012)) is used to ensure that the inward velocity in the ghost zones is always lower than at the boundary. The horizontal components of velocity have symmetric boundary conditions to exclude horizontal stresses, such that

$$u_x\left(x, y, \pm Z \pm k\Delta\right) = u_x\left(x, y, \pm Z \mp k\Delta\right)$$

Magnetic field

The ISM simulation presented in this Thesis used a 'vertical field' vertical boundary condition for the magnetic field, which ensures zero vertical flux across the boundaries. The horizontal components of the vector potential are

$$A_x\left(x, y, \pm Z \pm k\Delta\right) = A_x\left(x, y, \pm Z \mp k\Delta\right)$$

for the x component,

$$A_y\left(x, y, \pm Z \pm k\Delta\right) = A_y\left(x, y, \pm Z \mp k\Delta\right)$$

for the y component, and

$$A_z\left(x, y, \pm Z \pm k\Delta\right) = -A_z\left(x, y, \pm Z \mp k\Delta\right)$$

for the z component. These conditions ensure that

$$\frac{\partial A_x}{\partial z} = \frac{\partial A_y}{\partial z} = 0 = B_x = B_y.$$

B_z can differ from zero. The constraint on $\partial B_z/\partial z$ is satisfied since $\nabla \cdot \boldsymbol{B} = 0$.

Other important aspects of model

- The heat equation contains terms representing photoelectric heating and optically thin radiative cooling. Photoelectric heating and radiative cooling follow the parametric prescriptions of Wolfire *et al.* (1995*a*) and Wolfire *et al.* (1995*a*); Sarazin & White (1987*a*), respectively. Gent (2012) provides a comparison of cooling and heating functions.
- An external gravitational potential is used to account for stars and dark matter following Kuijken & Gilmore (1989). Self-gravity is neglected as it is subdominant at the scales of interest for the model.

All further details of the model equations are presented in Gent (2012); Gent *et al.* (2013); Gent *et al.* (2013).

Part II

The dynamical role of large-scale magnetic fields in spiral galaxies

Chapter 3

Effects of gas flows on the large-scale magnetic field

The interstellar medium (ISM) has a complex, multi-phase structure. However very little is known about the influence that this structure has upon galactic magnetic fields. This is partly due to limitations in the observational techniques, but it should also be emphasised that galactic dynamo theory has been developed without any explicit reference to the multi-phase structure of the ISM (Beck *et al.*, 1996; Shukurov, 2007). Further theoretical progress is needed to aid the interpretation of observations.

Two types of dynamo operate in a typical spiral galaxy. The mean-field (large-scale) dynamo produces a magnetic field that is ordered on a scale larger than the turbulent scale, $l_0 \simeq 50$–$100\,\mathrm{pc}$. This process relies on the differential rotation of galactic gaseous discs as well as helical turbulence in the ISM. The e-folding time of the large-scale magnetic field, T_{MFD}, is comparable to the turbulent magnetic diffusion time across the ionised gas layer, which is of the order of $2.5 \times 10^8\,\mathrm{yr}$ near the Sun. The other key dynamo mechanism is the fluctuation (small-scale) dynamo, in which local turbulent motions (which may, or may not, be helical) produce a disordered magnetic field that is structured on the scale of the flow (e.g. Zeldovich *et al.*, 1990; Brandenburg & Subramanian, 2005). The time scale at which these small-scale magnetic fields are amplified is of the order of the eddy turnover time of the turbulent flow, $T_{\mathrm{FD}} \simeq l_0/v_0 (\simeq 10^7\,\mathrm{yr}$ in the warm phase near the Sun, assuming that the scale and speed of interstellar turbulence are $l_0 = 100\,\mathrm{pc}$ and

$v_0 = 10\,\mathrm{km\,s^{-1}}$, respectively). Both types of dynamo mechanism amplify magnetic fields up to a strength of the order of a few micro-gauss, which corresponds to energy equipartition with the turbulence, $B_0 \simeq (4\pi\rho v_0^2)^{1/2}$.

Since the fractional volume occupied by the cold and molecular gas in the ISM is negligible, it is likely that only the warm and hot phases affect significantly dynamo action at the galactic scale. The spatial scale of the mean magnetic field, of the order of 1 kpc or more, is comparable to or exceeds the typical size of the hot regions in the ISM. Furthermore, it is replenished by the dynamo at a time scale longer than the residence time of a parcel of hot gas within the gas layer, $h/V_z \simeq 5 \times 10^6\,\mathrm{yr}$, where $h \simeq 500\,\mathrm{pc}$ is the scale height of the warm, partially ionised gas layer and $V_z \simeq 100\,\mathrm{km\,s^{-1}}$ is the vertical speed of the hot gas at the base of a galactic fountain or wind. Therefore, it seems plausible that the large-scale magnetic field should be mainly produced in the warm interstellar gas that remains in an average hydrostatic equilibrium within a relatively thin layer (Shukurov, 2007). It is also important to note that, given the large volume fraction occupied by the warm phase, it is likely to form, on average, a simply connected (percolating) volume in which the mean field can reside. On the other hand, the time scale of the mean-field dynamo is so much longer than the residence time of the hot gas in the warm layer that the dynamo might be controlled by ISM parameters averaged over time scales comparable to T_{MFD}, in which case, the mean magnetic field would permeate both the warm and hot phases.

The time scale of the fluctuation dynamo T_{FD} also exceeds the residence time of the hot gas in the warm layer, but not by a wide margin. It is therefore plausible that the fluctuation dynamo is able to amplify the random magnetic field in the hot gas to the level of equipartition with the local turbulence only at a certain height above the galactic midplane, whilst the magnetic field strength in the hot gas near the midplane is significantly below equipartition.

The qualitative arguments presented above need to be tested quantitatively using numerical simulations of the multi-phase ISM. The structure of this chapter is as follows. In Section 3.1, I briefly describe the numerical simulations which are the source of the data. The method I use to define the magnetic field lines of the mean and fluctuating magnetic field components is covered in Section 3.2. In Section 3.3 I investigate how the mean and fluctuating magnetic field are connected to the different phases of the ISM. The main conclusions are summarised in Section 3.4.

3.1 Simulations of the multi-phase ISM

It is now possible to carry out magnetohydrodynamic (MHD) simulations of the ISM, including all the relevant physical processes (e.g. Korpi *et al.*, 1999*b*,*a*; de Avillez & Breitschwerdt, 2005; Mac Low *et al.*, 2005*a*; Gressel *et al.*, 2008; Piontek *et al.*, 2009; Hill *et al.*, 2012; Bendre *et al.*, 2015; Henley *et al.*, 2015). My results are based on the simulations of supernova-driven turbulence in the multiphase ISM of Gent *et al.* (2013) and Gent *et al.* (2013), subsequently referred to as Paper I and Paper II, respectively. The crucial point about these simulations is that the magnetic field has not been imposed, but evolves dynamically under realistic physical conditions (see also Gressel *et al.*, 2008; Bendre *et al.*, 2015). The numerical model is based on the non-ideal MHD equations solved in a local box of $1 \times 1\,\mathrm{kpc}^2$ horizontally and $-1 < z < 1\,\mathrm{kpc}$ vertically, with the galactic midplane located at $z = 0$. Gravity due to stellar mass and the dark halo follows Kuijken & Gilmore (1989). All models are subject to radiative cooling (Sarazin & White, 1987*b*; Wolfire *et al.*, 1995*b*), photoelectric heating (Wolfire *et al.*, 1995*b*) and other transport processes, which are necessary to support the multiphase structure. Local estimates for the differential rotation, supernova rate and distribution, and column density are used (see Ferrière, 2001). A nano-gauss seed magnetic field is amplified by dynamo action until it saturates with a typical magnetic field strength of a few micro-gauss.

I follow Gent (2012) in defining the three phases of the ISM in terms of entropy. Low entropy corresponds to cold, dense gas and high entropy corresponds to hot, diffuse gas. The cold phase is defined as $s < 4.4 \times 10^8$ erg g^{-1} K^{-1}, the warm phase as $4.4 \times 10^8 < s < 23.2 \times 10^8$ erg g^{-1} K^{-1}, and the hot phase as $s > 23.2 \times 10^8$ erg g^{-1} K^{-1}. The phases of the ISM can also be defined according to temperature and density. Specific entropy can be expressed as

$$s = c_V \left[\ln(T/T_0) - (\gamma - 1)\ln(\rho/\rho_0)\right], \tag{3.1}$$

where ρ (base unit, $\rho_0 = 1\,\mathrm{g\,cm^{-3}}$) and T (base unit, $T_0 = 1\,\mathrm{K}$) denote density and temperature, respectively, c_V is the ISM specific heat capacity at constant volume, and the adiabatic index is $\gamma = 5/3$. The phase definitions are listed in Table 3.1 together with the typical ranges in temperature and density which apply within these entropy bands. I consider volume and time averages of physical variables from 23 snapshots from a nonlinear MHD model that has twice the galactic rotation rate

Table 3.1: Definition of the ISM phases.

	Cold	Warm	Hot
s	$s < 4.4$	$4.4 < s < 23.2$	$s > 23.2$
T	$T < 500$	$500 < T < 5 \times 10^5$	$T > 5 \times 10^5$
ρ	$\rho > 10^{-24}$	$10^{-26} < \rho < 10^{-24}$	$\rho < 10^{-26}$

Entropy s in units of 10^8 erg g^{-1} K^{-1}, temperature T in units of K, and density ρ in units of g cm^{-3}.

of the solar neighbourhood. Integrating MHD models to attain dynamo saturation is computationally expensive (even the most efficient dynamo from Paper II took over 1 Gyr to reach saturation). The choice of rotation rate is a pragmatic one, designed to optimise the efficiency of the dynamo. I will consider models with lower rotation rates in future work. To illustrate the difference that a magnetic field makes to the phase-structure of the ISM, I also consider snapshots taken from the kinematic phase of the dynamo, during which the field is too weak to influence its surroundings.

3.2 The mean and fluctuating magnetic field

The decomposition of the magnetic field into mean and fluctuating (random) parts follows the method described in Paper II. Volume averaging with a Gaussian kernel, $G_l(\boldsymbol{x} - \boldsymbol{x}')$ is used to decompose the magnetic field, $\boldsymbol{B}$, into mean, $\boldsymbol{B}_l$ and random, $\boldsymbol{b}_l$, fields, following the method presented by Germano (1992). The decomposition is given by

$$\boldsymbol{B} = \boldsymbol{B}_l + \boldsymbol{b}_l, \qquad \boldsymbol{B}_l = \langle B \rangle \,, \tag{3.2}$$

where $\langle . \rangle$ represents an average on the scale l, calculated as

$$\langle B \rangle = \int_V \boldsymbol{B}(\boldsymbol{x}') G_l(\boldsymbol{x} - \boldsymbol{x}') \mathrm{d}^3 \boldsymbol{x}', \tag{3.3}$$
$$G_l(\boldsymbol{x}) = \left(\frac{1}{2\pi l^2} \right)^{3/2} \exp\left\{ -\frac{\boldsymbol{x}^2}{2l^2} \right\},$$

where $l \approx 50$pc is half the integral scale of the turbulent motions. For further details see Paper II and (Hollins *et al.*, (in prep.). A comparison of horizontal averaging and Gaussian smoothing is also provided in Appendix B. Preliminary analysis does

not show significant sensitivity of the mean or random field to variations in l within the range $30 < l < 100$pc.

Given a magnetic field, $\boldsymbol{B}(\boldsymbol{x})$, in Cartesian coordinates, its integral (field) lines are described by

$$\frac{\mathrm{d}x}{B_x} = \frac{\mathrm{d}x}{B_y} = \frac{\mathrm{d}z}{B_z} = \frac{\mathrm{d}r}{|\boldsymbol{B}|}, \tag{3.4}$$

where $\mathrm{d}r$ is a separation constant used to integrate along the field line. I obtain the integral lines for both the mean and fluctuating magnetic fields by integrating these equations using a 4^{th}-order Runge-Kutta scheme, applying linear interpolation to find the fields between grid points.

My aim is to determine the extent to which the mean and fluctuating magnetic field components prefer to reside in specific phases of the ISM. However, it is difficult to find a robust quantitative measure for this. A simple comparison of magnetic energy densities is complicated by the fact that the phases have very different physical properties, and it is not clear how to disentangle these from differences in the dynamo mechanism. I suggest a different approach, based on a comparison of entropy characteristics along field lines with the entropy distribution in the entire volume. If a magnetic field does not prefer to reside in a specific phase, the probability density function (PDF) of entropy sampled along field lines should be the same as the volume entropy PDF. Conversely, if a magnetic field is sensitive to the multi-phase structure, the difference between the field line entropy PDF and volume entropy PDF will highlight the entropy interval(s), and thus the phase, where differences arise.

3.3 Magnetic fields in the multi-phase structure

Figure 3.1(a) compares $\mathcal{P}_V(s)$, the volume-sampled entropy PDF, with $\mathcal{P}_B(s)$, the entropy PDF sampled along the mean magnetic field lines. These plots indicate that the mean magnetic field tends to favour the low entropy zone of the warm phase; the peak of $\mathcal{P}_B(s)$ is located at $s = 12$, whereas the corresponding peak of $\mathcal{P}_V(s)$ is located at $s = 15$, and for $18 \lesssim s < 23$, $\mathcal{P}_B(s)$ is systematically lower than $\mathcal{P}_V(s)$. Furthermore, for entropy values in the range $s > 23$, $\mathcal{P}_B(s)$ is significantly lower than $\mathcal{P}_V(s)$, which suggests that the mean field is generally absent from the

hot gas. Figure 3.1(b) shows a comparison between $\mathcal{P}_V(s)$ and $\mathcal{P}_b(s)$, which is the PDF following the fluctuating (random) component of the magnetic field. The differences between these curves are less dramatic than those shown in Figure 3.1(a). Whilst $\mathcal{P}_b(s)$ systematically has a higher probability density than $\mathcal{P}_V(s)$ for $s < 15$, the difference is clearly smaller than for $\mathcal{P}_B(s)$. The random field component is suppressed to some extent in the hot phase, but this effect is less pronounced than it was for the mean field.

Figure 3.2 uses a single snapshot in the nonlinear regime to give an alternative view of these results. In panel (a), there is a large column (chimney) of hot, high entropy gas spanning the domain horizontally and vertically, from which mean magnetic field lines appear to be absent. This is consistent with the PDFs shown in Fig. 3.1, further reinforcing the idea that the mean magnetic field is sensitive to the multi-phase structure. Panel (b) shows that the mean magnetic field tends to be aligned with the y-direction. This is unsurprising as it coincides with the direction of the velocity shear. Panels (c) and (d) show the random (fluctuating) magnetic field in the same snapshot. As expected, the field lines do not appear to have a preferred direction. In addition, the random magnetic field lines do not appear to avoid the column of hot gas in the same way as the mean field. Thus, the random magnetic field appears to be less sensitive to the multi-phase structure. It is worth noting here that the velocity field is in a statistically steady state in the kinematic phase. This has been investigated by Gent (2012); Gent *et al.* (2013) and also in adhoc analysis performed by the author to verify results, which also compare velocity fields with those found in hydrodynamic simulations. Thus, the changes to velocity field can be attributed to the magnetisation of the simulated ISM.

It remains to be understood whether the absence of the mean fields from the hot gas is caused by the mean field being expelled by blast waves from the SN remnants. Figure 3.3 shows that the mean and random magnetic fields reach their maximum amplitude away from the midplane. This may indeed be due to the disruptive effect of supernova shocks on the magnetic structure and formation, as SN explosions are primarily confined within 200 pc of the midplane. I note that the random magnetic field strength remains of order 1μG for $|z| < 0.2$ kpc, whilst the mean magnetic field increases from 1.6μG at the midplane to 2.6μG at $z = 300$ pc. The mean field strength at the midplane is remarkably consistent with the observed estimate of Rand & Kulkarni (1989), while by comparison the random field is only 20–25%

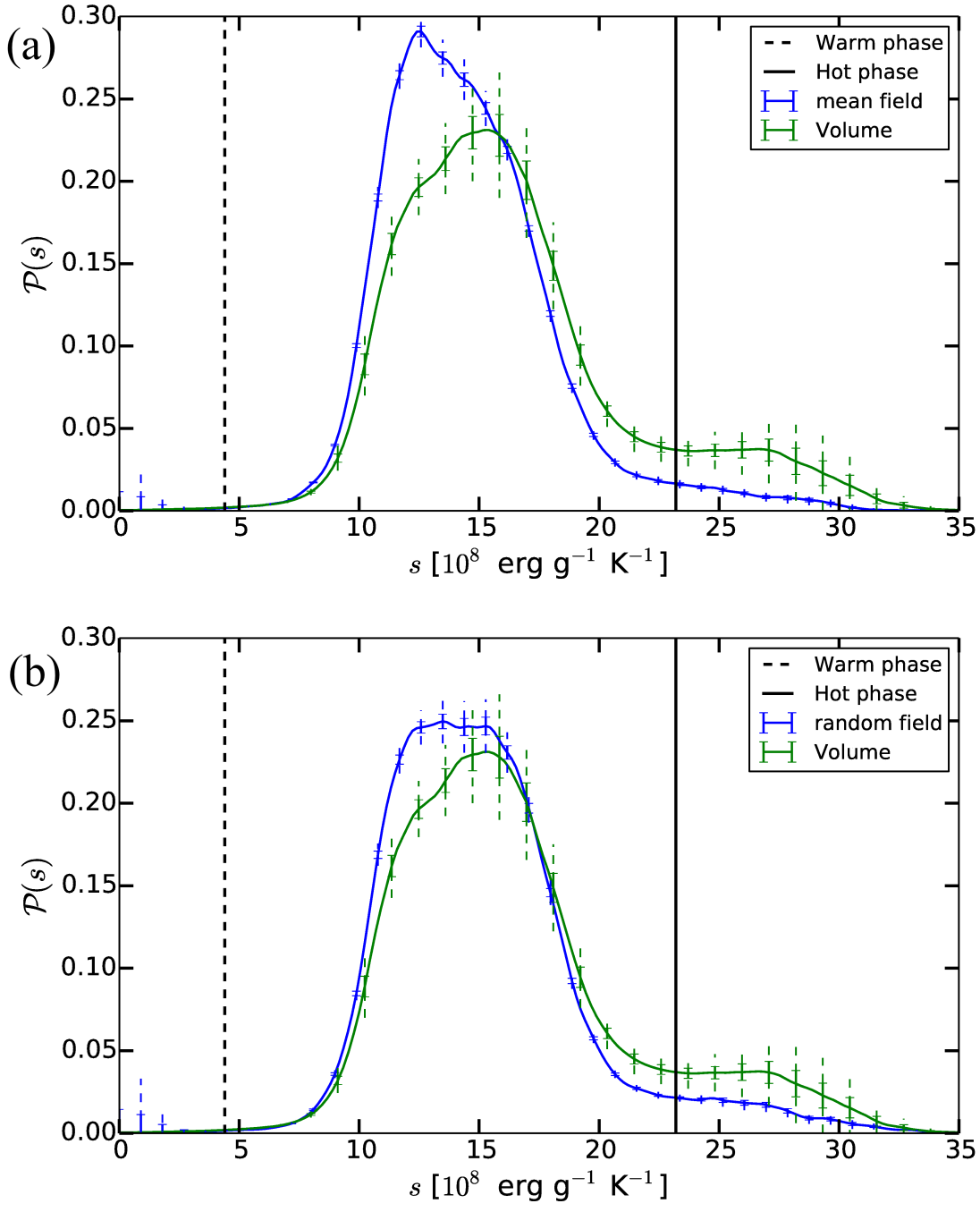

Figure 3.1: PDFs of entropy, $\mathcal{P}_V(s)$, calculated from volume samples together with **(a)** samples along integral lines of the mean magnetic field $\mathcal{P}_B(s)$, and **(b)** samples along integral lines of the random magnetic field $\mathcal{P}_b(s)$. Vertical lines show the boundaries between the cold and warm ISM phases and the warm and hot phases.

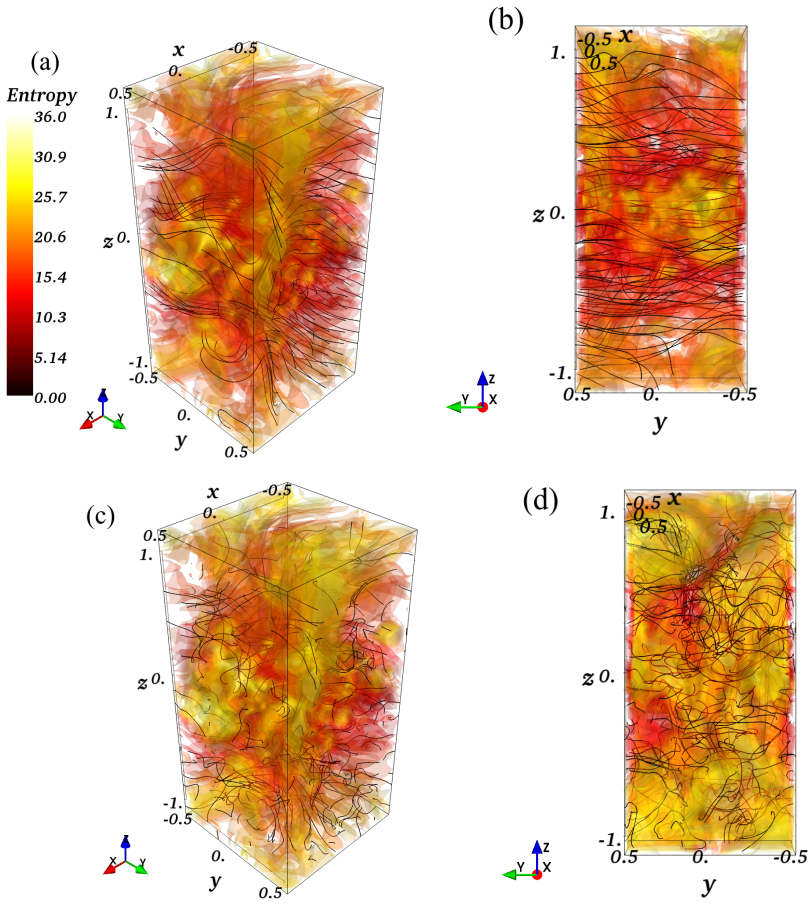

Figure 3.2: 3D rendering of magnetic field lines (black lines) in the simulated ISM gas, with gas entropy in the background. Panels **(a)** and **(b)** show the mean-field lines and panels **(c)** and **(d)** the random field lines. Panels **(a)** and **(c)** give an isometric view, whilst panels **(b)** and **(d)** show a view through the (y, z) plane.

of their estimate or that of Haverkorn (2015). The reason for this difference is not obvious. It may indicate that the fluctuation dynamo (which directly generates small scale field) is less efficient than it should be, so that the observed random field is due primarily to the tangling of mean-field lines by the turbulent velocity field. Another possibility is the (implicit) use of longer averaging scales in the interpretation of the observations. The domain size of 1 kpc limits the smoothing scale which can be applied. However, these possibilities are speculative and more work is required to understand properly the relatively weak random field in the simulations.

Looking again at Figure 3.3, there is a local maximum in the random velocity $|\boldsymbol{u}|$ at the midplane, where the supernovae dominate the dynamics. Away from the

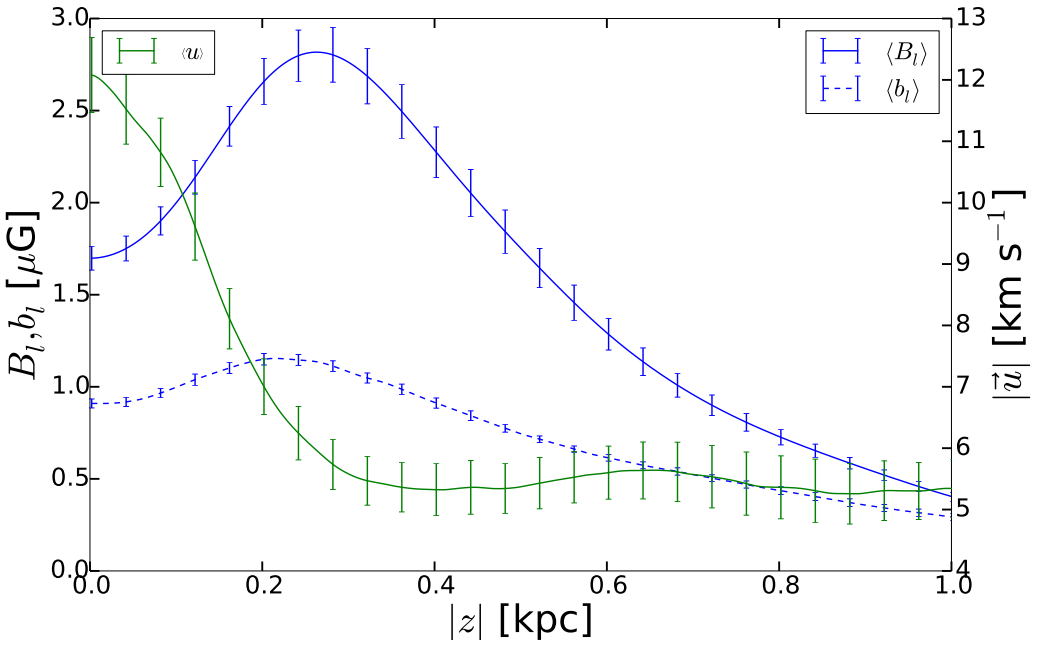

Figure 3.3: Horizontal averages of mean magnetic field strength $|\boldsymbol{B}_l|$, random magnetic field strength $|\boldsymbol{b}_l|$ and random velocity $|\boldsymbol{u}|$, shown as functions of distance from the midplane.

midplane, the random velocity decreases rapidly reaching a minimum value at approximately $|z| \sim 0.4$ kpc, where the mean magnetic field is strong. At larger values of $|z|$, the amplitudes of the mean and fluctuating components of the magnetic field both decrease with increasing distance away from the midplane. In this region, the mean magnetic field strength decreases from its maximum, 2.6μG, to 0.4μG. The decrease in random magnetic field strength is more modest (1 to 0.3μG). The variation of the magnetic field with $|z|$ suggests that the most efficient dynamo action is confined primarily to regions within a few hundred parsecs of the midplane.

Figure 3.4 displays the volume weighted PDFs of entropy during both the early kinematic and non-linear (saturated) dynamo stages. There is a difference in the distribution of entropy between the ISM with a dynamically-insignificant (i.e. kinematic) magnetic field and the ISM with a dynamo-generated magnetic field, when the dynamo has reached saturation. Whilst the modal probabilities of the warm and hot phase are similar, the shape of the distribution is different. In the case of a saturated dynamo, the PDF is wider in the warm phase, and has a region of higher probability density in $10 < s < 12$. In addition, saturation of the dynamo leads to

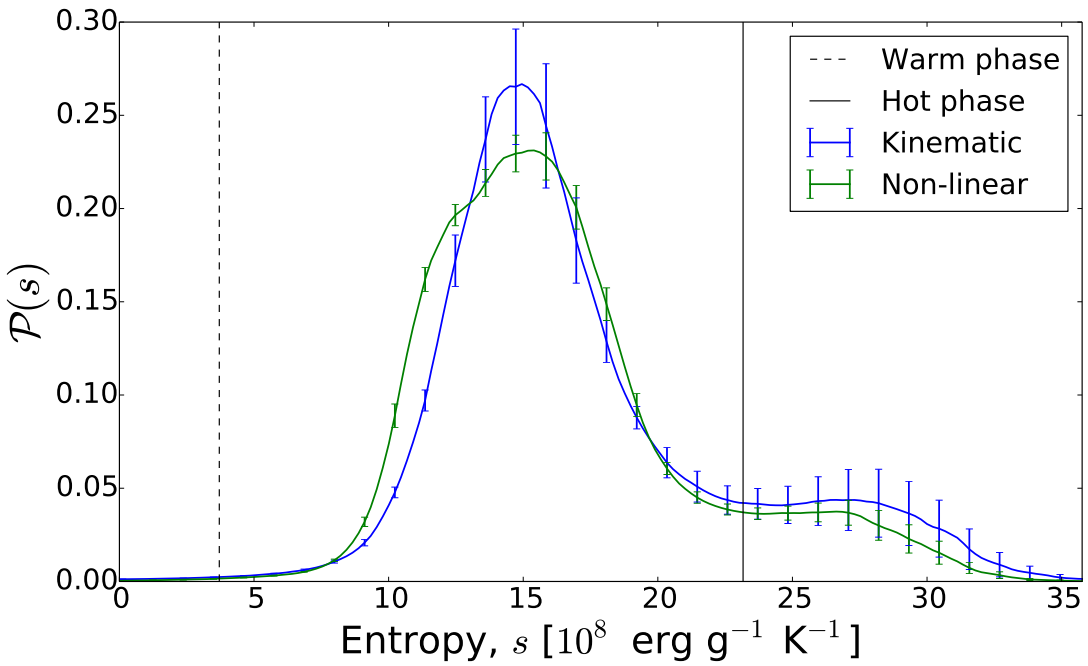

Figure 3.4: Volume entropy PDFs for the kinematic (growing) and non-linear (saturated) state of the dynamo. Vertical lines show the boundaries between the cold and warm ISM phases and the warm and hot phases.

a consistent reduction of probability density for the higher entropy gas with $s > 20$. Even though there is clear evidence for the existence of a warm and hot phase the entropy distributions within the phases change as the magnetic field grows.

3.4 Summary

I have shown that the mean magnetic field is sensitive to the multiphase structure of the ISM. The PDF analysis indicates that it resides preferentially in the lower entropy region of the warm phase, particularly in the layer $0.2 < |z| < 0.4$ kpc, avoiding regions of hotter gas. Given the presence of the velocity shear, it is unsurprising that this mean field tends to be aligned with the y-coordinate (i.e. the azimuthal direction) in the model. The random magnetic field appears to be less strongly influenced by the multiphase structure. As functions of distance from the midplane ($z = 0$), the mean and random magnetic field strengths peak at $|z| = 300$pc and $|z| = 200$pc, respectively.

The marginal preference of the fluctuating field for low entropy regions of the warm phase is likely to be caused by generation of the random field by tangling of the mean field produced by the large-scale dynamo. Small-scale dynamo action may not be fully resolved with a minimum resolution of 0.004 kpc, and so may be less efficient than it should be, but this interpretation is speculative. Separating the two different mechanisms, by which the random field can be produced is subtle and difficult; I shall return to this problem in subsequent work that examines how galactic dynamos saturate in the multi-phase ISM.

There is an increasing fractional volume of gas within the warm phase, as the mean magnetic field grows and saturates. Whilst it was expected that the magnetic field preferentially resides in the warm phase, this result suggests that dynamo action actively changes the volume entropy distribution, and thus the multi-phase structure of the ISM. This raises a significant question: does the magnetic field preferentially reside in the warm phase, or does it adapt the multi-phase structure, in order to create a hospitable environment for dynamo action? In other words, how does the multi-phase structure change as the ISM becomes magnetised? I will discuss these questions, which can have important consequences for galactic evolution, in future work.

Chapter 4

Effects of the large-scale magnetic field on the ISM

4.1 Introduction

In the dynamics of the interstellar medium (ISM), the role of magnetic fields is most often discussed in the contexts of the pressure support of the galactic gas layer (Bloemen, 1987; Boulares & Cox, 1990; Fletcher & Shukurov, 2001, and references therein), galactic winds, especially with cosmic rays (Breitschwerdt *et al.*, 1991, 1993; Everett *et al.*, 2008), and star formation (Peters *et al.*, 2011; Crutcher, 2012). There is no clear consensus about the dynamical significance of magnetic fields in the ISM as a whole. For example, de Avillez & Breitschwerdt (2005); Hill *et al.* (2012); Walch *et al.* (2015) suggest a modest or negligible magnetic field contribution, while Ferrière (2001); Cox (2005, and references therein) argue for a significant dynamical role. The exploration of interstellar magnetic fields and their effects upon the structure and dynamics of the multi-phase ISM is complicated by difficulties in observing them, for example, by the absence of observational estimates for magnetic field strength in the hot gas.

One way to clarify the picture is to employ increasingly powerful and realistic numerical simulations. Numerical simulations have explored many aspects of the ISM,

covering a variety of physical effects on a broad range of scales from sub-parsec to kiloparsec. Each numerical model must exclude some physical processes at relevant length and time scales, but each helps to clarify the significance of particular physical effects. The first numerical models of the SN-driven, multi-phase ISM of Rosen & Bregman (1995), Rosen *et al.* (1996), Vazquez-Semadeni *et al.* (1995), Passot *et al.* (1995) and Gazol-Patiño & Passot (1999) were two-dimensional but the significance of magnetic fields was evident even then. The first three-dimensional simulations that included all ingredients required for realistic modelling of magnetic fields at both large and small scales (differential rotation, stratification, random nature of the gas flow and sufficiently high kinematic and magnetic Reynolds numbers) were presented by Korpi *et al.* (1999*b*,*a*) while the simulations of de Avillez (2000) and de Avillez & Berry (2001) focussed on non-magnetic effects. These are local models with the computational domain of a kiloparsec size and numerical resolution of a few parsecs. With the computational facilities available, global models where numerical resolution is sufficient to capture reliably the random nature of interstellar gas flows neglect magnetic fields and are restricted to a relatively small central region of galactic discs (within about 2.6 kpc of the centre and 0.15 kpc of the midplane) in two (Wada & Norman, 2001; Wada *et al.*, 2002) and three (Wada & Norman, 2007) dimensions. Extension to a larger region is only possible at the expense of reduced spatial resolution (Hanasz *et al.*, 2009; Siejkowski *et al.*, 2014).

Apart form the models of Korpi *et al.* (1999*b*), Gressel *et al.* (2008), Gent *et al.* (2013); Gent *et al.* (2013) and Bendre *et al.* (2015), magnetic fields in these simulations are imposed (i.e. supported by initial and/or boundary conditions, even if modified by the gas flows) rather than produced self-consistently by large- and small-scale dynamos. I find evidence, discussed in Section 4.3.1, that the multi-phase gas structure and galactic outflows are sensitive to the nature of the magnetic field support, and dynamo-generated magnetic fields affect the ISM in a more profound manner. Evirgen *et al.* (2017) discussed the effects of the multi-phase ISM structure on the mean and random galactic magnetic fields in a numerical simulation of the supernova-driven multi-phase ISM. Here, I explore the effects of the magnetic field on the ISM including its multi-phase structure, gas outflow and the force balance. I identify several effects which are rather unexpected and yet, with hindsight, physically compelling.

The focus of this Chapter is on the dynamical role and significance of dynamo-

generated large-scale magnetic fields. Discussion of this topic is based on changes to the vertical and multiphase structure near the galactic disk, due to magnetisation of the simulated ISM. Results are presented following a brief overview of the numerical model used for the analysis.

4.2 Simulations of the SN-driven ISM

A local Cartesian box, $1 \times 1\,\mathrm{kpc}^2$ in size horizontally and extending to 1 kpc on each side of the galactic midplane, is placed at a galactocentric radius of 8 kpc (Gent *et al.*, 2013, hereafter, ISM I). The local Cartesian coordinates (x, y, z) correspond, respectively, to the cylindrical polar coordinates $(r, \phi\, z)$ with the z-axis aligned with the galactic angular velocity. Parameters are representative of the Solar neighbourhood, but with rotation double the rate in the Milky Way to accelerate magnetic field amplification by the dynamo, as discussed in Gent *et al.* (2013, hereafter, ISM II) and Evirgen *et al.* (2017); the numerical model used here is denoted B2Ω in Gent (2012). Supernova sites, where thermal and kinetic energies are injected into the gas, are distributed randomly in time and space at the occurrence frequency of the Solar neighbourhood. The numerical resolution is 4 pc in each direction; with such a grid spacing, it is possible to reproduce the known expansion laws of supernova (SN) remnants from the Sedov–Taylor to the late snowplough phases (ISM I);(Hollins *et al.*, 2017*b*). Differential rotation is implemented using the shearing periodic boundary conditions in the radial (x) direction. The system of non-ideal, fully compressible and nonlinear magnetohydrodynamic (MHD) equations is solved assuming the equation of state of an ideal monatomic gas. The simulations use the ISM module of the Pencil Code[1]. The momentum equation includes velocity shear due to galactic differential rotation, the Coriolis force, viscous stress, kinetic energy injection by SNe, and the Lorentz force. A fixed gravity field is due to the stellar mass and the dark matter following Kuijken & Gilmore (1989). The energy equation includes viscous and Ohmic heating and thermal energy injected by the SNe. Radiative cooling is parametrised using the cooling functions of Sarazin & White (1987*b*) and Wolfire *et al.* (1995*b*), and photoelectric heating follows Wolfire *et al.* (1995*b*). The cooling rate is truncated at $T = 100\,\mathrm{K}$ to avoid numerically intractable gas densities; the heat diffusion is enhanced to ensure that gas clouds produced by thermal instability

[1]https://github.com/pencil-code

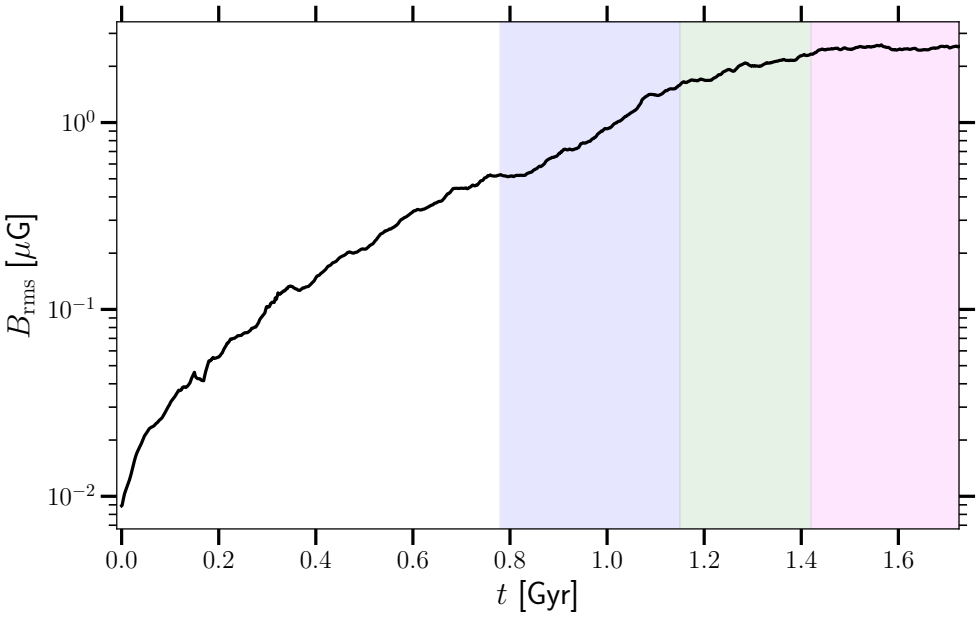

Figure 4.1: Evolution of the rms magnetic field strength. During the Early (kinematic) stage of the dynamo, the field grows exponentially. The dynamo is in a statistically steady state during the Late stage. The blue, green and magenta shaded regions refer to the Early, Transitional, and Late stages, respectively.

are fully resolved at the working numerical resolution (further details can be found in Appendix B of ISM I). Self-gravity is neglected given the relatively low gas densities in the simulated ISM, $n \lesssim 10^2\,\mathrm{cm}^{-3}$ in terms of the number density. The induction equation is solved in terms of the vector potential to ensure the solenoidality of the simulated magnetic field. The detailed form of the equations can be found in ISM I.

Figure 4.1 shows the time evolution of the volume–averaged root-mean-square (rms) magnetic field strength and introduces the Early and Late stages of the model evolution. During the Early stage, $0.78 \lesssim t \lesssim 1.15\,\mathrm{Gyr}$, the magnetic field is too weak to influence the flow or perturb the thermodynamic structure of the ISM; the dynamo is therefore kinematic, which explains the exponential growth in the magnetic field strength. Next follows a transitional stage ($1.15 \lesssim t \lesssim 1.42\,\mathrm{Gyr}$) when the growth of the field slows down as the Lorentz force gradually becomes strong enough to exert a dynamical influence upon the flow. The system settles to a statistically steady state in the Late stage, $t \gtrsim 1.42\,\mathrm{Gyr}$, where the energy density of the magnetic field

is comparable to that of the random motions and thermal energy. By comparing the system during the Early and Late stages (the former with a negligible magnetic field, the latter with a dynamically significant field) it is therefore possible to identify the effects of magnetic fields on the ISM. I stress that the Early stage represents a hydrodynamical statistically steady state of the system, whereas the Late stage is an MHD steady state. Wherever appropriate, I present results for the transitional stage despite its transient nature, since it may be observable in high-redshift galaxies and to illustrate the continuity of the adjustments between the Early and Late stages.

4.3 Vertical structure of the ISM

It is generally accepted that magnetic fields can affect the structure and dynamics of the interstellar medium. However, the magnetic effects are still not fully understood, with a number of important questions still unresolved. In this section, I present detailed comparison of the simulated ISM in its Early and Late stages to identify the ways in which magnetic fields affect this system.

4.3.1 Changes to the vertical distribution of specific entropy and gas density

Figure 4.2 shows the specific entropy distribution for a few representative snapshots, at various stages of evolution of the simulated ISM. The specific entropy of the interstellar gas is defined by

$$s = c_V \left[\ln \frac{T}{T_0} - (\gamma - 1) \ln \frac{\rho}{\rho_0} \right], \tag{4.1}$$

where c_V is the specific heat capacity at constant volume, T and ρ are the gas temperature and density, with the reference values $T_0 = 1\,\mathrm{K}$ and $\rho_0 = 1\,\mathrm{g\,cm^{-3}}$, and $\gamma = 5/3$ is the adiabatic index. Specific entropy is quoted in the text in units of $10^8\,\mathrm{erg\,g^{-1}\,K^{-1}}$.

The top panels of Fig. 4.2 are taken from the Early stage (in which the magnetic field is dynamically negligible); the bottom panels represent the Late stage (when

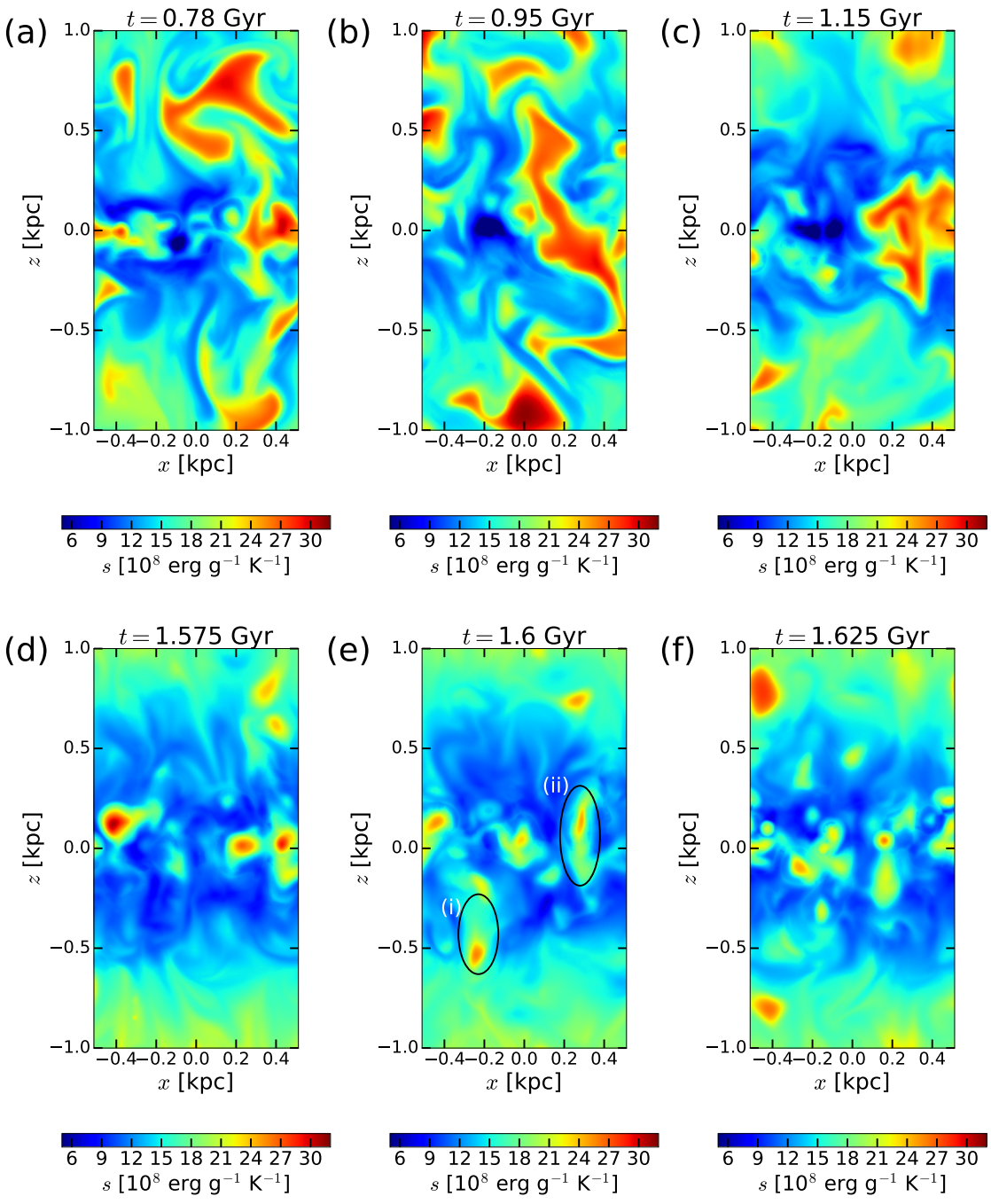

Figure 4.2: Specific entropy in the (xz)-plane, corresponding to (r, z) of the cylindrical frame, with the large-scale velocity shear in the y-direction: **(a)**, **(b)** and **(c)** are from the Early stage whereas panels **(d)**, **(e)** and **(f)** represent the Late stage. The time after the start of the simulation is given at the top of each panel and entropy colour bars are provided at the bottom. It is evident that the system is more homogeneous in the Late stage, with a lower abundance of the hot gas. The structures labelled (i) and (ii) in panel (e) are discussed in the text.

the magnetic field becomes dynamically important). Specific gas entropy s is colour coded, with red corresponding to hot and dilute gas, and blue to cooler and denser gas. Blue colours represent the warm phase of the simulated ISM ($4.4 < s < 23.2$, $500 < T < 5 \times 10^5\,\mathrm{K}$, $10^{-26} < \rho < 10^{-24}\,\mathrm{g\,cm^{-3}}$ for the specific entropy, temperature and density, respectively); the cold gas occupies a small fraction of the volume and is hardly visible in this representation.

In the Early stage, large hot gas structures are widespread and many of them span a large part of the domain. In the Late stage, the hot structures are typically smaller and rounder. This suggests that the magnetic field tends to drive the system towards a more homogeneous gas distribution, given that any qualitative changes arise from the evolution from a hydrodynamically steady state to a magnetohydrodynamically steady state. Some indications of this behaviour can already be seen in panel **(c)** of Fig. 4.2, which corresponds to the end of Early stage (when local magnetic fields can already be dynamically important); the regions of hot gas already seem to be less extensive than those at earlier times.

Panel **(e)** of Fig. 4.2 contains two features, labelled (i) and (ii), that demonstrate the reduced ability of hot gas to expand in the Late stage. They show hot structures formed close to the midplane and rising to larger $|z|$ producing little disturbance in the surrounding gas.

Figure 4.3 provides an alternative view of the gas structure showing the horizontally averaged gas density and specific entropy, as functions of distance z to the midplane, averaged over time for the Early (17 snapshots) and Late (13 snapshots) stages separately. During the Early stage, the mean gas density is maximum at the midplane, decreasing rapidly with height within 100 pc of the midplane and then more gradually. In the Late stage, there is a clear flattening of the density profile for $|z| \lesssim 0.3\,\mathrm{kpc}$, but a steeper density gradient for $|z| \gtrsim 0.3\,\mathrm{kpc}$. The specific entropy is everywhere lower in the Late stage than it is in the Early stage, which is consistent with the apparent reduction in the abundance of hot gas. A pronounced minimum in the specific entropy at around $|z| \simeq 0.3\,\mathrm{kpc}$ is notable – this is the same height at which the mean density gradient changes.

Hill *et al.* (2012, their Figure 9**a** and Table 4) present vertical profiles of gas density in MHD simulations of the SN-driven ISM where the magnetic field is not generated self-consistently by the dynamo action, as in our model, but imposed to be initially

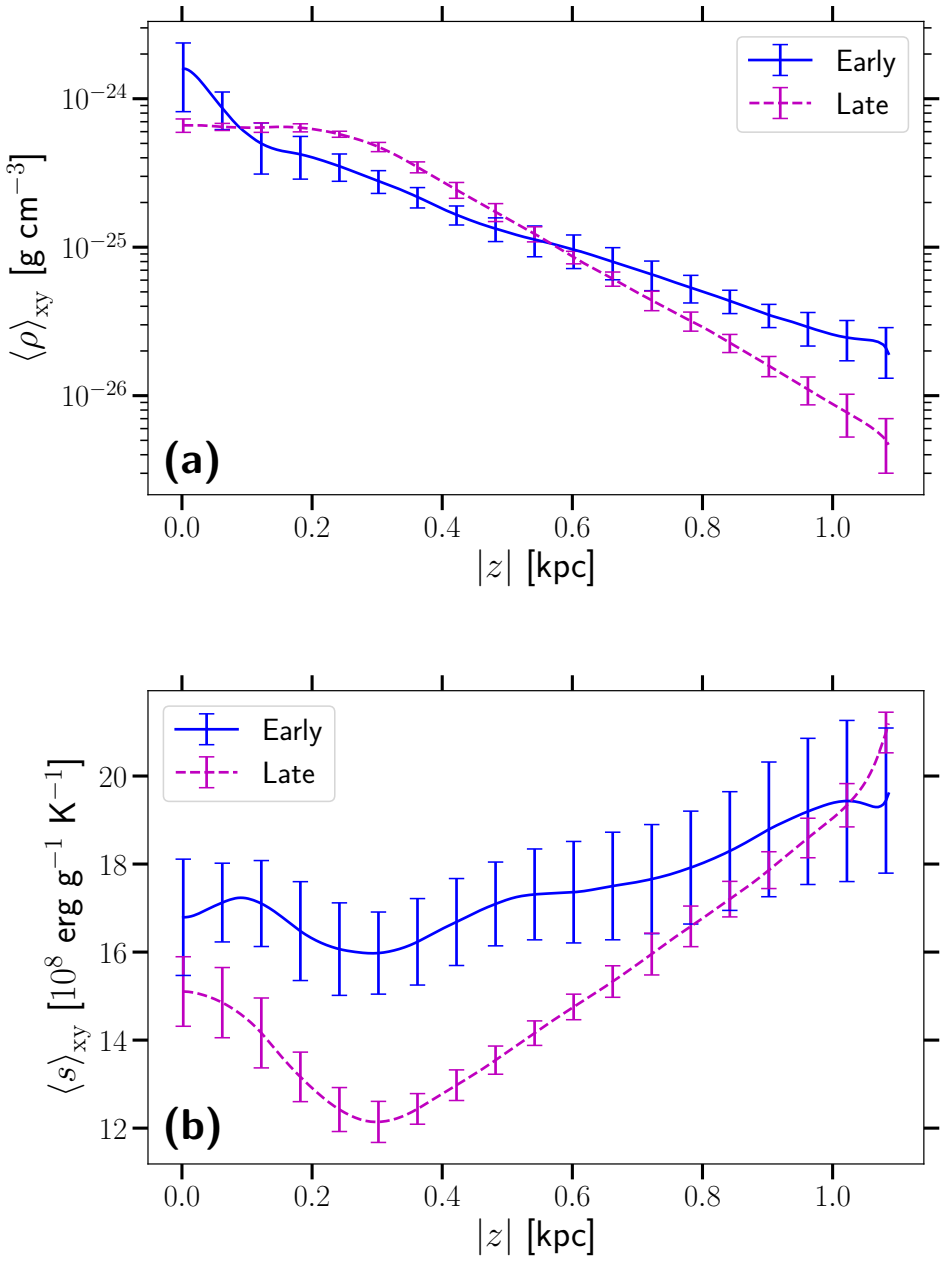

Figure 4.3: The horizontally averaged **(a)** gas density and **(b)** specific entropy versus distance to the midplane, $|z|$, further averaged over time for the Early (solid, blue) and Late (dashed, magenta) stages of the evolution.

independent of x and y and scale with the initial gas density as $n^{1/2}(z)$. This model shows that the gas distribution is rather insensitive to the strength of the magnetic field, when it varies between 0 and 10 μG at the midplane. The vertical gas density profile in the Early stage of our Model is similar to the density profiles of Hill *et al.* (2012). Thus, the ISM containing magnetic field produced by the system itself in a self-consistent manner via dynamo action is very different. Numerical models which do not allow for dynamo action commonly use *a priori* assumptions regarding magnetic field strength and spatial form. For example, de Avillez & Breitschwerdt (2005), Hill *et al.* (2012) and Girichidis *et al.* (2016) use an initial field of micro-gauss strength, where the strength of the uniform component scales with the gas density as $n(z)^{1/2}$, decreasing monotonically with distance from the midplane. These authors find that the magnetic field does not contribute to vertical force balance as magnetic pressure gradient and magnetic tension compensate each other. In our simulations, and those of Gressel *et al.* (2008) and Bendre *et al.* (2015), dynamo action changes the vertical distributions of the magnetic field strength and gas density, leading to a different dynamical role to that seen in models with a strong initial magnetic field.

4.3.2 Enhanced cooling of hot gas in a magnetised ISM

The effects described above are noticeable over a scale of hundreds of parsecs. However, both the smaller size of hot gas structures, seen in Fig. 4.2, and the decrease in entropy – particularly close to $|z| = 300$ pc, seen in Fig. 4.3 **b**, suggest that hot gas is affected by the magnetic field at smaller scales as well. I find that the fractional volume of the hot gas decreases from 20–25% in the Early stage to 1–5% in the Late stage. Makarenko *et al.* (2018) also find differences in the topology of gas density fluctuations, between the Early and Late stages, which suggest that the ISM becomes more homogeneous as the magnetic field grows. As shown in Fig. 4.4, the average number density of the hot gas increases by a factor of two from the Early to the Late stage. This enhances the cooling rate but cannot account fully for the reduction in the fractional volume of the hot gas by a factor of more than five.

The cooling of the hot gas is further enhanced by its longer residence time near the midplane, as its outflow is quenched by the magnetic field. This is reflected in the decrease of cooling length of hot gas, which is defined as $L_{\rm c} = \tau_{\rm c} U_{\rm hot}$, where $U_{\rm hot}$ is the mean vertical velocity of the hot gas shown in Figure 4.5 **(b)** and $\tau_{\rm c} = c_V T/(\rho \Lambda)$

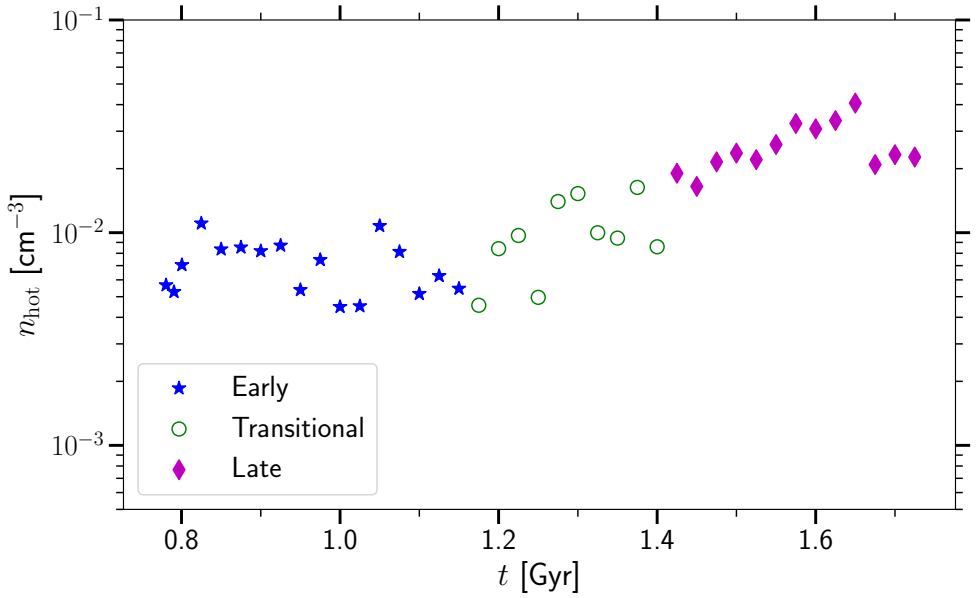

Figure 4.4: The average number density of the hot gas at various stages of magnetic field growth. The Early, Transitional and Late stages are represented by blue stars, green circles, and magenta diamonds, respectively.

is the radiative cooling time, with Λ the cooling function (described in detail in Gent *et al.*, 2013), c_V is the specific heat and T and ρ are the gas temperature and density. The cooling length represents the distance over which the hot gas loses a significant part of its thermal energy as it flows away from the midplane. Figure 4.6 shows that the cooling length decreases from 50–100 kpc in the Early stage, to about 1 kpc in the Late stage. The former value is significantly larger than the vertical extent of the simulation domain (and the galactic disc), which suggests that hot gas leaves the disc with only a modest radiative cooling. Conversely, in the Late stage, the cooling length becomes comparable to the vertical extent of the simulation domain, indicating that hot gas cools down significantly even within the disc. The magnetic fields affect the abundance of hot gas in two indirect ways: firstly, it enhances the cooling rate of the hotter gas by increasing its density; secondly, it opposes the outflow of the hot gas from the midplane, allowing it to cool for a longer time.

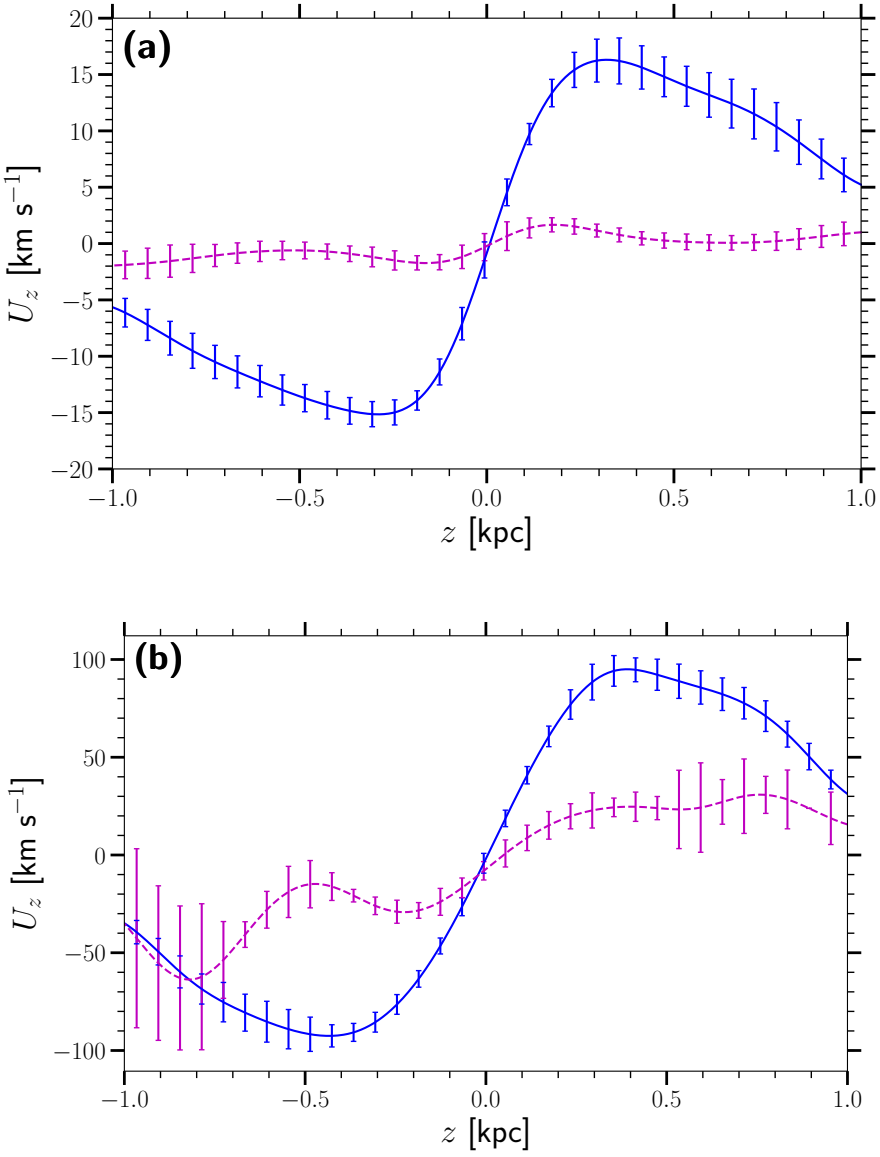

Figure 4.5: **(a)** The horizontally averaged vertical velocity versus $|z|$ in the Early (solid, blue) and Late (dashed, magenta) stages of magnetic field evolution **(b)** as in panel (a) but for the hot gas alone.

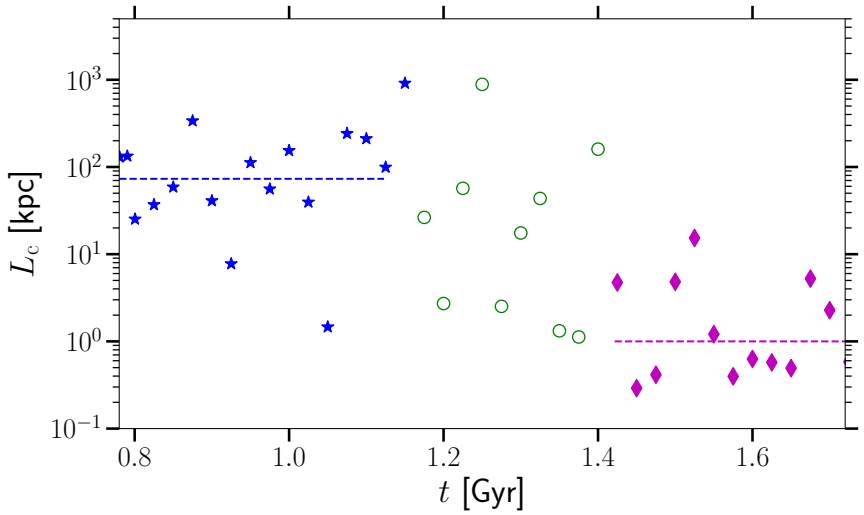

Figure 4.6: The evolution of the cooling length of the hot gas. The Early, Transitional and Late stages are represented by blue stars, green circles, and magenta diamonds, respectively. The typical cooling length is 70 kpc in the Early stage and 1 kpc in the Late stage.

4.3.3 Magnetic quenching of vertical velocity

There are contradictory opinions about the effects of magnetic fields in galactic outflows. Boulares (1988), Boulares & Cox (1990), Passot *et al.* (1995), and Bendre *et al.* (2015) suggest that a large-scale magnetic field does affect vertical gas motions. However, the numerical simulations of de Avillez & Breitschwerdt (2005), Hill *et al.* (2012) and Girichidis *et al.* (2016) find no evidence for such an effect with an imposed plane-parallel magnetic field. To determine whether the decrease in vertical velocity is connected to the magnetic field, I examine the relationship between the dependence of the mean vertical velocity $|\langle U_z \rangle_{xy}|$ on mean magnetic field strength[2] It is useful to compare with Figure 6 of Bendre *et al.* (2015). Our results can be approximated by

$$|U_z| \approx \frac{U_0}{1 + |\xi \langle B \rangle_{xy} / \langle B_{eq} \rangle_{xy}|^n}, \tag{4.2}$$

where B_{eq}, a function of z, is the local equipartition magnetic field strength, $B_{eq}^2 = 4\pi\rho u^2$, where u is the turbulent gas velocity. The fitted values for U_0, ξ, and n are

[2]The total magnetic field is decomposed into mean and random components using horizontal averaging. I also use horizontal averaging to calculate vertical profiles of quantities presented in this Chapter, which is shown in Figure 4.7.

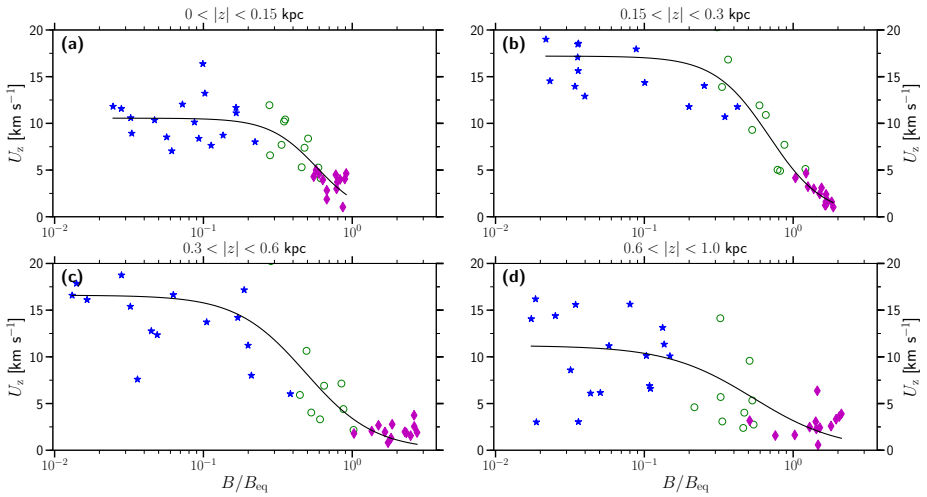

Figure 4.7: The dependence of the mean vertical speed on the strength of the mean magnetic field at various distances from the midplane: **(a)** $0 \leq |z| \leq 0.15\,\mathrm{kpc}$, **(b)** $0.15 \leq |z| \leq 0.30\,\mathrm{kpc}$, **(c)** $0.3 \leq |z| \leq 0.6\,\mathrm{kpc}$ and **(d)** $0.6 \leq |z| \leq 1.0\,\mathrm{kpc}$. The data points represent horizontally averaged values of the mean vertical speed in individual snapshots in the Early (blue star), Transitional (green circle) and Late (magenta diamond) stages of magnetic field evolution. Parameters of the fits (4.2), shown in black solid lines, are given in Table 4.1.

Table 4.1: Fits to the outflow speed, of the form (4.2), at various distances $|z|$ from the midplane.

Distance to the midplane [kpc]	U_0 [$\mathrm{km\,s^{-1}}$]	ξ	n
$\lvert z\rvert < 0.15$	11	1.7	2.7
$0.15 < \lvert z\rvert < 0.3$	17	1.4	2.4
$0.3 < \lvert z\rvert < 0.6$	17	2.1	1.9
$0.6 < \lvert z\rvert < 1.0$	11	1.9	1.5
$\lvert z\rvert = 0.8$ (Bendre *et al.*, 2015)	12	1.2	2

given in Table 4.1. Bendre *et al.* (2015) show a similar relation between $|\langle U_z \rangle|$ and $\langle B \rangle_{xy} / \langle B_{\mathrm{eq}} \rangle_{xy}$ (Figure 6). While fitted parameters differ, both fits feature a steep decrease in vertical velocity for values of this ratio above a threshold value. I find that this threshold value is $0.1 - 0.2$, in agreement with Bendre *et al.* (2015).

4.4 Gas pressure

Figure 4.8 shows vertical profiles of various pressure components for the Early and Late stages. In the Early stage, thermal and kinetic pressure are dominant; while magnetic pressure is approximately an order of magnitude smaller. The total pres-

sure gradient is constrained by the weight of the gas and the strength of the gravity field. The latter does not change during the simulation, so the increase over time in the vertical gradient of the total pressure is due to the ejection of gas to larger altitudes. The contributions of the thermal and turbulent pressures decrease together with the total pressure as the magnetic field grows (the relative contribution of the turbulent pressure decreases especially strongly in the Late stage) as they are replaced by the magnetic pressure. The contributions of the gradients of the various pressure components to the force balance are discussed in Section 4.5.

Remarkably, magnetic pressure is the only part of the total pressure that varies with $|z|$ non-monotonically, confining the gas at $|z| \lesssim 0.3\,\mathrm{kpc}$ and producing an outwardly directed force above that level. In the Late stage, magnetic pressure is within an order of magnitude of thermal and kinetic pressure within 200 pc of the midplane. It is in equipartition with thermal pressure, and in supra-equipartition with kinetic pressure further away from the midplane. A stronger magnetic field may be produced near the midplane and advected to larger altitudes to dominate over the random flows there, as I discuss in Section 4.6.

4.5 Vertical force balance

To understand the dynamics of the ISM, in particular the effects of magnetic tension and pressure gradient on the vertical flow, I consider the averaged vertical momentum equation

$$\frac{\partial}{\partial t}\left\langle \rho U_z \right\rangle_{xy} = \left\langle \rho g_z \right\rangle_{xy} - \frac{\partial P}{\partial z} + \frac{1}{4\pi}\left\langle (\boldsymbol{B}\cdot\nabla) B_z \right\rangle_{xy} + \mathcal{D}, \tag{4.3}$$

where the total mean pressure is

$$P = \left\langle p_{\mathrm{th}} \right\rangle_{xy} + \frac{1}{8\pi}\left\langle |\boldsymbol{B}|^2 \right\rangle_{xy} + \left\langle \rho U_z^2 \right\rangle_{xy}, \tag{4.4}$$

p_{th} is thermal gas pressure, ρ is the gas mass density, g_z is the vertical gravitational acceleration, and $\mathcal{D}$ represents diffusion terms, including numerical diffusion. Here, ρU_z^2 is the sum of turbulent and ram pressures. I do not attempt to separate the turbulent and ram pressure components since the bulk motions such as wind or fountain flow are an essential part of vertical force balance. I compute and

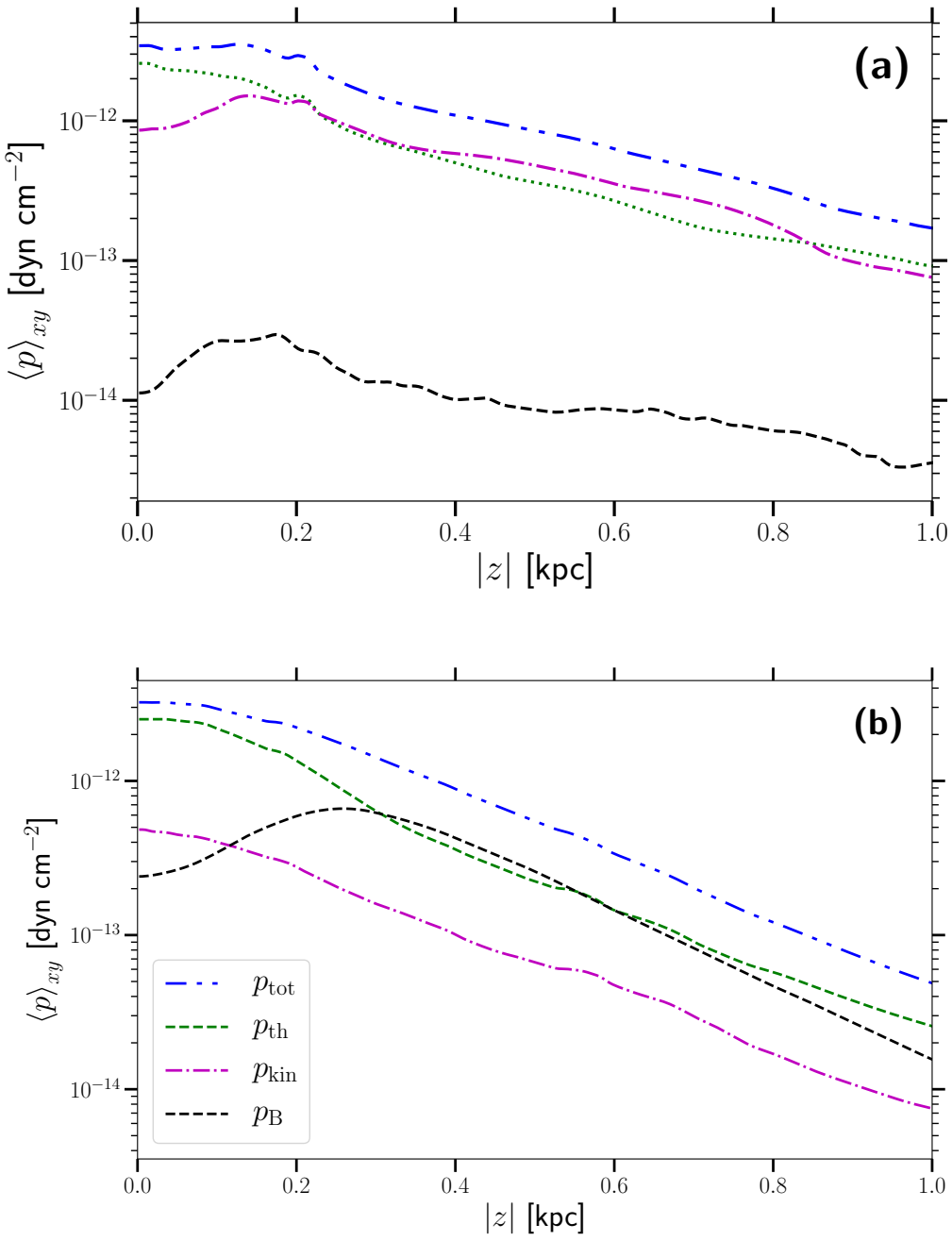

Figure 4.8: Vertical profiles of the total pressure, $p_{\rm tot} = p_{\rm th} + p_{\rm kin} + p_{\rm B}$, thermal pressure $p_{\rm th}$, turbulent pressure $p_{\rm kin}$, and magnetic pressure $p_{\rm B}$, and their variation as the system evolves from the **(a)** Early to **(b)** Late stage.

compare individual terms in this equation but, since the physical diffusion is just one contribution to the momentum dissipation, I do not include the diffusion term in the analysis that follows. This should be kept in mind when discussing the force balance but this does not affect our conclusions regarding the relative magnitudes of various terms. The derivation of this equation, in the absence of diffusion, is provided in Appendix C.

Figure 4.9 show the vertical profiles of the individual terms in the vertical momentum equation (4.3) for the Early (upper row), Transitional (middle) and Late (bottom) stages, respectively. The contribution of gravity is shown in all panels with solid blue for reference. The magnetic pressure gradient and tension are negligible in the Early stage, Fig. 4.9 **a**, when the magnetic field is still growing exponentially and has minor dynamical significance. The thermal pressure gradient (dotted, magenta) is close to balance with the gravity force, exceeding it most notably around $|z| = 0.2\,\mathrm{kpc}$ to drive the systematic gas outflow. The turbulent pressure gradient (dash-dotted, green) is subdominant. This picture remains qualitatively similar in the Transitional stage but the magnetic pressure gradient (dashed, black) already makes a noticeable contribution to the force balance. The importance of magnetic pressure increases in the Late stage where it assists gravity to confine the gas layer at $|z| < 0.3\,\mathrm{kpc}$, but combines with thermal pressure against gravity at larger distances from the midplane. Horizontally averaged magnetic tension (solid, blue) opposes the magnetic pressure gradient but this force is subdominant at all times and all altitudes. The turbulent pressure gradient is also weak.

Altogether, the vertical force balance is dominated by gravity and the thermal pressure gradient. Contrary to the suggestion of Boulares & Cox (1990), magnetic tension is negligible within $|z| \lesssim 1\,\mathrm{kpc}$ and I expect it is unlikely to become more important at larger altitudes.

4.6 Vertical distribution of the mean magnetic field

A notable and unexpected feature of the distribution of the magnetic field is that it has its maximum away from the midplane as shown in Fig. 4.10. In the Late stage, the maximum of the mean field strength is located around $|z| \simeq 250\,\mathrm{pc}$, while for

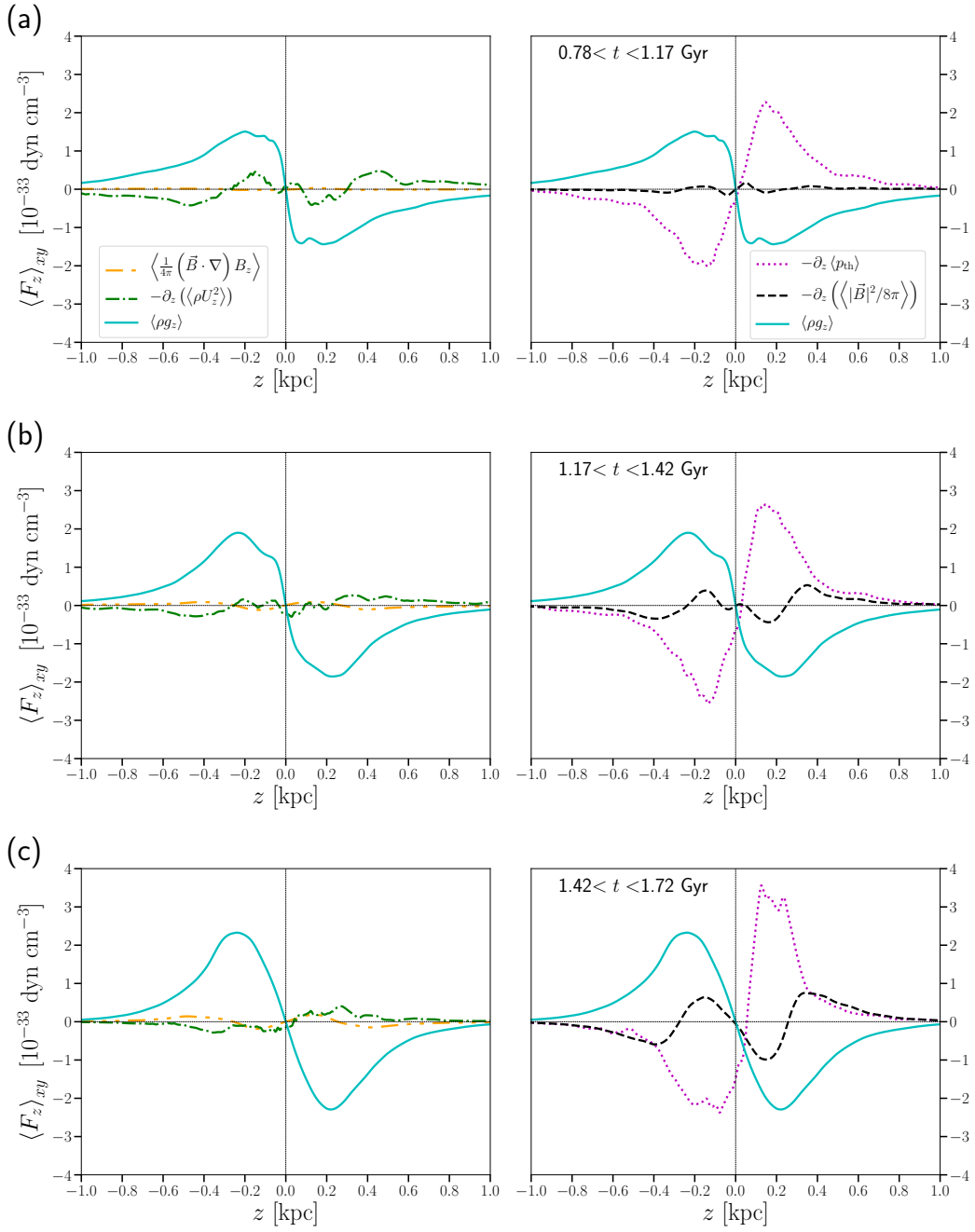

Figure 4.9: Horizontal averages of the individual terms in the vertical momentum equation (4.3) in the (**a**) Early, (**b**) Transitional and (**c**) Late stages, from top to bottom. The vertical profile of the gravity force (solid, light-blue) is shown in all panels for reference, thermal and magnetic pressure gradients are shown dotted (magenta) and dashed (black), respectively, and magnetic tension and turbulent pressure gradient are shown solid (blue) and dash-dotted (green), respectively.

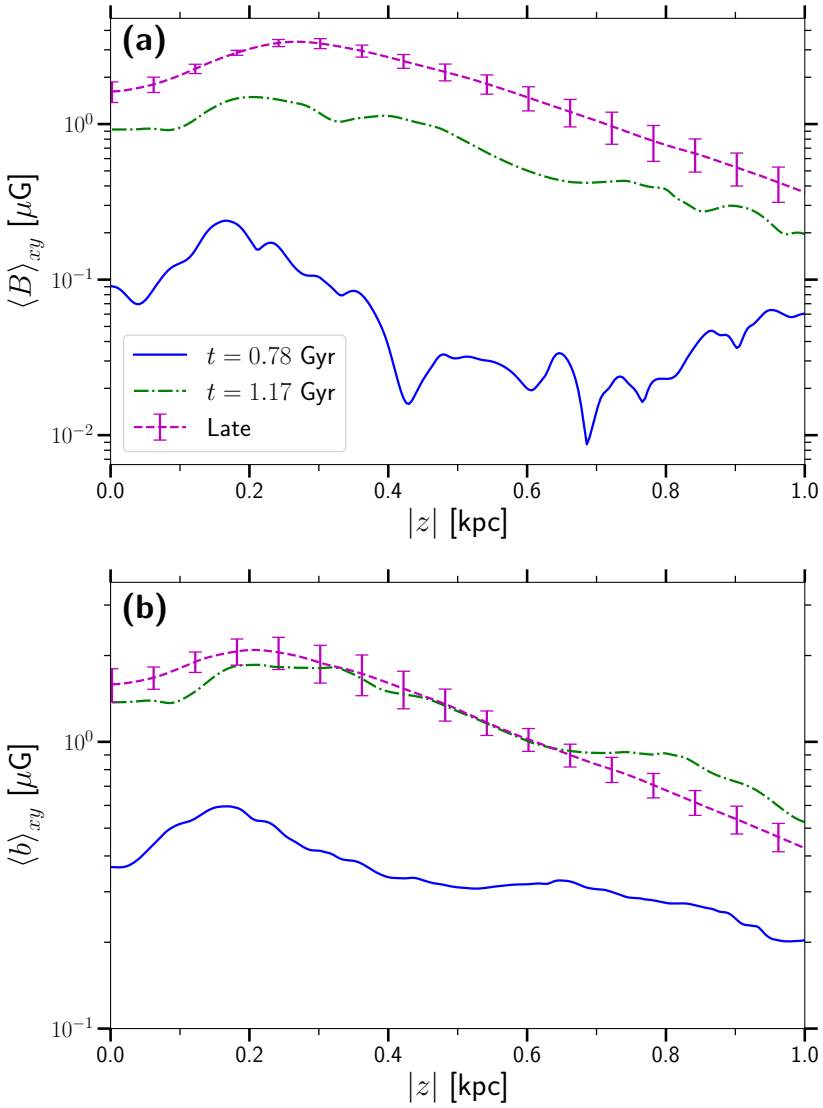

Figure 4.10: The vertical profiles of **(a)** mean and **(b)** random magnetic field strength in the Early (blue, dashed) and Late (magenta, solid) stages.

the random field it is slightly nearer the midplane at $|z| \simeq 200\,\mathrm{pc}$.

The mean magnetic field can be redistributed from the midplane by turbulent diamagnetism, i.e. the transport of the mean magnetic field from a region with enhanced turbulence at an effective speed of $-\frac{1}{2}\nabla\eta_\mathrm{t}$, where

$$\eta_\mathrm{t} \simeq \frac{1}{3}\tau u_0^2 \simeq \frac{1}{3}u_0 l_0,$$

is the turbulent magnetic diffusivity, τ and l_0 the correlation time and length of the

flow, u_0 its rms speed (Zeldovich, 1957; Roberts & Soward, 1975). The correlation length, l_0, of the random velocity in the warm gas increases from about 70 to 100 pc between $|z| = 0$ and 0.4 kpc, whereas u_0 decreases from 13 to 4 $\mathrm{km\,s^{-1}}$, over the distance $\Delta z = 0.4$ kpc (Table 3 of Hollins *et al.*, 2017*a*). Thus,

$$-\frac{1}{2}\nabla\eta_\mathrm{t} \simeq -\frac{1}{6}\frac{\Delta(l_0 u_0)}{\Delta z} \simeq 0.2\,\mathrm{km\,s^{-1}},$$

where Δ denotes the increment in the corresponding variable. With these estimates, the maximum of the mean magnetic field would be displaced away from the midplane by a distance of $-\frac{1}{2}t\nabla\eta_\mathrm{t} \simeq 120$ pc over a period of 0.6 Gyr. While this cannot fully account for the location of maximal field strength in Fig 4.10, turbulent diamagnetism probably contributes to the transport of mean magnetic field. The magnetic pressure exceeds the turbulent (kinetic) pressure at $|z| > 0.2$ kpc (as shown in Fig. 4.8), which also suggests that magnetic field is systematically transported away from its generation region.

Since a significant part of the random field is generated by tangling of the mean field by the random flow, it is understandable that both have a maximum away from $z = 0$ kpc.

Another factor that could contribute to the non-monotonic variation of the magnetic field strength with $|z|$ is a similarly non-monotonic distribution of intensity of dynamo action, quantified by the dynamo number. However, careful assessment of this possibility requires sophisticated dedicated analysis, which is beyond the scope of this Thesis.

As mentioned above, I do not suggest that the vertical profiles shown in Figures 4.3 and 4.10 necessarily occur in the Milky Way or any other specific galaxy but rather argue that this behaviour is physically meaningful and that its possibility should be kept in mind in the interpretation of observations and the assessment of various effects of interstellar magnetic fields.

4.7 Summary

I have found a significant qualitative difference between magnetic effects in our model (in agreement with the results of Bendre *et al.* (2015)) and those models

adopting strong *imposed* magnetic fields. Any numerical model of this kind must provide an initial value and spatial configuration for the magnetic field. If a strong imposed field is used, then it is crucial to use a spatial configuration which reflects the configuration of the evolved magnetic field.

I find that systematic outflow speed is reduced throughout the disc and disc-halo interface as the magnetic field grows, approximated by Eq. (4.2). Below $|z| = 300\,\mathrm{pc}$ the magnetic pressure gradient opposes the outflow of gas driven by thermal pressure. I, and Bendre *et al.* (2015), find that there is a rapid decrease in U_z for $B_\mathrm{h}/B_\mathrm{eq} > 0.1 - 0.3$. Models with imposed magnetic fields do not capture this effect, which is vital to modelling how outflows feed the galactic halo.

Magnetization of the simulated ISM leads to an increase in the density of hot gas, particularly close to the midplane where hot gas is produced by SNe. However, I also find that fractional volume of hot gas decreases by up to an order of magnitude from the Early to the Late stage, due to an increased cooling rate and a reduced outflow speed of the hot gas. This is evident in the visualisation shown in Fig. 4.2, with the hot gas structures becoming more compact as the magnetic field grows.

I do not include SN clustering in our simulations since the size of such clusters, identified with OB associations, is comparable to the horizontal size of the computational domain, which is approximately 1 kpc. The SN clustering in such a relatively small region is better simulated as a time variation of the SN rate. The random variations of the SN rate in our simulations mimics the clustering.

The changes outlined above combine to produce a qualitative change in the vertical density profile of ISM gas between the Early and Late stages. Once the magnetic field has reached a steady state, the density profile is flatter within 300 pc of the midplane. Above this height the density decreases more rapidly with distance from the midplane compared to the Early stage.

Part III

The effect of magnetic fields on supernova explosions

Chapter 5

Magnetic effects on individual supernova explosions

5.1 Overview

Results presented in Chapters 3 and 4 show that fractional volume and mass of hot gas, in numerical simulations of the ISM, decrease as the magnetic energy becomes dynamically significant. There are clear signs, in Fig. 4.2, that hot gas structures become smaller in the non–linear stage of the simulation. While a number of factors contribute to the decreasing gas temperature, it is possible that the properties of hot gas are altered by the magnetic field during the injection stage by SNe.

5.2 Introduction

My initial aim is twofold: to examine the effects of large-scale magnetic fields in isolation, and to assess the claim that large-scale magnetic fields do not affect momentum injection in SN remnants. In order to make direct comparison, I use similar parameters to numerical models from earlier studies.

SN explosions are a major component of larger-scale numerical models of galaxies, evolving turbulence in which SN remnants are more realistically embedded. Remnant-scale modelling provides necessary constraints on the critical aspect of en-

ergy injection to apply in the larger simulations. However, a less idealized model will ultimately be required for comparison with SN remnant observations. None the less, starting with an idealised model is useful for two reasons:

1. Attempting to extract the effects of any particular dynamical process or physical variable, such as the magnetic field, in non-linear, compressible turbulence simulations of the ISM requires untangling of dynamical processes which interact (often in a non-linear manner) with each other. Introducing new physics gradually will enable clearer comparisons, and an incremental development of understanding.

2. There are a number of results concerning the evolution of SNe using both HD and MHD simulations, which use an idealised set up for the ambient gas. When I first ran these simulations, I did so with the intention of reproducing known results before running SNe simulations with more physics included. However, I have found a number of new results which I discuss in this chapter.

In Section 5.3, I present details of the numerical model, which uses the PENCIL code. I then discuss magnetic effects on the aspect ratio of SN remamnts in Section 5.4. This is followed examination of the effect of large-scale magnetic fields on momentum injection by SN remnants in Section 5.5. In Section 5.6 I discuss magnetic effects on the thermodynamical properties of SN remnants. Residual energy injection by the remnants into the ISM is measured in Section 5.7 and I consider the critical magnetic field strength for MHD effects to become important in Section 5.8. I present a summary and discussion of results in Section 5.9.

As a sanity check I perform shock-tube experiments which verify the qualitative results are not sensitive to numerical recipes or parameters. These are external to the focus of the chapter, so I discuss them in Appendix E.1. I explore the effect of physical parameters on 1D HD and MHD shocks. Section E.2 provides a preliminary set of results on the effects of large-scale magnetic fields on 1D shocks in ambient gas densities ranging from $n = 10^{-2}\,\mathrm{cm}^{-3}$ to $n = 10^{-2}\,\mathrm{cm}^{2}$.

5.3 Numerical methods

Here I explore further the MHD effects, especially momentum injection, the anisotropy of the remnant, and effects on the gas and density distribution within the remnant. I use the Pencil Code[1], adapted for highly compressible nonideal MHD turbulence.

The MHD equations applied include the compressible form of the continuity equation

$$\frac{D\rho}{Dt} = +\dot{\rho}_{\rm SN} - \rho\nabla\cdot\boldsymbol{u} + \zeta_D\nabla^2\rho + \boldsymbol{\nabla}\zeta_D\cdot\boldsymbol{\nabla}\rho, \tag{5.1}$$

where ρ is the gas density and $\dot{\rho}_{\rm SN}$ is the mass of the SN ejecta, which for the purposes of these experiments is set to zero. An artificial shock dependant mass diffusion, ζ_D, is required for numerical stability in simulations of the SN-driven turbulent ISM. $\zeta_{\rm D} \propto f_{\rm shock}$, where

$$f_{\rm shock} = \left\langle \max_5 \left[(-\nabla\cdot\boldsymbol{u})_+\right] \right\rangle \left(\min\left(\Delta x, \Delta y, \Delta z\right)\right)^2. \tag{5.2}$$

This is described in Gent *et al.* (2019), along with shock dependant diffusivities included in the following equations. The material derivative is

$$\frac{D}{Dt} = \frac{\partial}{\partial t} + \boldsymbol{u}\cdot\boldsymbol{\nabla}.$$

The momentum equation evolving velocity, $\boldsymbol{u}$, includes an artifical shock dependent viscosity, ζ_ν and a momentum conserving correction term for ζ_D from Equation (5.1). The pressure force is expressed in terms of specific entropy, s, specific heat capacity of the gas at constant pressure, c_p, and sound speed, c_s, yielding

$$\begin{aligned}\rho\frac{D\boldsymbol{u}}{Dt} = &-c_s^2\rho\boldsymbol{\nabla}\left(\frac{s}{c_p} + \ln\rho\right) + \boldsymbol{\nabla}\cdot(2\rho\nu\boldsymbol{\nabla}\mathbf{S}) + \boldsymbol{j}\times\boldsymbol{B} \\ &+\rho\boldsymbol{\nabla}\left(\zeta_\nu\boldsymbol{\nabla}\cdot\boldsymbol{u}\right) - \boldsymbol{u}\left(\zeta_D\nabla^2\rho + \boldsymbol{\nabla}\zeta_D\cdot\boldsymbol{\nabla}\rho\right).\end{aligned} \tag{5.3}$$

This also includes the Lorentz force due to the magnetic field, $\boldsymbol{B}$, and the current density, $\boldsymbol{j} = \mu_0^{-1}\boldsymbol{\nabla}\times\boldsymbol{B}$. The vacuum magnetic permeability is denoted μ_0. Viscous stresses are accounted for through the shear viscosity ν within the divergence of the

[1] https://github.com/pencil-code

rate of strain tensor S, defined by

$$2\mathsf{S}_{ij} = \frac{\partial u_i}{\partial x_j} + \frac{\partial u_j}{\partial x_i} - \frac{2}{3}\delta_{ij}\boldsymbol{\nabla}\cdot\boldsymbol{u}, \quad \text{with} \quad \mathsf{S}^2 \equiv \mathsf{S}_{ij}\mathsf{S}_{ij}.$$

The energy equation is evolved in the form of the specific entropy with

$$\begin{aligned} \rho T\frac{Ds}{Dt} &= \dot{\sigma}_{\rm SN} + \rho\Gamma - \rho^2\Lambda + 2\rho\nu\mathsf{S}^2 + \eta\mu_0|\boldsymbol{j}|^2 \\ &\quad +\boldsymbol{\nabla}\cdot(c_p[\chi+\zeta_\chi]\rho\boldsymbol{\nabla}T) \\ &\quad -c_{\rm v}\,T\left(\zeta_D\nabla^2\rho + \boldsymbol{\nabla}\zeta_D\cdot\boldsymbol{\nabla}\rho\right), \end{aligned} \tag{5.4}$$

where T denotes the gas temperature and c_v the specific heat capacity of the gas at constant volume. Heat sources and sinks include SN explosion thermal energy, $\dot{\sigma}_{\rm SN} = 10^{51}$ erg at time $t = 0$, and viscous and Ohmic heating, in which η denotes the resistivity. As applied in Gent *et al.* (2013), the radiative cooling, Λ, applies Wolfire *et al.* (1995*b*) at lower temperatures and Sarazin & White (1987*a*) for the hot gas. Diffuse UV-heating, Γ, follows Wolfire *et al.* (1995*b*). Thermal conductivity, χ and shock dependant ζ_χ are applied, and an energy conserving correction term due to ζ_D from Equation (5.1).

The induction equation is solved in terms of the vector potential, $\boldsymbol{A}$, which conserves $\boldsymbol{\nabla}\cdot\boldsymbol{B} = 0$ by design. In contrast to the previous equations I do not include any shock capturing resistivity, as this has the unphysical effect of suppressing magnetic field in the SN remnant shell through excessively rapid diffusion (reconnection). However, I am interested in investigating the nature of dynamo in the turbulent ISM, so isotropic resistivity is included to yield

$$\frac{\partial \boldsymbol{A}}{\partial t} = \boldsymbol{u}\times\boldsymbol{B} + \eta\boldsymbol{\nabla}^2\boldsymbol{A} + \boldsymbol{\nabla}\cdot\boldsymbol{A}\boldsymbol{\nabla}\eta. \tag{5.5}$$

The system of equations is completed by the ideal gas equation of state with adiabatic index $\gamma = c_p/c_v = 5/3$. The monatomic gas with hydrogen and helium abundances representative of the Solar neighbourhood of the Milky Way has mean molecular weight 0.531 when assumed to be fully ionised. A comprehensive description of the Pencil Code application to SN driven ISM turbulence is given in Gent (2012, Chapter 3), while the further enhancement of shock handling and stability methods for reproducing SN blast waves in HD are presented in Gent *et al.* (2019).

Here, I consider a plane-parallel uniform magnetic field $\boldsymbol{B} = (0, B_0, 0)$, for $B_0 \in [0, 5]\,\mu$G. With a fiducial gas number density, n_0, for the ambient ISM of $1\,\mathrm{cm}^{-3}$ and resolution 0.5 parsec along each side, I use a Cartesian grid of 528^2 by 576 parallel to the field. For consistent thermal pressure in the ambient ISM throughout the duration of the model blastwaves I set a thermal equilibrium temperature of $T \simeq 2500\,\mathrm{K}$ (Wolfire *et al.*, 1995*b*, see Figure 3) and (Sánchez-Salcedo *et al.*, 2002, see Figure 1).

The numerical model uses constant magnetic resistivity, $\eta = 8 \cdot 10^{-4}\,\mathrm{kpc\,km\,s^{-1}}$ and sound speed dependent viscosity, $\nu = \nu_0 c_\mathrm{s}$, where $\nu_0 = \Delta x = 5 \cdot 10^{-4}\,\mathrm{kpc}$ is the grid resolution, and c_s is the speed of sound. A test of alternate Prandtl numbers produced qualitatively similar solutions, and results were convergent with resolution of 0.5 pc, other than a thinner more dense remnant shell.

The SN energy (10^{51} erg) is injected into an injection site at the centre of the simulation domain $(0, 0, 0)$ with radius 6 pc in a Gaussian profile centered of the injection site. The energy injected into the site is purely thermal.

5.4 SN remnant aspect ratio

I show the radial profiles of gas density in Figure 5.1, perpendicular and parallel to the magnetic field, for models with $B_0 = 0, 0.5$ and $5\,\mu$G. With a weak magnetic field $B_0 \leq 1\,\mu$G, the evolution of the remnant is very similar to the HD model. With stronger B_0 the remnant core is less diffuse, and the slightly less dense remnant shell parallel to the field is coincident with the HD model shell. However, perpendicular to the field the mass profile of the remnant is substantially altered. Mass is more confined within the remnant, but Figure 5.1 also shows that the SN shockwave propagates faster perpendicular to the magnetic field while carrying less mass at the shock front. Panel (a) shows that these magnetic effects are already noticeable by 400 kyr into the evolution of the remnant.

Figure 5.2**(a)** shows the shockwave at 2 Myr compressing magnetic field lines to form a dense magnetic collar. Magnetic field is initially evacuated from the core of the remnant. It is evident that the MHD remnant core geometry resembles a prolate spheroid with the polar radius parallel to the magnetic field. The ratio of polar to equatorial radius increases with field strength. In contrast, the remnant shock front

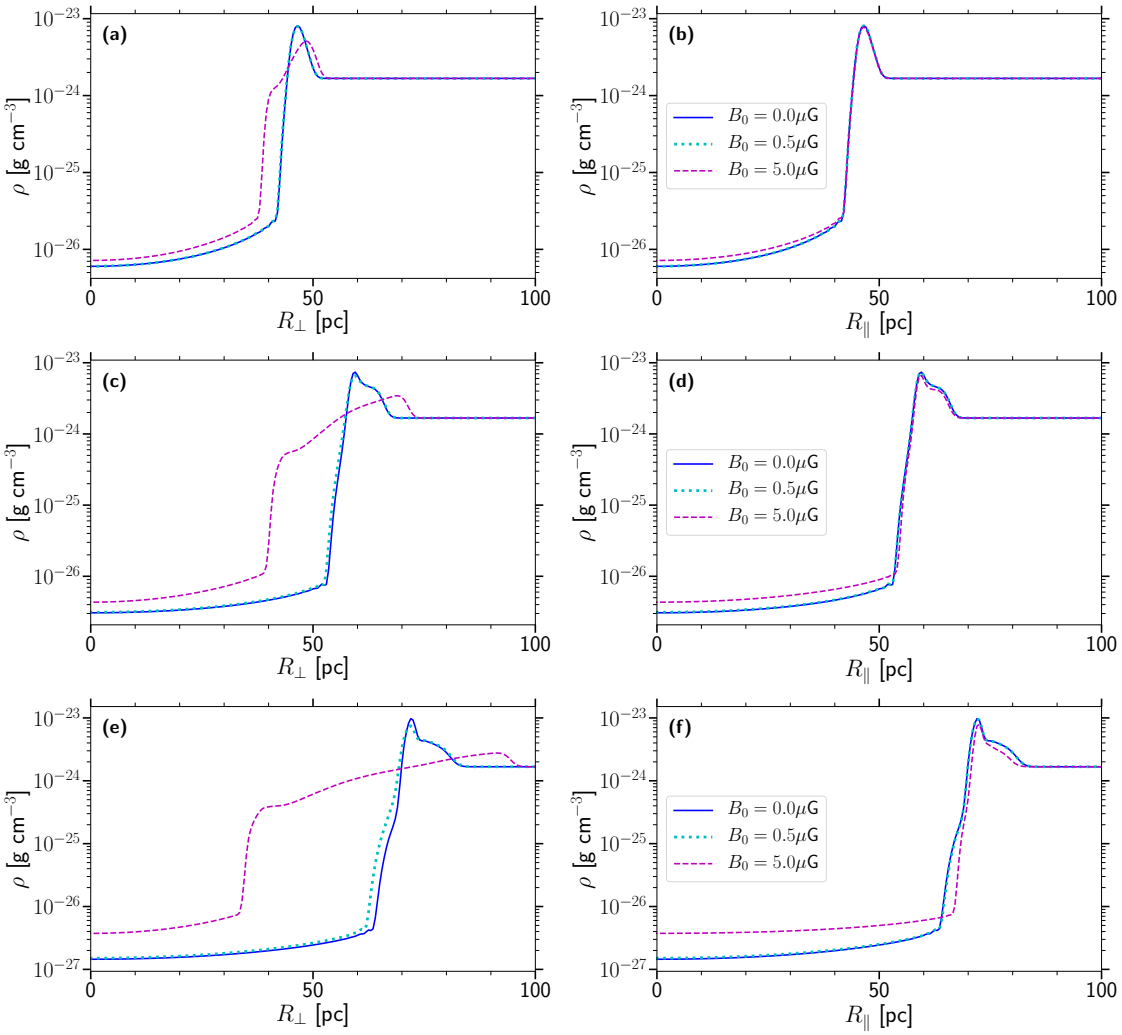

Figure 5.1: Radial profiles of gas density perpendicular (left column) and parallel (right column) to the magnetic field at $t = 400\,\mathrm{kyr}$ (top row) $t = 1\,\mathrm{Myr}$ (middle row) and $t = 2\,\mathrm{Myr}$ (bottom row).

forms the surface of an oblate spheroid with equatorial radius perpendicular to the magnetic field. This ratio of polar to equatorial radius decreases with field strength.

Figure 5.2**(b)** shows the structure of flows driven by the remnant in a strongly magnetized ambient ISM. The shockwave drives outward flows as expected. I find inward flows of comparable speed to the outward flows. There are retrograde shocks towards the core in all the models, but for the HD and weakly magnetic models these carry negligible mass. For strong B_0 the magnetic forces drive inward gas flow from the shell, perpendicular to the magnetic field. As the flow approaches the thermally dominated core, the outward thermal pressure gradient channels the flows parallel

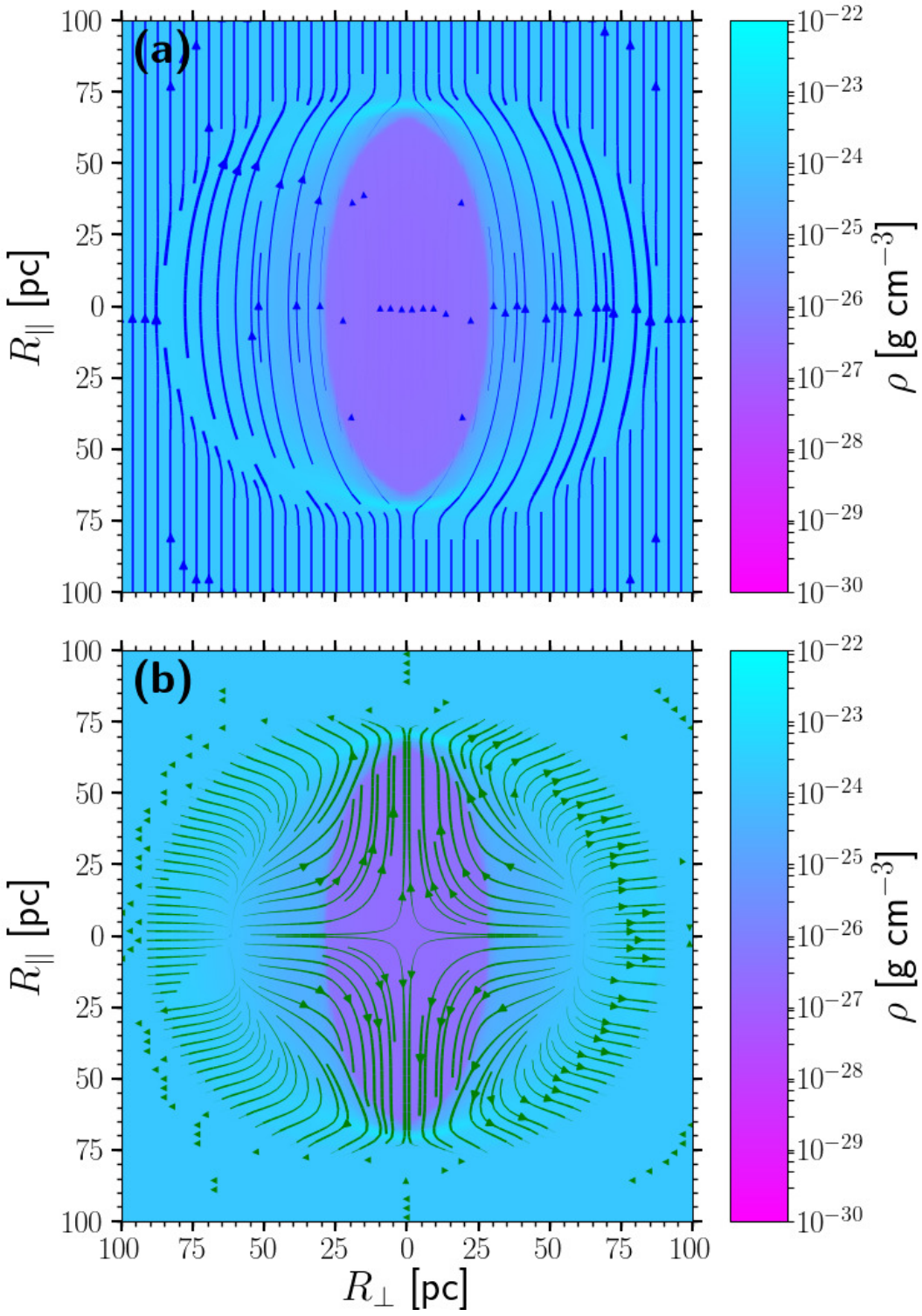

Figure 5.2: Cross-section of the strongly magnetized remnant at 2 Myr, with **(a)** magnetic field lines and **(b)** velocity stream lines overlaid. Line thickness is proportional to field strength.

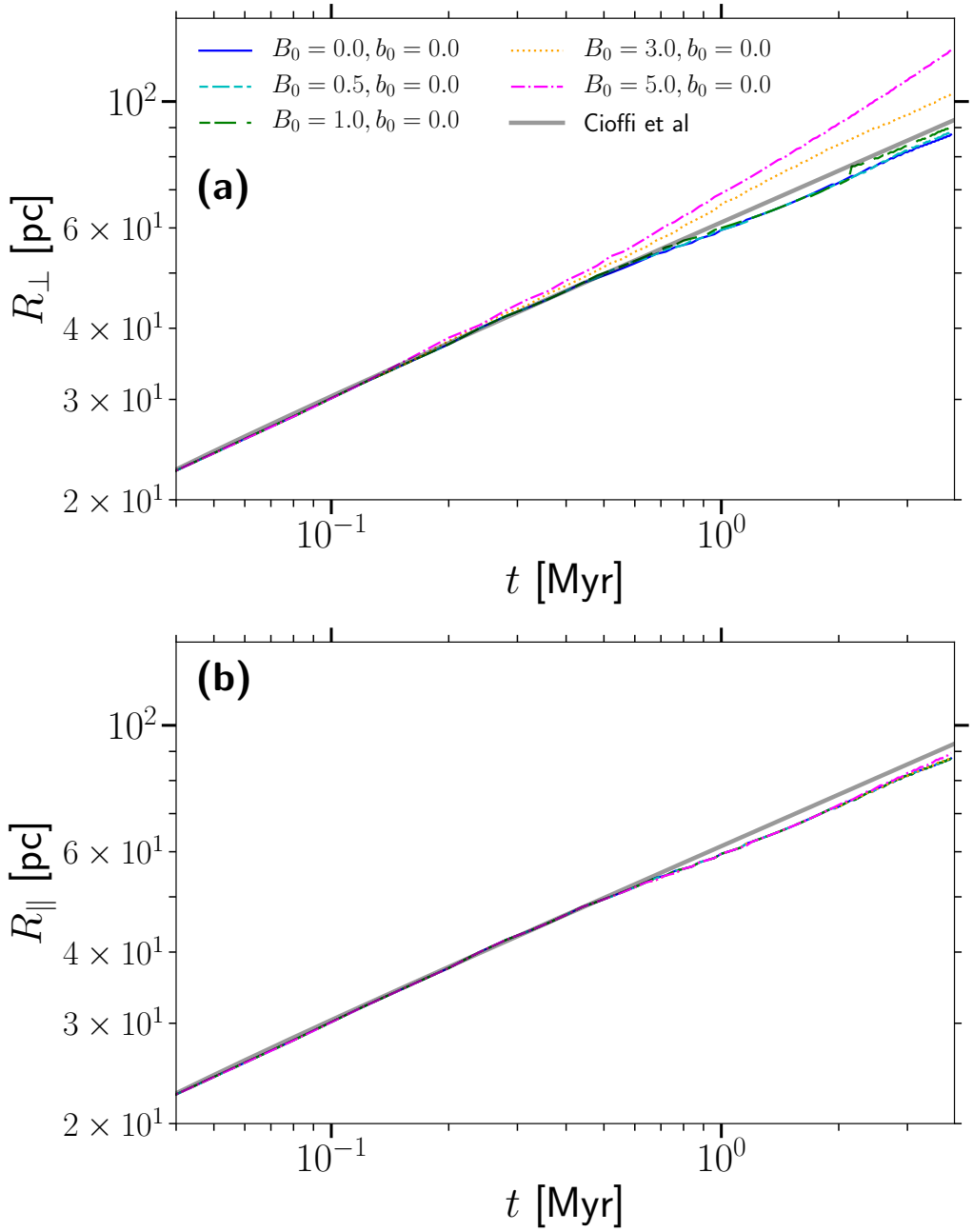

Figure 5.3: SN remnant radius, $R_\perp$, perpendicular and $R_\parallel$, parallel to B_0. Numerical solutions are compared to the HD analytical solution (Cioffi *et al.*, 1988).

Table 5.1: Details of fits for $R_\perp(t) = R_0(t/1\ \mathrm{Myr})^\alpha$.

Parameter	B_0 [μG]				
	0	0.5	1.0	3.0	5.0
R_0 [pc]	59	59	59	66	70
α	0.28	0.28	0.28	0.34	0.39

to the magnetic field, creating a quadrupolar velocity field between the shockwave and core. In the HD and weakly magnetized remnants, the internal gas flows of the remnant remain radially outward.

By 2 Myr the magnetic field along with some of the gas, has filled almost half the remnant void behind the shock front. This forms an inter-shock region between the core of the remnant and its shell. At even later times the field strength throughout the inter-shock region is close to its original strength. The gas in the core remains hot and diffuse, with magnetic field strength considerably weaker than outside the core.

Figure 5.3 shows the radial evolution of the shockwave for the HD, weakly magnetized and strongly magnetized remnants. The HD remnant has a single characteristic length; the shockwave radius, since the shockwave and core are coupled. This shows good agreement with the analytical solution of Cioffi *et al.* (1988) for a spherically symmetric model[2]. Shock wave radii are near identical for all models, parallel to the magnetic field. The weakly magnetized remnant behaviour in Figure 5.3 closely resembles that of the HD remnant. However, perpendicular to the strongly magnetized field the shockwaves diverge from the other profiles near $t = 200$ kyr. When a profile of the type, $R_\perp \propto t^\alpha$ is fitted, with fit parameters shown in Table 5.1, I find that α increases with magnetic field strength, which shows that the shock propagates faster perpendicular to the magnetic field for stronger magnetic fields. Details of the curve fitting are provided in Appendix D.

Given the ubiquity of magnetic fields in the ISM, it is reasonable to anticipate spheroid morphology to be common in SN remnants. This may be useful in understanding the 3D structure of observed remnants. For example, G351.0-5.4, dis-

[2]After 700 kyr, there is a small difference between the Cioffi *et al.* (1988) analytical solution and the HD shock radii in both directions. However, Cioffi *et al.* (1988) truncate cooling below $T \sim 10^4$ K and Gent *et al.* (2019) show that the late-stage difference between the analytical and numerical solutions is a due to further cooling.

covered in de Gasperin *et al.* (2014) is modelled in first approximation as spherical. This may be reasonable for observations of the shell, which from the models appears only slightly oblate, but misleading for the remnant core. Alternatively, comparisons of gamma-ray and radio data around remnant W44 (Cardillo *et al.*, 2014) indicate a smaller spheroid in gamma-ray emission with polar radius offset from the surrounding spheroid in radio emission, and the presence of magnetic field in the shock $B \geq 10^2\,\mu$G. Complex interaction with molecular clouds and the turbulent ISM affect the morphology of the remnant, but the inter-shock region may also be part of the explanation for the misalignment in the observational profiles.

Modelling the local bubble of the Milky Way with a prolate sphere Alves *et al.* (2018) find this a reasonable fit even for the magnetic shell. In contrast to the findings, they determine the remnant field to be vertical, out of alignment to the neighbourhood galactic field, and highly anisotropic between North and South. Perhaps, however, an oblate spheroid shell with polar axis parallel to the galactic plane would be an alternative model consistent with the galactic magnetic field.

Any speculation about how the results relate to observational features, is highly tentative at this stage. The large scale alignment of magnetic fields in the ISM will surely not be uniform on scales of a few parsecs. The structure of the turbulent magnetic field, the stratification and inhomogeneity of the gas density and temperature, and the turbulent motion of the ambient ISM will be considered in future work, let alone the effects of chemistry and ionization on the observational signatures. Anisotropy of SN remants may of course also arise independent of magnetic effects.

5.5 Magnetic effect on momentum injection by SNr

5.5.1 SN merge time

Before considering the momentum injection by an individiual remnant, I consider the time taken for the SN to 'merge' into the surrounding gas, which is the time at which the shock speed becomes comparable to the ambient speed of sound, $\dot{R} \sim c_{\rm s}$.

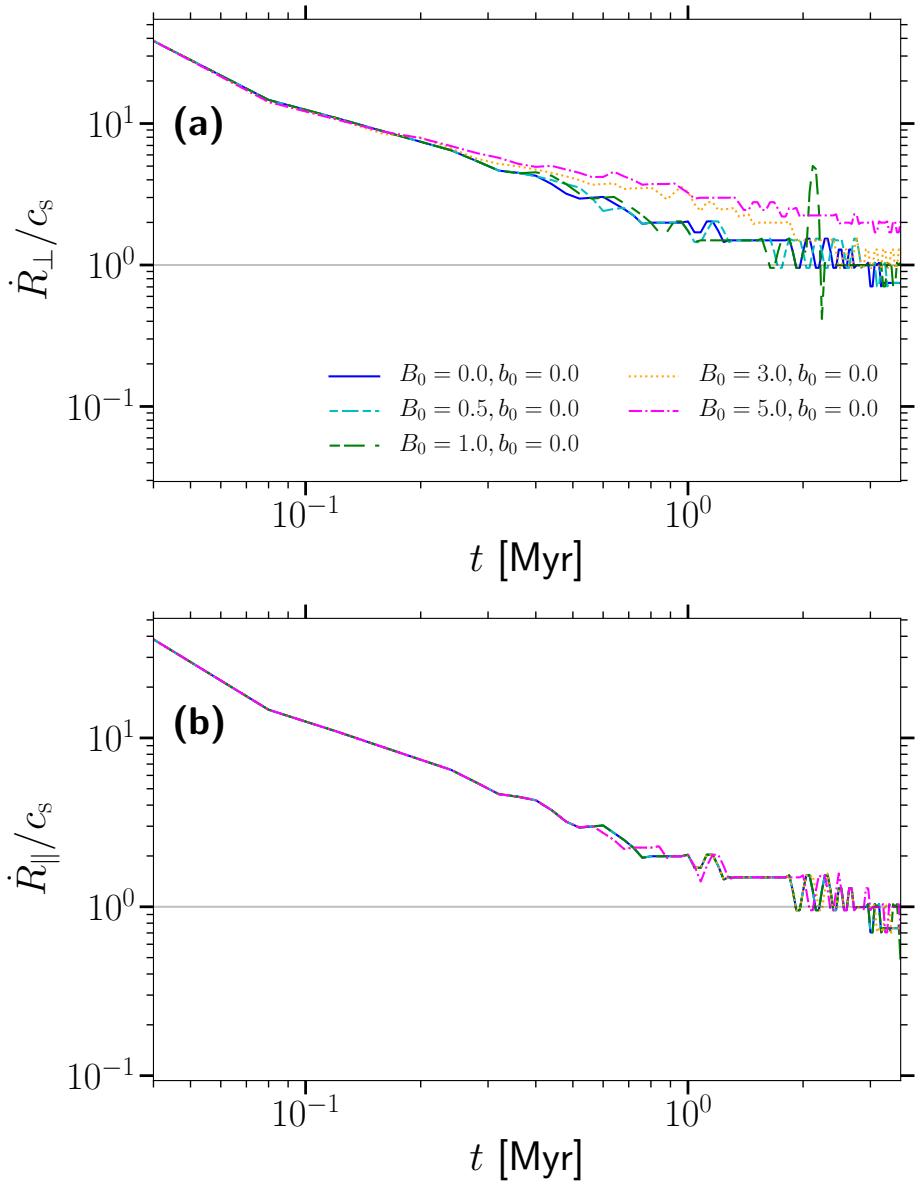

Figure 5.4: Mach speed at the shock **(a)** perpendicular and **(b)** parallel to the magnetic field.

In this numerical set up, with ambient temperature $T \sim 2500\,\mathrm{K}$, ambient sound speed is $c_s \sim 8\,\mathrm{km\ s^{-1}}$.

I define the Mach speed of the SN shock as $\dot{R}_\perp/c_s$ and $\dot{R}_\parallel/c_s$ perpendicular and parallel to the magnetic field, respecively. In the parallel direction, all the SN shock for all models become subsonic after 2 Myr. Similarly for weak B_0, the perpendicular shock also becomes subsonic after this time. However, for $B_0 \geq 3\mu$G, the increase

in shock speed results in a delay in the shock becoming subsonic. For the $B_0 = 5\mu$G model, the shock still has not become subsonic. Nevertheless, for the purposes of exploring momentum injection by the remnants, I use 2 Myr as the effective merge time with the surrounding gas. None the less, there is the possibility that magnetic effects persist beyond this merge time, owing to the magnetically enhanced shock velocity perpendicular to the large-scale magnetic field. Given that the SN shock effectively 'decouples' from the core perpendicular to magnetic field, it could be considered a separate entity after the merge time. Even if it did not further enhance momentum injection, it could continue to effect the local thermodynamical properties.

However, this is better viewed tentatively for now, as such an idea would need to be tested in a model which accounts for local gas density inhomogeneities and other interacting shocks which are a ubiquitous in the ISM.

5.5.2 Momentum injection

In a typical HD supernova explosion, the propagation of the shock, and subsequent momentum injection into the surrounding medium, is dominated by the thermal pressure gradients, which evacuate mass from the core into the blastwave. In a very similar physical set up to mine, Kim & Ostriker (2015) find the SN terminal momentum injection to be about $4 \times 10^5\,\mathrm{M}_\odot\,\mathrm{km\,s^{-1}}$, defined by

$$M u_n = \int_\mathrm{V} \rho\,(\boldsymbol{u} \cdot \hat{\boldsymbol{n}})\,\mathrm{d}V, \tag{5.6}$$

where $\hat{\boldsymbol{n}}$ is the radial unit vector from the centre of the SN explosion.

I consider this calculation with a modification to account for non-spherical expansion of the SN remnant. The most general approach would be to adopt a tri-axial ellipsoid profile. However in this case, the remnants have two distinct length scales, the SNR radius parallel and perpendicular to the magnetic field, $R_\parallel$ and $R_\perp$, respectively. This change produces a bi-axial ellipsoidal remnant, rather than the spherical HD remnants. The ellipsoidal surface is represented by

$$g(\mathbf{x}) = \left(\frac{x}{R_\perp}\right)^2 + \left(\frac{y}{R_\parallel}\right)^2 + \left(\frac{z}{R_\perp}\right)^2, \tag{5.7}$$

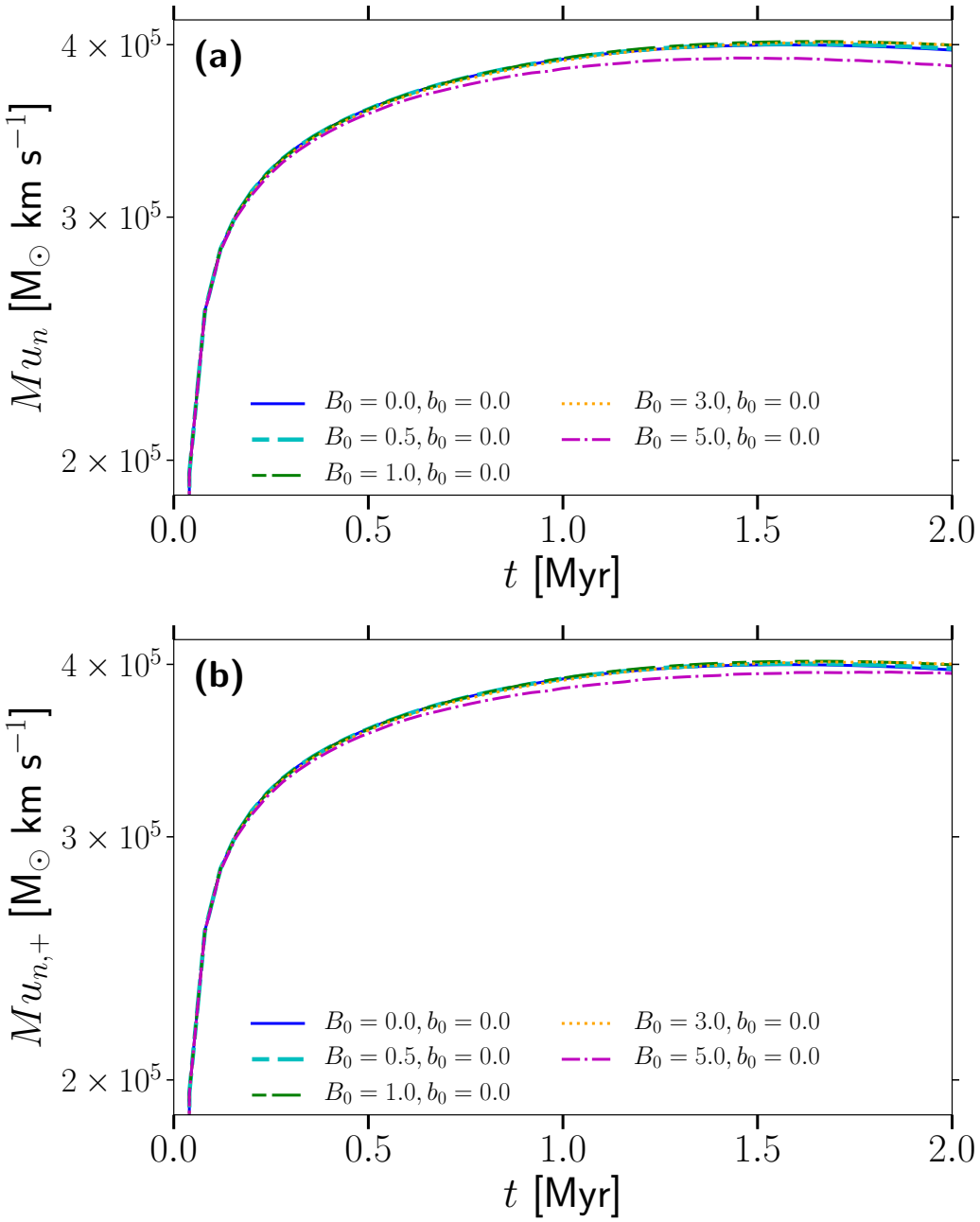

Figure 5.5: Time evolution of **(a)** total and **(b)** outward momentum injection for a number of SN models with magnetic field strengths $B_0 \in [0, 5]$ μG. Momentum, at a given snapshot, is calculated as $\int_\mathrm{V} \rho\,(\boldsymbol{u} \cdot \hat{\boldsymbol{n}})\,\mathrm{d}V$, where $\hat{\boldsymbol{n}}$ is the radial unit vector from the centre of the SN explosion.

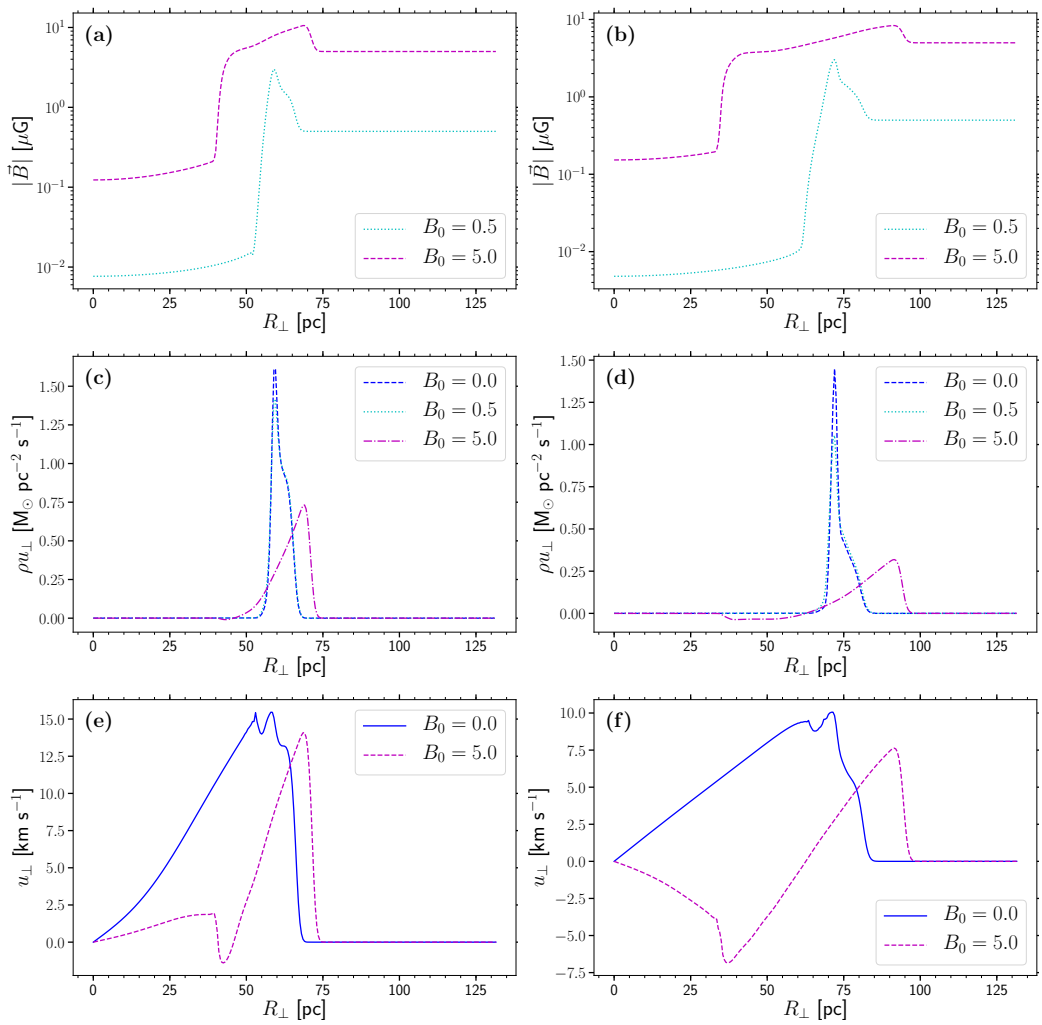

Figure 5.6: Radial profiles perpendicular to the magnetic field at 1 Myr (left column) and 2 Myr (right column) of magnetic field strength (top row), momentum (middle row) and velocity (bottom row).

where x and z are the directions perpendicular to the magnetic field, and y is parallel to the magnetic field. Here $g(\boldsymbol{x}) = 1$ represents the remnant shell.[3] I now define the normal to the shell as

$$\hat{\boldsymbol{n}} = \frac{\nabla g}{|\nabla g|},$$

where

$$\nabla g = \left(\frac{2x}{R_\perp^2}, \frac{2y}{R_\parallel^2}, \frac{2z}{R_\perp^2} \right).$$

It can be shown that $R_\perp = R_\parallel$ leads to a spherical remnant profile and $\hat{\boldsymbol{n}} = \hat{\boldsymbol{x}}$.

[3] $g(\boldsymbol{x}) = k$, where $0 \leq k \leq 1$, represent contours of the remnant.

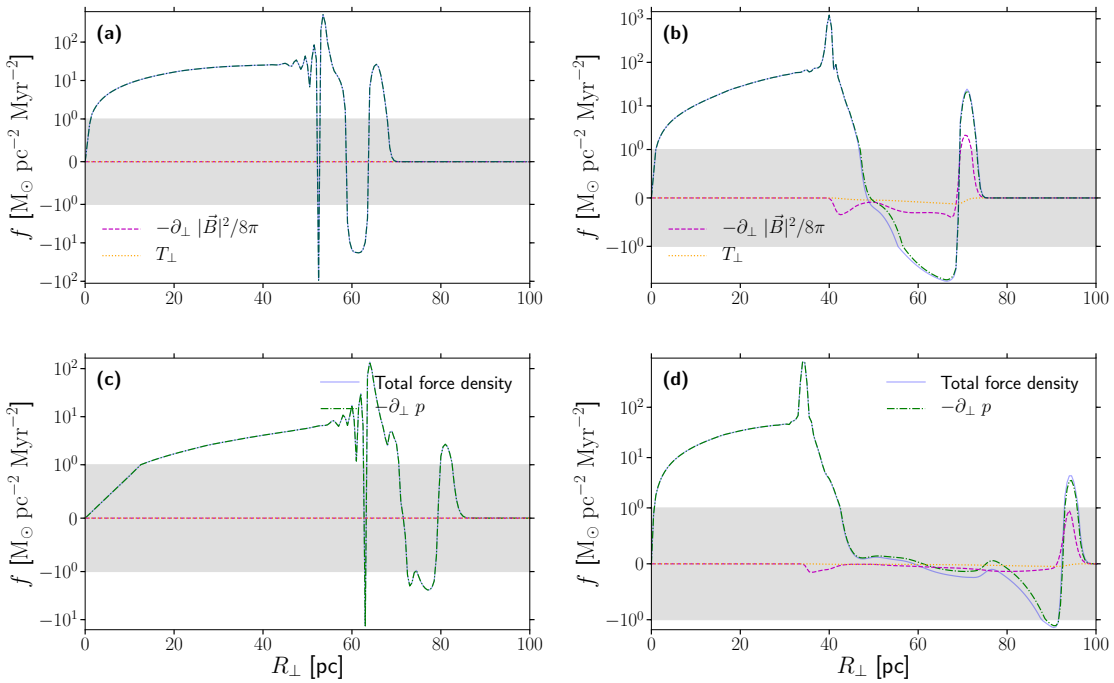

Figure 5.7: Force density, f perpendicular to magnetic field with the HD (left column) and $B_0 = 5\mu$G (right column) models at at $t = 1$ Myr (top row) and $t = 2$ Myr (bottom row). The vertical scale across the shaded area is linear and logarithmic elsewhere.

With this definition for $\hat{\boldsymbol{n}}$ applied to Equation (5.6), I obtain total momentum injection $4 \times 10^5\,\mathrm{M}_\odot\,\mathrm{km\,s^{-1}}$ for the HD remnant, similar to Kim & Ostriker (2015). I plot the evolution of total momentum for the HD and a range of MHD remnants in Figure 5.5 **(a)**. As the thermal pressure gradient reduces in the remnant the pressure driven snowplough (PDS) transitions to the momentum conserving snowplough (MCS), as described by Cioffi *et al.* (1988).

Figure 5.5(a) In terms of overall momentum injection, the HD and MHD models are very similar (if not identical). Momentum injection is only marginally reduced for the $B_0 = 5\mu$G model, which is likely to be explained by inward momentum injection. In fact, in Panel (b), I present only the outward momentum injection, and find that all models are very similar until the SN merges with the surrounding gas.

Kim & Ostriker (2015) find that momentum injection ceases within two to three shell-forming times, before the magnetic energy becomes comparable to the thermal energy in the shell. Subsequently, they argue that magnetic effects will not lead to further momentum injection by the remnant.

While the quantitative results agree, it is clear that the presence of the magnetic field changes the way in which momentum is injected, despite not affecting the overall momentum injection profile in these models. It is perhaps worth noting that where the local large-scale field is stronger than 5μG, we may expect to see quantitative changes to momentum injection.

To illustrate what is changing due to the strong MHD I show radial profiles perpendicular to the magnetic field at 1 Myr and 2 Myr in panels (a) and (b), respectively in Figure 5.6 of the magnetic field strength (top), velocity (centre) and momentum (bottom).

Momentum in the shell of the HD remnant is a factor of 4–6 higher and centered narrowly about the shock front. The MHD shock in all profiles is broader, projecting both in advance of the HD shock position and including an extended weak inward momentum behind the shock front. Even though inward momentum is weak compared with the outward momentum at the SN shock, it is clearly dominant over the minimal outward momentum of the hot, diffuse core, as seen in Figure 5.6(c) and (d). Panels (c) and (d) show that the HD model does not feature inward gas motion, which explains the absence of inward momentum in the HD models.

In order to explore how momentum injection changes in MHD remnants, I consider the momentum equation perpendicular to B_0,

$$\rho\frac{Du_\perp}{Dt} = -\frac{\partial}{\partial R_\perp}\left(p + \frac{|\boldsymbol{B}|^2}{2\mu_0}\right) + \frac{1}{\mu_0}\left(\boldsymbol{B}\cdot\boldsymbol{\nabla}\right)B_\perp + \mathcal{D}, \tag{5.8}$$

where p denotes thermal pressure and $\mathcal{D}$ refers to diffusive terms in the equation. For the analysis, I am interested in the interaction between the pressure gradient terms and the magnetic tension term on the right hand side of the equation.

For the strong MHD model Figure 5.7 shows the forces applying perpendicular to B_0 at $t = 1$ Myr, Panel **(a)** and $t = 2$ Myr **(b)**. Interestingly, the very large thermal pressure gradient extending through the inner core to about 40 pc at 1 Myr is confined to only 40 pc by 2 Myr. A negative thermal pressure gradient does evolve in the wake of the shock, and this is true also for the HD remnant. The negative thermal pressure gradient region is wider in the MHD shock than in the HD. However this is too remote from the core to account for its confinement late on. Magnetic effects are sub-dominant but gradually become more significant at the blastwave, primarily

the magnetic pressure gradients, where the outward magnetic pressure gradient is an order of magnitude smaller than the thermal gradient at $t = 1\,\mathrm{Myr}$, and 4 times smaller at $t = 2\,\mathrm{Myr}$. Despite being subdominant, the magnetic pressure gradient provides a 10% and 25% increase in force density at the shock by 1 Myr and 2 Myr, respectively.

However, the negative pressure gradient in the wake of the shock appears to be the most interesting. The negative force applies throughout the *intershock region*, between the primary blast wave and the core. It effectively causes mass to be peeled away from the remnant shell and driven inwards along with some of the magnetic field. This broadens the mass shell profile I see from Figure 5.1 and the magnetic field profile from Figure 5.6 (top panels) and provides the substantive forces confining the remnant core compared to HD. For most of the $40 < R_\perp < 70\,\mathrm{pc}$ region by 2 Myr the magnetic pressure gradient dominates the thermal pressure gradient. Magnetic tension is subdominant perpendicular to the magnetic field.

5.6 Thermodynamics of MHD remnants

The effect of confinement of the remnant core by the inward magnetic pressure gradient is to reduce adiabatic cooling compared to HD. The system is non-adiabatic, so how does the redistribution of mass in the strong MHD case affect its thermal properties? Snapshots of the net heating, $\Delta H = T^{-1}(\Gamma - \rho\Lambda)$, are presented in Figure 5.8 for the HD model, Panel **(a)**, and strong MHD model, **(b)**. In the HD and weak MHD models, cooling dominates everywhere in the remnant, except for a thin layer just behind the cooling shell. In the strong MHD model cooling dominates in the confined remnant inner core and shell, but in the inter-shock region perpendicular to the field UV-heating exceeds radiative losses. In Figure 5.1 **(a)** this applies for $35 \lesssim R_\perp \lesssim 60\,\mathrm{pc}$.

In Figure 5.9 I show the probability density functions (PDFs) of temperature, **(a)**, and gas density, **(b)**. Each panel features the respective PDFs for models with $B_0 = 0$, 0.5 and $5\,\mu\mathrm{G}$ at $t = 2\,\mathrm{Myr}$. All models have identical initial temperature and gas density distributions. The peaks at $T \simeq 2500\,\mathrm{K}$ and $\rho \simeq 1.67\,\mathrm{g\,cm^{-3}}$ identify the ambient ISM. For the HD model and model with $B_0 = 0.5\mu\mathrm{G}$, the differences in the PDFs are otherwise also negligible. The other local maxima identify the cold

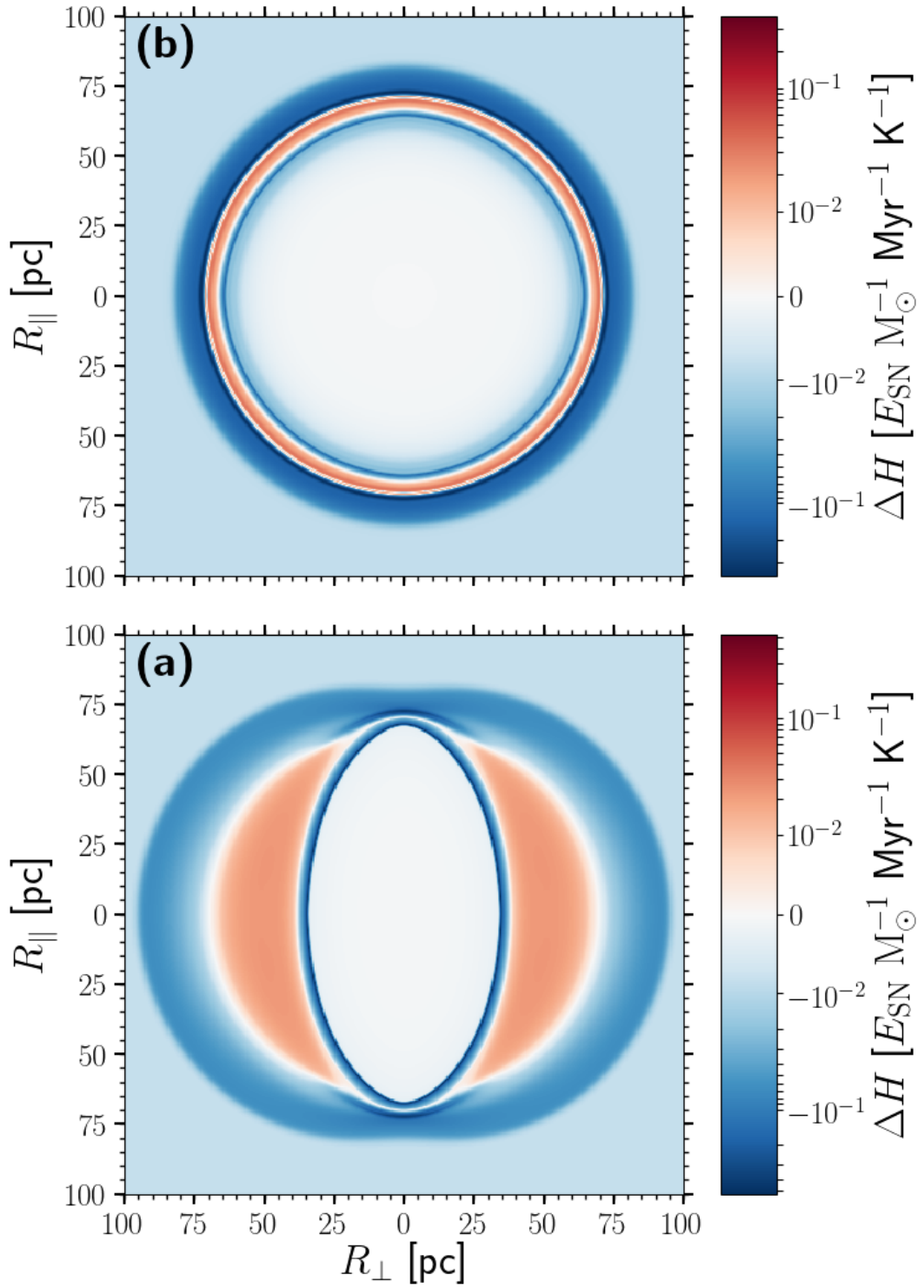

Figure 5.8: Cross sections at 2 Myr for the HD model, **(a)**, and the model with $B_0 = 5\mu$G, **(b)**, of the net heating, $\Delta H = T^{-1}(\Gamma - \rho\Lambda)$.

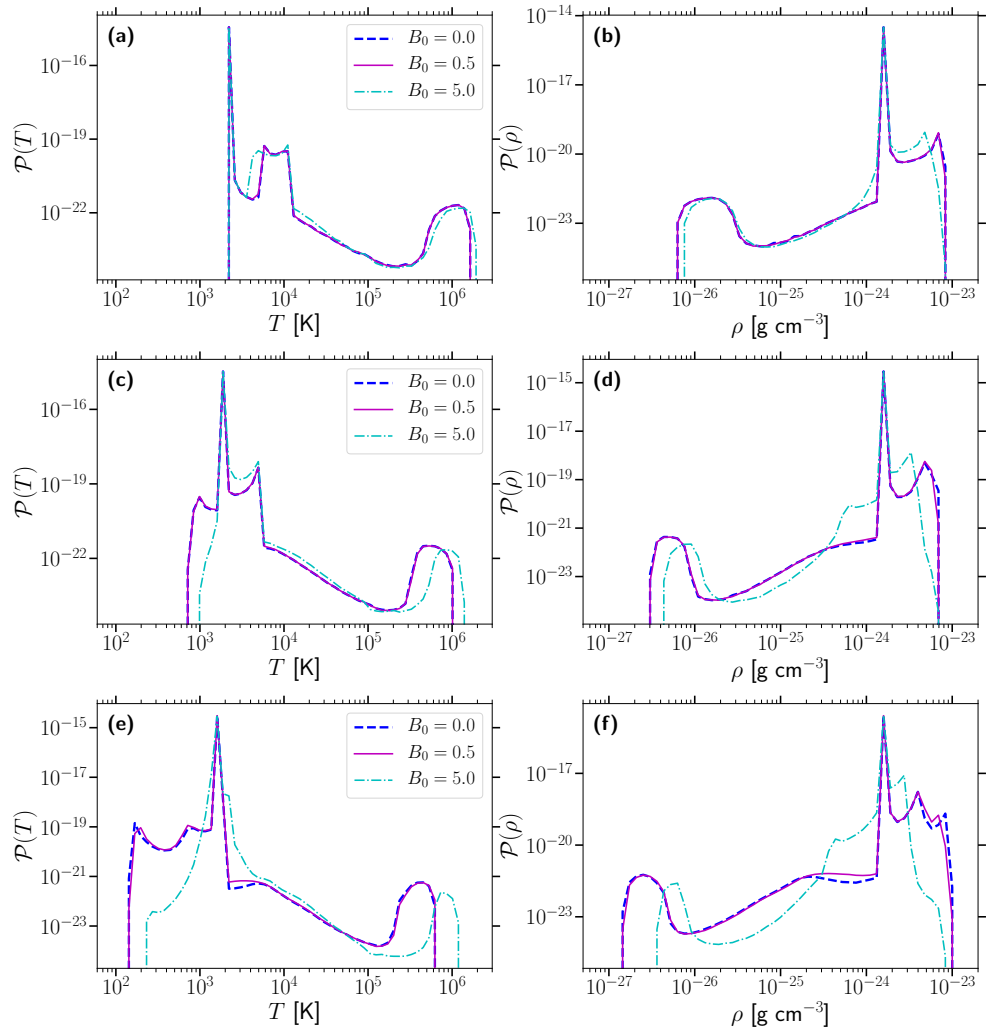

Figure 5.9: Mass-weighted probability density functions (PDFs) of gas temperature (left column) and gas density (right column) at 400 kyr (top row), 1.0 Myr (middle row), and 2.0 Myr (bottom row), for HD (dashed blue) and MHD models with $B_0 = 0.5\mu$G (solid cyan) and $B_0 = 5.0\mu$G (dash-dotted magenta) models.

remnant shell ($n > 10\,\mathrm{cm}^{-3}, T < 100\,\mathrm{K}$), the hot diffuse core ($n < 0.01\,\mathrm{cm}^{-3}, T > 10^5\,\mathrm{K}$), and the accumulation of thermally stable warm gas ($n \simeq 0.1\,\mathrm{cm}^{-3}, T \simeq 2 \times 10^3\,\mathrm{K}$).

However, with the strong magnetic field the peak temperatures representing the remnant shell and the remnant cores are hotter and more dense. Its magnetically confined hot gas has a smaller fractional volume. Hot gas in all models cools slowly, due to the low density, but the strong MHD hot gas cools due to radiative losses relatively faster due to its slightly higher density. It nevertheless remains hotter, be-

cause the adiabatic cooling is reduced. The strong MHD model has almost identical temperature distribution in the range $10^4 < T < 10^5\,\mathrm{K}$, although more dense.

Perhaps the strongest effect of a strong magnetic field is on the dense, cold gas. For the HD and weak magnetic field models, there is a clear probability density peak at $T \sim 150\,\mathrm{K}$ and $n \sim 10\,\mathrm{cm}^{-3}$. In the presence of a strong field, there is considerably less probability density for $T < 2 \times 10^3\,\mathrm{K}$, the temperature distribution truncates at $T \sim 200\,\mathrm{K}$, and there is much less high density gas. This indicates that the presence of the magnetic field inhibits the formation of cold, dense regions of gas.

Magnetic confinement of hot gas in the remnant is indicated strongly by the increasing mean hot gas density plotted in Figure 5.10 **(a)** and decreasing fractional volume from Figure 5.10 **(b)** of hot gas in strongly magnetized remnants. This effect has also been found in larger-scale simulations of the ISM (Evirgen *et al.*, 2017, 2019). The residual total mass of hot gas deposited into the ISM may be 20–40% greater in the strong MHD remnant as depicted in Figure 5.10 **(c)**.

In Figure 5.11 I show radial profiles perpendicular to the magnetic field at 1 Myr **(a)** and 2 Myr **(b)**, for temperature (top) and thermal pressure (bottom) for the HD and strong MHD remnants. This illustrates the higher temperature in the MHD core, but smaller fractional volume.

5.7 Residual SN energy injection

The increased mass of hot gas and reduced effect of non-adiabatic cooling within an MHD remnant invites the question how are the energetics of the ISM affected by a strong magnetic field? The time evolution of residual SN total energy and each contribution to the energy are plotted in Figure 5.12.

In Panel (a), I introduce an energy retention term

$$\Delta E_{\mathrm{tot}}(t) = E_{\mathrm{th}}(t) + E_{\mathrm{kin}}(t) + \Delta E_{\mathrm{mag}}(t),$$

where $\Delta E_{\mathrm{mag}}(t) = E_{\mathrm{mag}}(t) - E_{\mathrm{mag}}(t=0)$. This term examines energy retained by the system without the initial energy of the large-scale magnetic field, which varies by two orders of magnitude from the weakest to strongest large-scale field used here.

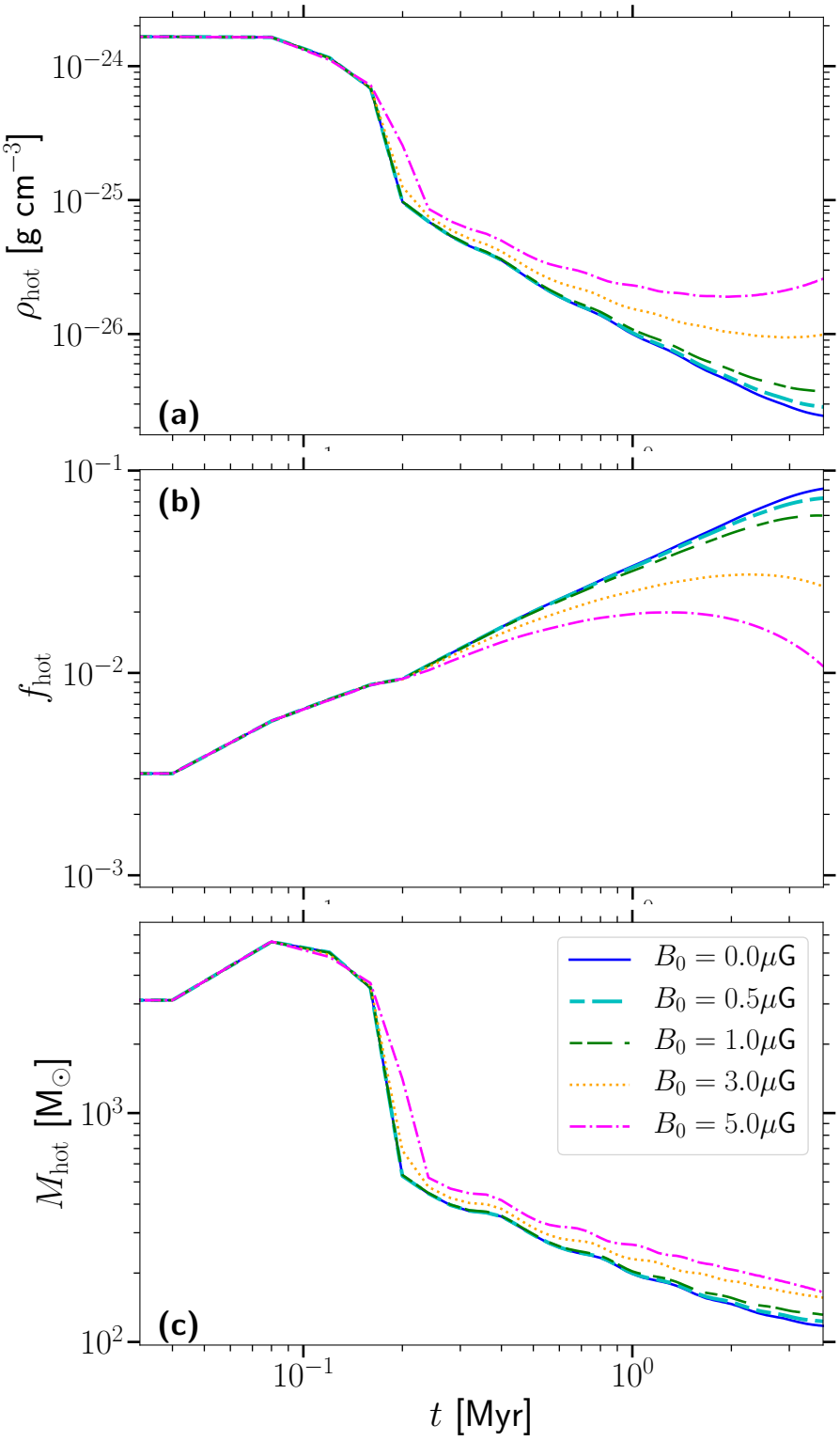

Figure 5.10: Time evolution of **(a)** mean density of hot gas **(b)** fractional volume of hot gas **(c)** mass of hot gas for the HD (solid blue) and MHD models with $B_0 = 0.5\mu$G. Hot gas is defined as $T > 2 \cdot 10^4$ K (Kim & Ostriker, 2015).

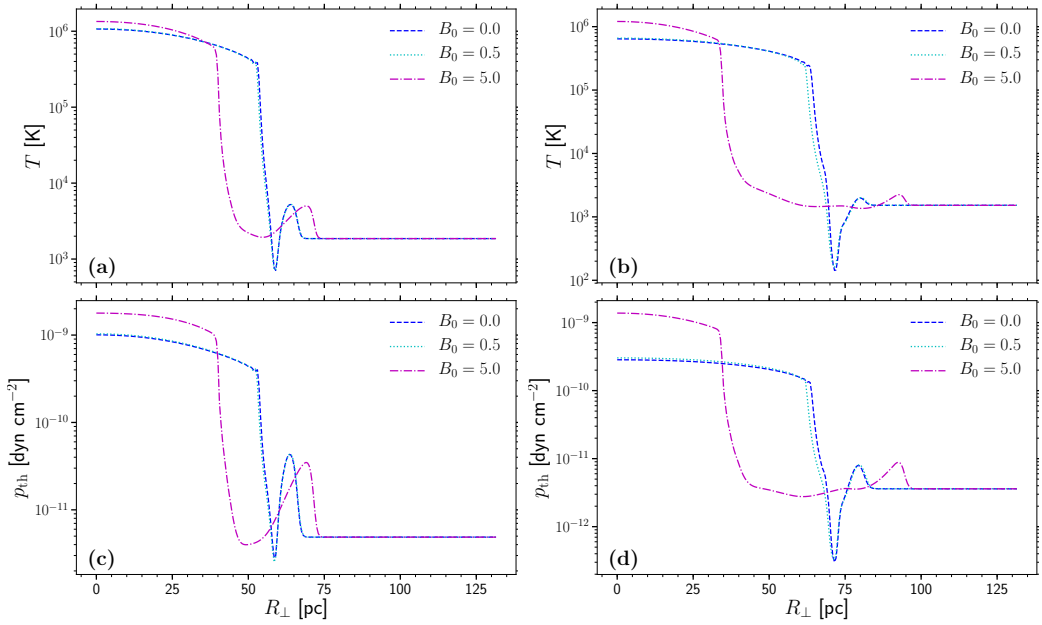

Figure 5.11: Radial profiles at **(a)** 1 Myr and **(b)** 2 Myr perpendicular to the magnetic field of gas temperature (top) and thermal pressure (bottom).

Panel (a) shows that the $B_0 = 5\mu$G model retains up to 10% more energy than the HD case by 2 Myr. The two profiles diverge within a few hundred kyr. The weak magnetic field models have identical energy retention as the HD model.

From Panel **(b)** I see that the presence of strong large-scale magnetic fields retains marginally more residual thermal energy, while Panel **(c)** shows that kinetic energy in the MHD remnants is lost marginally more quickly.

For all MHD models there is a modest amplification of the magnetic field though compression and tangling (Panel **(d)**). So the net contributions of thermal and magnetic energy mean that the MHD shocks in fact induce a greater total residual energy into the ISM than HD alone.

5.8 Critical magnetic field strength

Any qualitative differences between the HD and MHD remnants must arise from effects due to the Lorentz force. Inspection of the evolution of magnetic tension reveals this to be negligible, relative to the magnetic and thermal pressure gradients. The maximal tension forces apply in the remnant shell nearest the polar axis of the

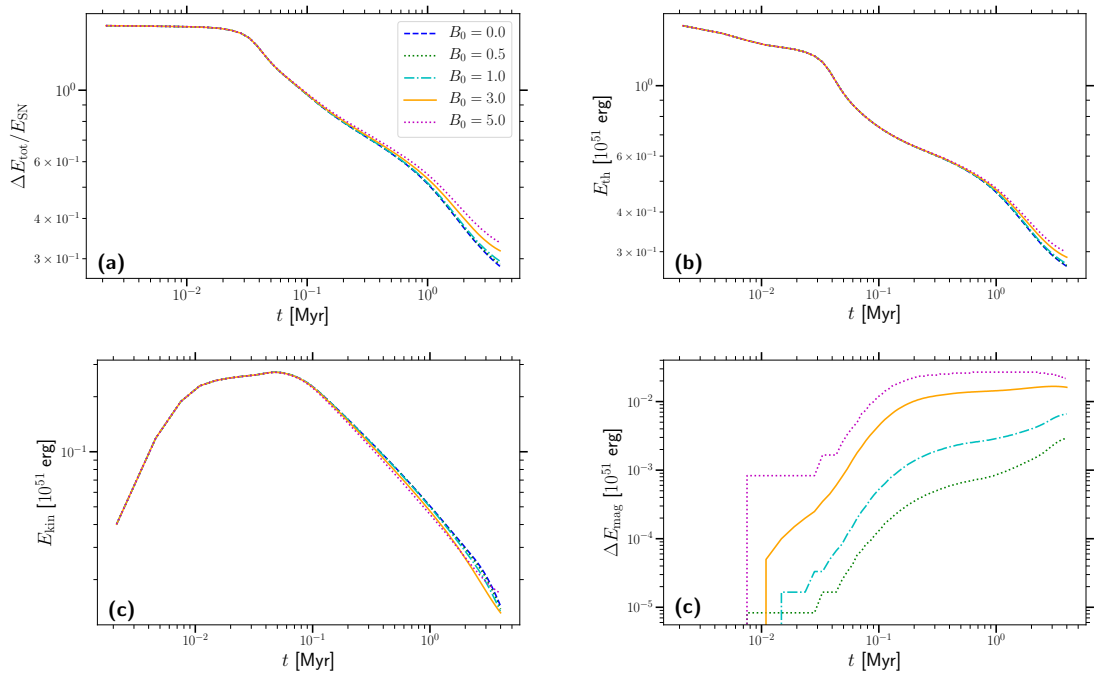

Figure 5.12: **(a)** Energy retention by HD and MHD (5μG remnants, where $\Delta E_{\rm tot}(t) = E_{\rm tot}(t) - E_{\rm tot}(t=0)$. $E_{\rm tot}(t=0)$ is the total energy in the ambient gas prior to the SN explosion, **(b)** thermal energy **(c)** kinetic energy and **(d)** magnetic energy profiles.

remnant.

Therefore, modification to momentum injection relies on the interacting radial pressure gradients, particularly where $\partial_\perp (p) \simeq \partial_\perp (|\boldsymbol{B}|^2/2\mu_0)$. In the blast wave the magnetic gradient will grow due to compression. The stronger the ambient field, the earlier the magnetic gradient in the shell and in its wake will acquire a critical strength sufficient to significantly modify the remnant evolution. The MHD shell begins to shed mass into its wake, compared to HD as early as 200 kyr for $B_0 = 5\mu$G, 320 kyr for 3μG and 920 kyr for 1μG. The leading shock outstrips the HD model at 440, 560 and 1560 kyr, respectively. From both panels in Figure 5.7 throughout the inter-shock region I have

$$\frac{\partial_\perp (|\boldsymbol{B}|^2/2\mu_0)\,|_-}{\partial_\perp (p)\,|_+} \gtrsim 1,$$

but when the MHD shock profiles start to diverge from HD this ratio locally is still much less than 1. A reasonable criteria for identifying the critical large-scale magnetic field strength may be to assume plasma-β <1. Hence, $B_{\rm crit} \sim \sqrt{2\mu_0 p}$,

where $p = k_{\rm B} n T$; $k_{\rm B}$ is the Boltzmann constant, and T denotes temperature.

For these simulations the ambient ISM has $n = 1\,{\rm cm}^{-3}$ and $T \simeq 2500\,{\rm K}$. Thus, the gas is in thermal equilibrium with radiative cooling balancing UV heating. I obtain $B_{\rm crit} \sim 3\,\mu{\rm G}$, which is in agreement with Hanayama & Tomisaka (2006), who also finds that significant change to the nature of the remnant is seen for $B_0 \geq 3\mu{\rm G}$. However, the effect of cooling and heating processes are highly nonlinear functions of density, so I shall explore how to explain critical field strength with various ambient ISM densities and magnetic field configurations in future work.

5.9 Summary

The merger of the remnant shell with the surrounding gas depends on a number of factors, including but not limited to, ambient sound speed, homogeneity (or inhomogeneity) of the ambient gas density structures, and interaction with other shocks in a turbulent, highly compressible and typically inhomogeneous interstellar medium. However, the emergence of differences in energy retention, directly linked to the presence of large-scale magnetic fields, suggests that the efficiency with which the surrounding gas extracts energy from SN remnants is modified by magnetic fields and it needs to be studied with the inclusion of aforementioned physical effects.

A plane-parallel, micro-gauss strength magnetic field changes the aspect ratio of SN remnants. The shockwave through the ambient ISM propagates faster perpendicular to the magnetic field. Figure 15 of Caunt & Korpi (2001) show a similar MHD remnant expanding faster perpendicular to the plane-parallel field. This is also identified by Ferrière *et al.* (1991) in the context of a superbubble blast wave. They also report that the MHD blast is faster in the parallel direction than for HD. Conversely, the hot diffuse remnant core is magnetically confined into a prolate spheroid with pole aligned to the field. Hanayama & Tomisaka (2006); Kim & Ostriker (2015) also find that expansion of the core is inhibited perpendicular to a plane-parallel magnetic field.

Both effects are caused by the magnetic pressure gradients perpendicular to the magnetic field. In the adiabatic and pressure driven phases of the blast wave expansion, while magnetic forces are weak relative to the explosive forces, magnetic field is expelled from the core and compressed into the shell. Some energy from the ther-

mally driven outward shock is stored in the highly compressed field at the remnant shell, to be released through the magnetic pressure gradient in the late MHD shock. Compression also generates an increasingly negative magnetic pressure gradient just behind the shell, ultimately injecting momentum inwards.

In similar simulations, which focus on the early (up to 400 kyr) stage of SN evolution, Kim & Ostriker (2015) conclude that momentum injection by an SN remnant is unaffected by the presence of a plane-parallel magnetic field. They suggest magnetic fields will not affect momentum injection, because they do not become comparable to thermal effects before the remnant enters the momentum-conserving phase. I also find that large-scale magnetic fields (up to 5μG strength) have a marginal quantitative effect on momentum injection.

The strongest effect of a large-scale magnetic field is the confinement of the hot core and a more dense inter-shock region. UV-heating exceeds radiative losses in this region and, combined with the magnetic broadening of the shock front, inhibits the formation of cold gas, compared to HD.

There is a reduced fractional volume of hot gas, an effect also noted by Evirgen *et al.* (2019). Even though I obtain this result in an idealized numerical setup, Evirgen *et al.* (2019) find that hot gas becomes more dense in numerical simulations of the local Galaxy, as the magnetic field reaches $B_{\rm rms} \sim 3\mu$G strength with a strong large-scale component. These numerical simulations feature highly inhomogeneous gas density, compressible turbulence and a multi-phase ISM structure. Thus, it is plausible that remnant-scale simulations may relate to magnetic effects found in more sophisticated numerical models.

In its early stages the presence of a magnetic field has negligible effect on SN remnant evolution, and this is consistent with the results of Kim & Ostriker (2015). However, as the magnetic shell forms increasingly strong local pressure gradients the dynamics alter markedly. For sufficiently weak magnetic fields this may evolve so late that the blast wave has already merged with the ISM and it remains dynamically insignificant. For stronger fields the magnetic retrograde shock and late MHD shock occur sufficiently early to alter remnant momentum injection and structure. For gas density $n = 1\,{\rm cm}^{-3}$, I find the critical field strength to correspond to plasma-$\beta = 1$ in the ambient ISM. The magnetic confinement and late MHD shock occur earlier and are stronger as B_0 increases within the range $0.5 \leq B_0 \leq 5\mu$G considered. With

respect to structure, this is consistent with Hanayama & Tomisaka (2006), who find notiecable magnetic confinement of the remnant interior for $B_0 \geq 3\mu$G, and Kim & Ostriker (2015) for $B_0 = 7.2\mu$G.

Magnetic fields in the ISM are not uniform as applied in these models and planned studies shall include the effects of turbulent structure of the magnetic field and a range of ambient ISM density. Nevertheless, it is widely observed that spiral galaxies have a large-scale, coherently structured magnetic field of strength in the range 1–30 μG (Beck, 2001; Tabatabaei, F. S. *et al.*, 2008; Fletcher *et al.*, 2011*a*). Thus, it is plausible that SN remnants evolve subject to the magnetic effects described here, which could have significant implications on pressure support, mass loading of the galactic halo, and generally the multiphase and vertical structure of the ISM.

Part IV

Summary and Supplementary material

Chapter 6

Summary

6.1 Conclusions

The main aim of this Thesis is exploring the possible effects of magnetic fields on the gas dynamics within galaxies. I explore these effects by analysis of pre-existing ISM simulations, which model a region of a spiral galaxy such as the Milky Way or M51. The simulation presented here, and similarly by Gressel *et al.* (2008); Gressel *et al.* (2013); Bendre *et al.* (2015), differ from the majority of other such simulations in that a weak seed magnetic field is evolved, via *dynamo action*, and consistently with the gas dynamics in the simulated ISM, while other simulations use a strong initial magnetic field with *a priori* assumptions about the strength and spatial configuration of the fully-evolved magnetic field[1]. In general, we find that simulations with a strong initial magnetic field leads to no qualitative change to gas dynamics on scales larger than dense molecular clouds (Mac Low *et al.*, 2005*a*; de Avillez & Breitschwerdt, 2005; Hill *et al.*, 2012; Girichidis *et al.*, 2016). Simulations with *dynamo-evolved* magnetic fields find a number of qualitative changes to the simulated ISM which arise from the self-consistent evolution of the model.

Here I summarise some of the main results arising from the work presented in this Thesis. In Chapter 3, I find that the large-scale magnetic field avoids hot gas, particularly larger hot gas structures spanning hundreds of parsec, and prefer to reside in the warm gas. The fractional volume of warm gas increases as the magnetic field

[1]Fully-evolved refers to the magnetic field in non-linear (or saturated) phase of dynamo action.

becomes dynamically significant, which indicates that there may be magnetic feedback on gas dynamics, leading to a greater fractional volume of the phase preferred by the large-scale magnetic field. Moreover, I find that the magnetic field strength does not have a monotonic vertical distribution, with the maximum strength gradually moving away from the midplane to $|z| \sim 300\,pc$ as the magnetic field becomes dynamically significant. This is particularly intriguing, since the prevalent assumption has been that the maxima of magnetic field strength is at the midplane[2] (Cox, 2005). This assumption has previously indicated that the magnetic pressure gradient is expected to be an additional pressure support throughout the galactic disc, whereas the non-monotonic vertical distribution suggests that:

- The dynamo-active region is likely to close to the midplane but is transport away from the midplane by a process (or processes) which need to be investigated further.
- Magnetic pressure gradient may behave differently than previous expectations.

In Chapter 4, I explocre the dynamical role played by the magnetic field in the simulated ISM. The Early[3] stage of the model features large hot gas structures with span hundreds of parsec both horizontally and vertically, with the vertical distribution of gas density being disrupted noticeably. In the Late stage[4], hot gas structures are much smaller due to magnetic confinement of hot gas, and the hot gas is typically more dense than in the Early stage.

In addition, the gas density become more homogenous within the disc, with smaller variation in gas density within 300 pc of the midplane. The pre-dominant factor is the non-monotonic vertical distribution of the magnetic field strength. Below the maxima (at 300 pc), magnetic pressure gradient acts against outflow, which reduces mean vertical velocity and alters the gas density profile. Conversely, magnetic pressure gradient changes sign and provides pressure support alongside thermal pressure gradient. Even though magnetic pressure is orders of magnitude smaller than other pressure terms in the Early stage, it is in equipartition (above 300 pc) with thermal pressure in the Late stage.

The results presented in these two chapters lead to three immediate questions:

[2]This is close to the midplane and within the galactic disk. It is expected that magnetic field strength increasesfor $|z| > 1$ kpc.

[3]This corresponds to the kinematic phase of the dynamo.

[4]This refers to the non-linear phase of the dynamo.

1. What is the transport process by which magnetic field is transported from the midplane?
2. What is the relative importance of differential rotation rate and shear rate?
3. The nature of hot gas structures change both qualitatively (or even visibly) and quantitatively, even at the level of individual structures. Could this be, perhaps partially, due to a modification of SN remnants in the presence of a dynamically significant magnetic field?

I will briefly discuss Questions 1 and 2 in Section 6.2. Unfortunately, I have not been able to address these questions within the time-scale of my doctoral research, owing to the computational expense of the numerical simulations necessary. However, I plan to continue working on these simulations.

In Chapters 5 , I begin to address Question 3[5]. I explore the evolution of individual SN remnants in both HD and MHD simulations using the Pencil code, with an idealised uniform background gas density.

I run the SN simulations with a plane-parallel uniform magnetic field with varying strengths. In the presence of such a large-scale magnetic field (for $B_0 \geq 3\mu$G), I find a number of changes in the evolution and properties of the SN remnant:

1. The SN shock propagates faster perpendicular to the magnetic field, while it is in agreement with the HD (and Cioffi *et al.* (1988)) model in the paralle direction. In addition, the core of the remnant is magnetically confined perpendicular to the magnetic field. These effects are caused or at least initiated by magnetic pressure gradient at the SN shock.
2. While magnetic fields affect momentum injection marginally in quantitative terms (for field strengths up to 5μG), they alter the way in which momentum is injected since inward momentum injection and the subsequent inward shedding of mass from the SN shock are only found in the MHD remnants.
3. Confinement of the remnant core is due to inward momentum injection from the SN shock, which is not seen in the HD model or the weak magnetic field models. This confinement of the core results in reduced adiabatic cooling of the hot gas in the core, as well as an increase in the density of the gas. Moreover,

[5]I say 'begin' quite tentatively as this work has lead to a number of other questions and ideas to be explored. I will outline these in Section 6.2.

this leads to a significant change in the fractional volume of hot gas. These results are also found in simulations of the ISM reported by Evirgen *et al.* (2019).

4. The presence of a large-scale magnetic field also inhibits the formation of dense regions of cold gas.

5. For field strengths above 3μG, more energy is retained by the system by up to 10%. This comprises additional thermal and magnetic energy. In the presence of a strong magnetic field, kinetic energy retention is reduced marginally.

6.2 Future work

6.2.1 ISM simulations

Dr Frederick Gent and I are working on running new ISM simulations to address a number of questions which originate from Gent (2012) and the results presented here in Chapters 3 and 4.

Differential rotation and shear rate

I would like to run an identical set up to that presented by Gent (2012) and vary the differential rotation and shear rates separately, focusing particularly on saving snapshots of the data more frequently in the kinematic phase of the dynamo, as well as the non-linear phase, in order to be able to analyse the turbulent transport coefficients with more data.

An additional focus would be the effect of the aforementioned parameter changes on the time-evolution and spatial configuration of the magnetic field, as well as the vertical and multi-phase structure of the ISM. These simulations will require months of intensive computation, if run in parallel, millions of hours of CPU time, and up to 200 TB of storage space. For these reasons, I focused on questions which could feasibly answered within the scope of my doctoral research.

Taller simulation box

The current vertical extent of the simulation domain does not allow modelling of the galactic halo. We plan to run new simulations which extend the vertical extent up to $|z| = 2.5\,\mathrm{kpc}$, potentially using a non-uniform computational grid vertically.

Cosmic Rays

We are also working on including CRs in our ISM simulations, which provide an important pressure term in galaxies, and are closely aligned with galactic magnetic fields.

6.2.2 SN simulations

I feel that these simulations have only scratched the surface, so to speak, and I have a number of ideas for subsequent simulations.

Inhomogeneous background gas density

Kim & Ostriker (2015) find that an inhomogeneous background density does not have a noticeable effect on momentum injection by an individual SN remnant. However, I would like to perform a similar experiment with an inhomogeneous background density, even if only as a quick check.

Interacting shocks

Shocks, commonly created by SN explosions, are ubiquitous in the ISM, and they interact quite readily. I am very interested in applying the ideas and analysis explored in Chapters 5 and 6 to simulations of interacting SN shocks.

Vertical stratification

Another aspect which is not captured by the current simulations is that there is no vertical stratification in gas density. I plan to run new SN simulations in a stratified,

inhomogeneous medium.

Appendix A

Effects of random magnetic fields on supernova explosions

In this Section, I use an identical numerical set up as presented in Chapter 5, and include a small-scale, random magnetic field component. I have included these results as an appendix, rather than a main chapter, as these are very preliminary results. I present the results, as I think they are interesting. However, there remain a number of aspects which need to be analysed and understood further.

The magnetic field is represented by

$$\boldsymbol{B} = \boldsymbol{B_0} + \boldsymbol{b_0},$$

where $\boldsymbol{B_0} = (0, B_0, 0)$ and $\boldsymbol{b_0}$ is a Gaussian random field. I fix $B_{\rm rms} = 5\mu$G for all MHD models presented here, for direct comparability of results. The following models are considered:

- HD model - as a reference
- Model **B5** - Large-scale field only, $B_0 = 5\mu$G - for comparison with effects of a purely large-scale magnetic field
- Model **b5** -Random field only, $b_0 = 5\mu$G - to assess the effects of a purely random magnetic field
- Model **B2b1** - $B_0 = 4.47\mu$G, $b_0 = 2.23\mu$G - Mean to random field in ratio 1 : 2

- Model **B1b2** - $B_0 = 2.23\mu$G, $b_0 = 4.47\mu$G - Mean to random field in ratio 2 : 1

The purely large-scale and purely random field simulations are included to isolate the effects on SN remnants. The latter simulation, where $B_0/b_0 = 1/2$ is of particular interest, since we expect the random field strength to be dominant in a spiral disk.

A.1 SN profiles

A.1.1 Remnant radius

Figure A.1 shows the time profiles of SN remnant radius perpendicular, $R_\perp$, and parallel, $R_\parallel$, to the large-scale magnetic field. The models presented in the figure are the HD model, and MHD models.

Models which have a large-scale component have a faster shock perpendicular to the large-scale field. The large-scale component of B2b1 is very close to that of B5, and subsequently their $R_\perp$ profiles are very similar. However, in both B2b1 and B1b2 the perpendicular shock is slower than B5 despite being faster than the HD shock. In the parallel direction, B5, B2b1 and B1b2 have the same $R_\parallel$ profile as the HD model. Interestingly, the perpendicular and parallel profiles are identical for the b5 model, which are identical to the HD profile up until 1 Myr. After this time, both $R_\perp$ and $R_\parallel$ diverge from the HD profile, with the shock propagating more slowly through the surrounding gas.

This indicates that presence of a random, small-scale magnetic field slows the shock down, and that the local ratio of large to small scale field strength could be another important factor in deciding the shape of the remnant.

A.1.2 Radial profiles

Figure A.2 shows the radial profiles of gas density and temperature. The HD remnant and the purely random magnetic field remnant have almost identical profiles.

Models featuring a large-scale component show the changes to remnant profile discussed in Chapter 5. As the large-scale to random field strength ratio increases, the

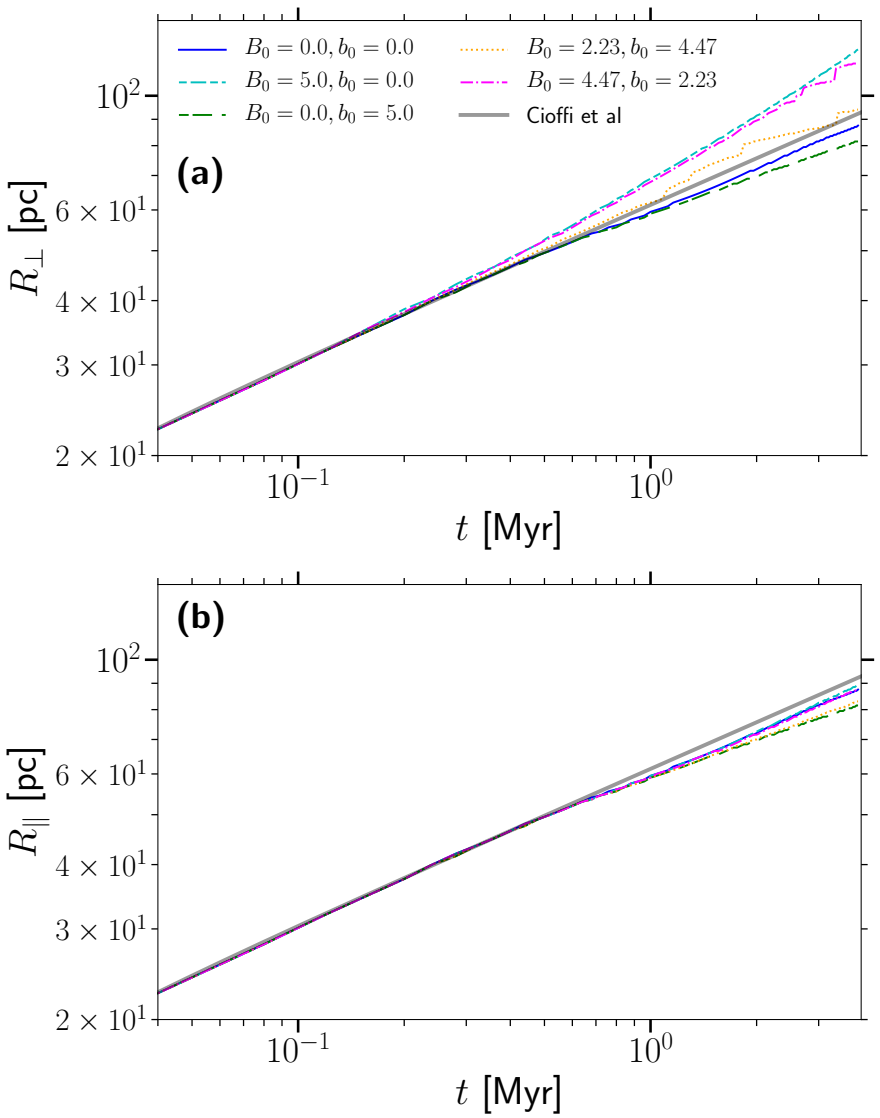

Figure A.1: Time profiles of SN remnant radius **(a)** perpendicular, $R_\perp$, and **(b)** parallel, $R_\parallel$, to the large-scale magnetic field.

differences from the HD remnant profile increase. However, the large-scale component does not need to be dominant. The model in which the random component is twice as strong as the large-scale component features a changed SN aspect ratio, higher temperatures in the core and an enhanced gas density profile behind the SN shock.

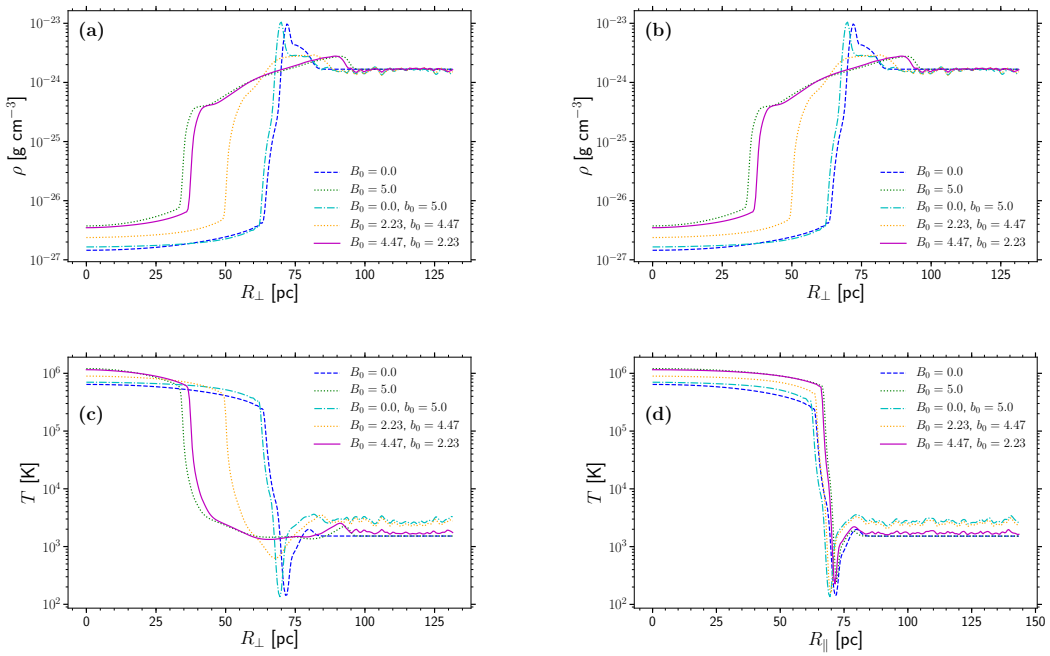

Figure A.2: Radial profiles of gas density (top row) and temperature (bottom row), perpendicular (left column) and parallel (right column) to the large-scale magnetic field, 2 Myr into remnant evolution.

A.2 Energy injection into the surrounding gas

Another aspect discussed in Chapter 5 is the energy injection by the supernova remnant into the surrounding gas. For a purely large-scale magnetic field, I find that thermal energy retention is marginally more efficient after 500 kyr into the evolution of the remnant.

Figure A.3(a) shows the energy retention (after excluding initial magnetic energy). While the overall energy decays as the SNr evolves in HD and B5 models, the b5 and B1b2 models show an increasing trend very early in the evolution of the remnant, approximately up to 30 kyr. The B2b1 model has a slightly higher energy retention than the HD and B5 model consistently until 1 Myr. All models which include a random magnetic field begin to lose energy rapidly close to 1 Myr. This can be explained by Panel (a) which shows $\Delta E_{\rm mag}(t) = E_{\rm mag}(t) - E_{\rm mag}(t=0)$. It is possible that the SN shockwave destroys local random magnetic field, and converts its energy into thermal energy, while pre-existing large-scale magnetic field is amplified by the shock. Magnetic energy, $E_{\rm mag}$, is defined as

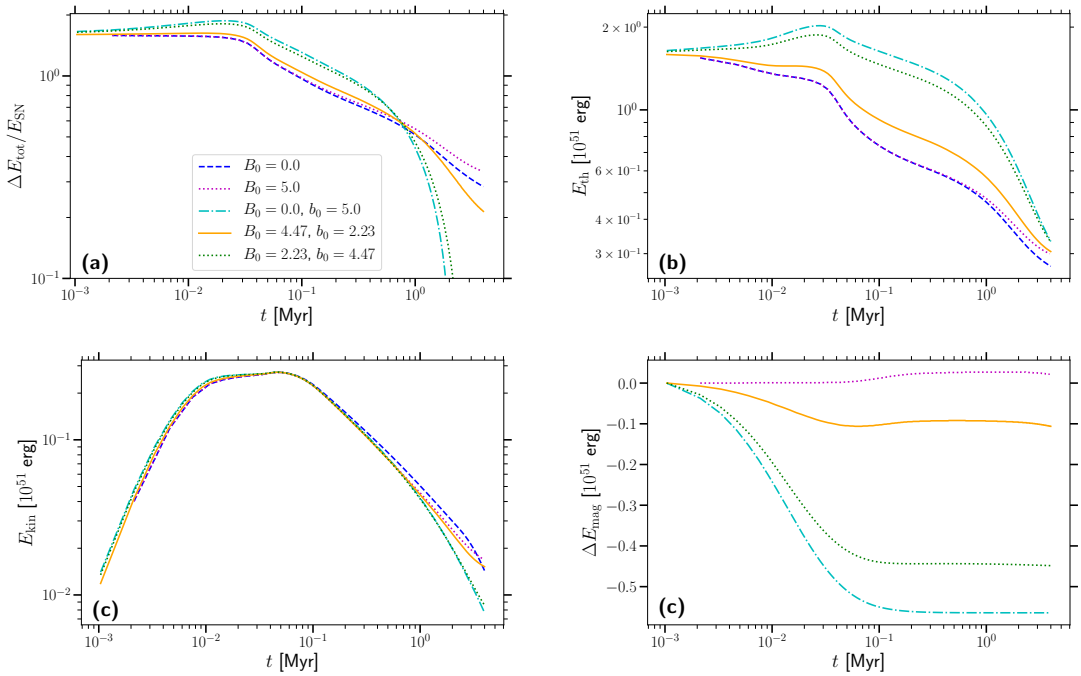

Figure A.3: Time profiles of **(a)** thermal **(b)** kinetic **(a)** magnetic energy.

$$E_{\rm mag} = \int_{\rm V} \frac{|\boldsymbol{B}|^2}{2\mu_0} {\rm dV}.$$

For the initial set up, this can be expressed as

$$E_{\rm mag} = N_x N_y N_z \frac{B^2}{2\mu_0} (\Delta x)^3,$$

where B is the initial magnetic field strength; N_x, N_y and N_z are the number of grid points in the x, y, and z directions, respectively; Δx is the spatial resolution of the model. If we have two initial magnetic field strengths, B_2 and B_1 such that $k = B_2/B_1$, then we have $E_2 = k^2 E_1$. The purely large-scale magnetic field has a large-scale component strength of 5μG, which corresponds to 6×10^{50} erg initial magnetic energy within the simulation volume. The other MHD models with a large-scale component have large-scale strengths of 2.23μG and 4.47μG, which give $k = 0.446$ and $k = 0.894$, respectively. These values indicate that these two models will have a large-scale component 20% and 80% of the purely large-scale field, corresponding to 1.2×10^{50} erg and 4.8×10^{50} erg. Models b5, B2b1 and B1b2 are shown to have lost almost all of the energy stored in the random component

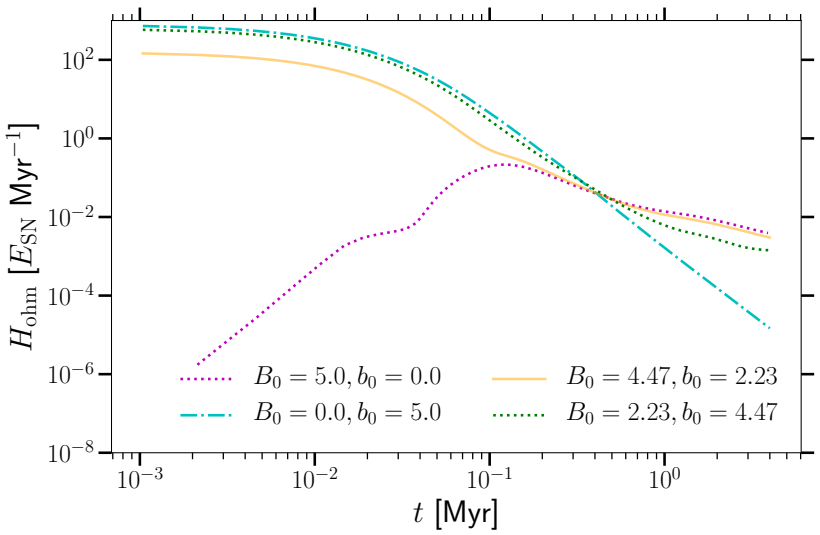

Figure A.4: Time profile of Ohmic heating for MHD SN remnant models.

of their field. However, models which feature a mixture of large-scale and random magnetic fields reach a steady magnetic field strength after an initial decay stage, corresponding to the energy stored in the large-scale component of the magnetic field.

Panel (c) shows that kinetic energy is very similar for all models in the early stage of SNr evolution, whereas Panel (b) shows that there is a significantly higher energy thermal energy retention for the models featuring random magnetic fields, in the early stage of remnant evolution in particular. Given that this effect is not seen in the HD model, a possible explanation for the initial increase in thermal energy, and ensuing increased thermal energy retention, in the presence of a random magnetic field is Ohmic heating, which features in the heat equation (Eq. (2.3)) as $\eta\mu_0\boldsymbol{j}^2$. I use the quantity, $H_{\rm Ohm}$, which is Ohmic integrated over the volume of the simulation domain:

$$H_{\rm ohm} = \int_{\rm V} \eta\mu_0\boldsymbol{j}^2 {\rm dV}.$$

Figure A.4 shows strong Ohmic heating in the models featuring random magnetic fields within the first 500 kyr of remnant evolution. All MHD models which feature a large-scale magnetic component converge to the same Ohmic heating profile in their late evolution, which indicates that the initial Ohmic heating phase can be attributed to presence of random magnetic field. In the presence of a purely random magnetic

field, Ohmic heating continues to decay after 500 kyr, which is the time at which other MHD models converge to the same time profile for Ohmic heating.

This suggests that local random magnetic field could be destroyed, with its magnetic energy being converted into thermal energy via Ohmic heating. Large-scale fields also contribute Ohmic heating but to a smaller extent.

A.3 Momentum injection

Figure A.5 shows the total and outward momentum for HD and MHD models. Both total and outward momentum are consistently higher for models featuring a random magnetic field component than the model with a purely large-scale magnetic field. In the early stage of remnant evolution, models with a random magnetic field component inject more momentum than HD remnants in total and in the outward direction.

n f In Model B2b1, momentum injection is only marginally greater than the HD and B5 models, with all three models reaching approximately 4×10^5 $M_\odot$ km s^{-1}. The b5 and B1b2 models inject 4.2×10^5 $M_\odot$ km s^{-1} momentum, 5% more than the HD model. Moreover, the presence of a random magnetic field enhances momentum injection within 100 kyr of the SN explosion. Models B1b2 and B2b1, despite having the same total magnetic energy, have a different momentum injection profile. This suggests that the ratio of large-scale to random magnetic field is also important to determining the effect of magnetic fields on momentum injection by a remnant.

Far from magnetic fields not playing a significant role in momentum injection by remnants, it seems that they might play both a significant and subtle part. While the heat equation includes magnetic effects via Ohmic heating, the Lorentz force is likely to be the factor which modifies momentum injection by the SN remnant.

Lorentz force

The Lorentz force, $\rho^{-1}\boldsymbol{j} \times \boldsymbol{B}$, is the only term in the momentum equation (Eq. (2.2)) which relates directly to the magnetic field. It is very possible that thermal change due to the magnetic field could influence momentum injection *indirectly*. However, these are highly nonlinear terms which require further, dedicated work beyond the

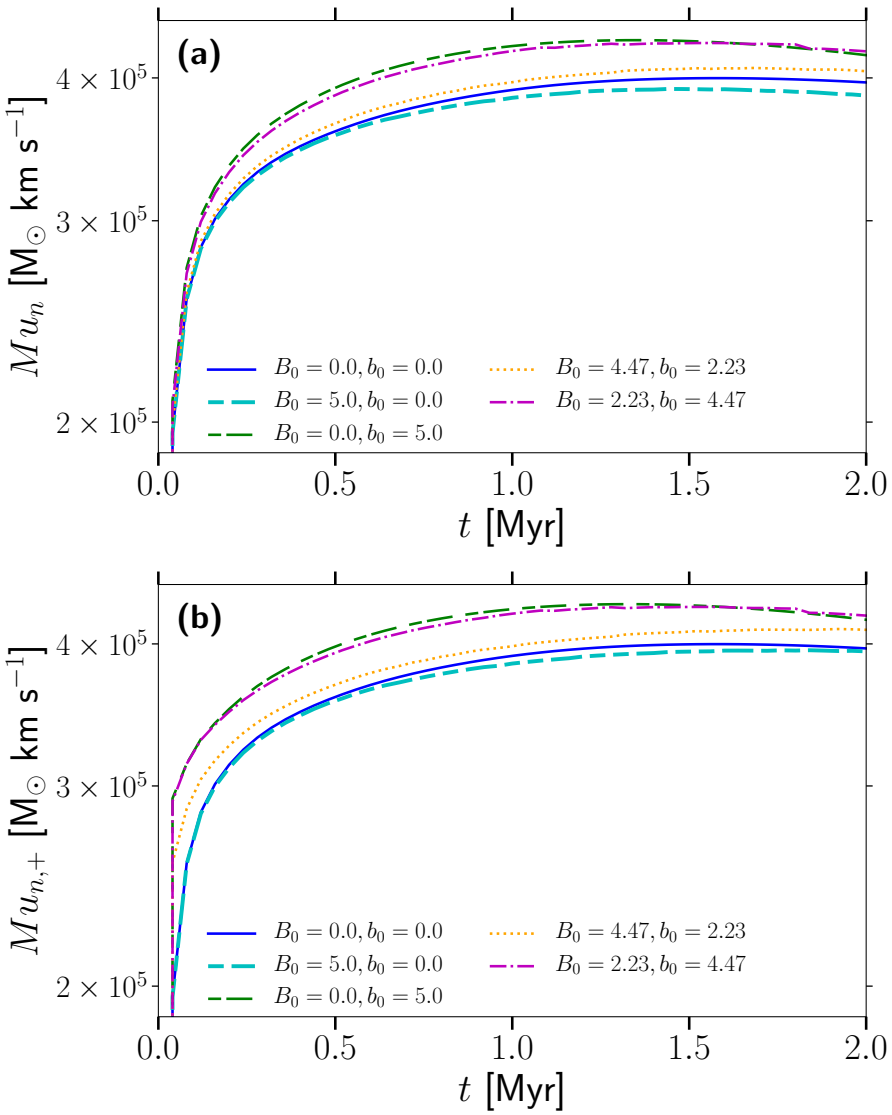

Figure A.5: Time profiles of **(a)** total and **(b)** outward momentum injection by the SN remnant models given in the figure legend.

scope of the current work. Perhaps more importantly, it is better to start by assessing the extent of a *direct* magnetic effect before focusing on other aspects.

Figure A.6 shows the magnitude of the Lorentz force, $\rho^{-1} |\boldsymbol{j} \times \boldsymbol{B}|$, throughout the evolution of the models. Lorentz force is up to two orders of magnitude higher in models featuring a random magnetic field within the first 400 kyr of SNr evolution. Interestingly, Model B1b2 is largest within this period. After this period, LOrentz force decays rapidly for Model b5, by up to three orders of magnitude. Model B2b1, where the large-scale magnetic field is dominant over the random component, decays

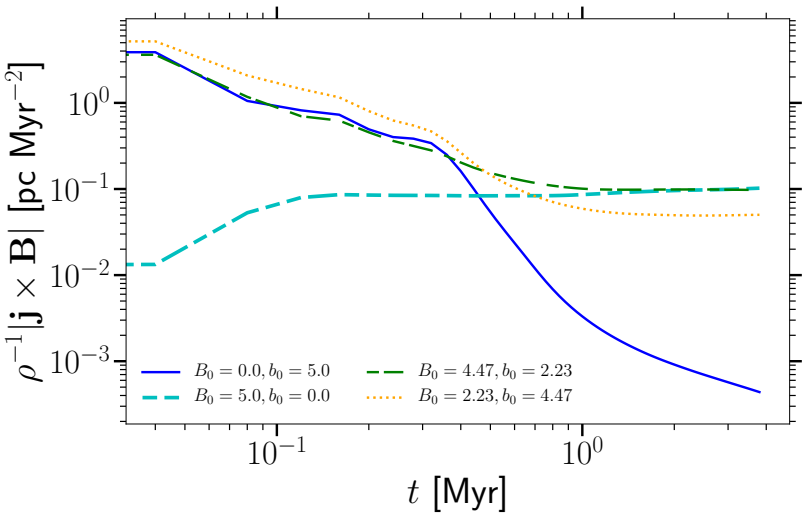

Figure A.6: Time evolution of the magnitude of the Lorentz force.

gradually and reaches the same level as B5. Model B1b2 also features a decay phase similar to Model b5 but to a lesser extent. This is very likely due to the decay of random magnetic field energy in models, particularly where the random component is dominant.

A.4 Thermodynamics of remnants

Figure A.7 shows the PDFs of gas temperature and density at different times in the evolution of the remnants. The most striking feature at 400 kyr is that the HD and B5 model have an identical peak at $T \sim 2100$ K, whereas this peak is at $T \sim 6000$ K for Model b5. Model B1b2 has a very similar peak to b5, albeit at a marginally lower temperature, whereas the peak for Model B2b1 is located between the HD (and B5) and the b5 peak. Given that the B5 model, which only features a large-scale magnetic field, is not affected by this initial shift in warm gas temperature, this shift in peak is very likely due to Ohmic heating. Otherwise, the temperature and density distributions are very similar at this stage of the models. The only other noteworthy feature is that the B5 model inhibits the formation of dense regions of gas, as discussed in the previous chapter.

By 1 Myr, the gas at the $T \sim 6000$ K peak (for models with random magnetic components) cools and has shifted to $T \sim 3000$ K, probably since Ohmic heating

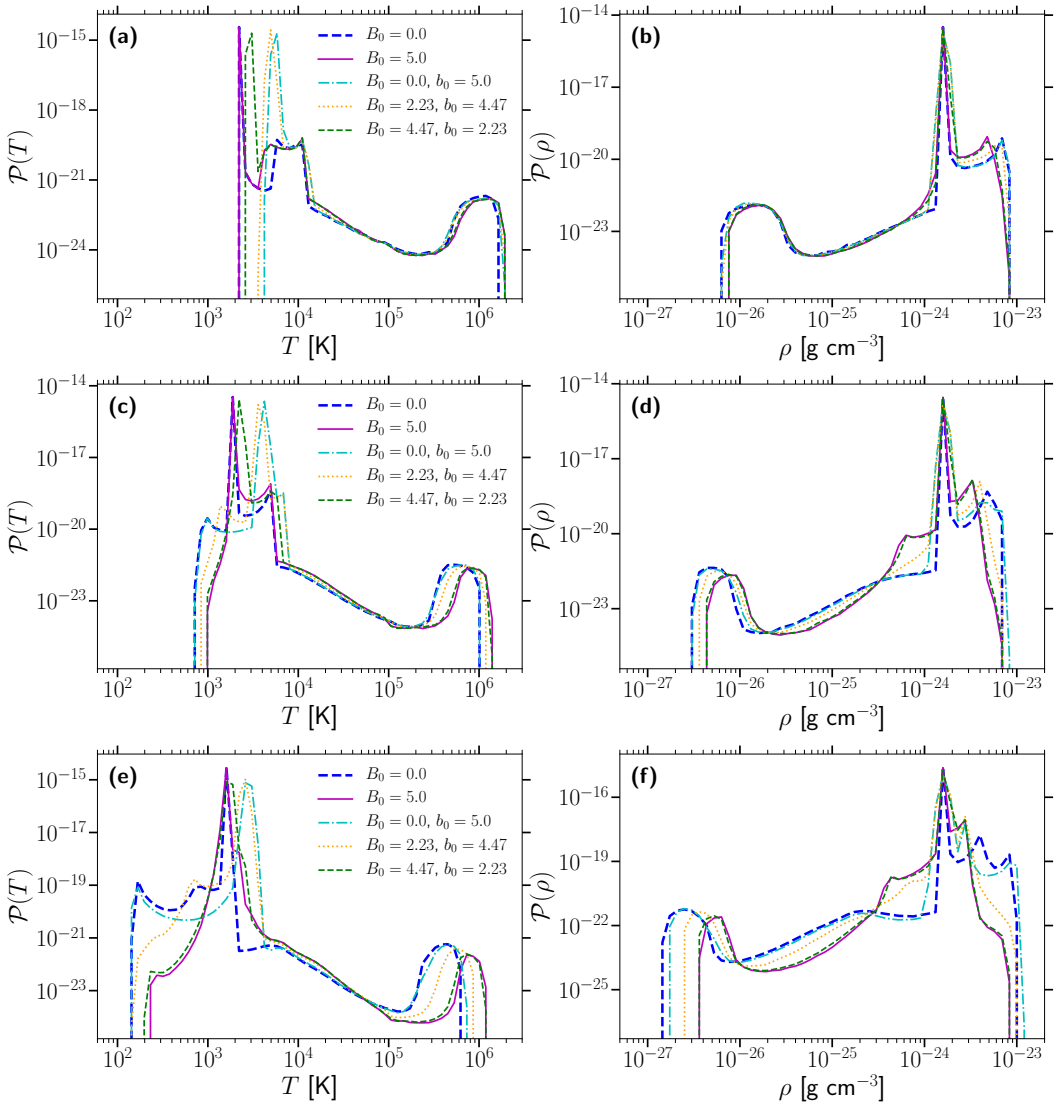

Figure A.7: PDFs of gas temperature (left column) and gas density (right column) at 400 kyr (top row), 1 Myr (middle row), and 2 Myr (bottom row).

contributes very little after 500 kyr for all models.

The HD and b5 (purely random magnetic field) models have very similar (if not identical) distributions for cold and hot gas. The random magnetic field does not inhibit the formation of cold, dense gas, It also does not keep the hot gas at higher temperatures later on in the evolution of the remnant, unlike the large-scale magnetic field.

Figure A.8(a) shows that hot gas density for the HD and b5 models are very similar, with hot gas in Model b5 becoming marginally more dense after 1 Myr. The

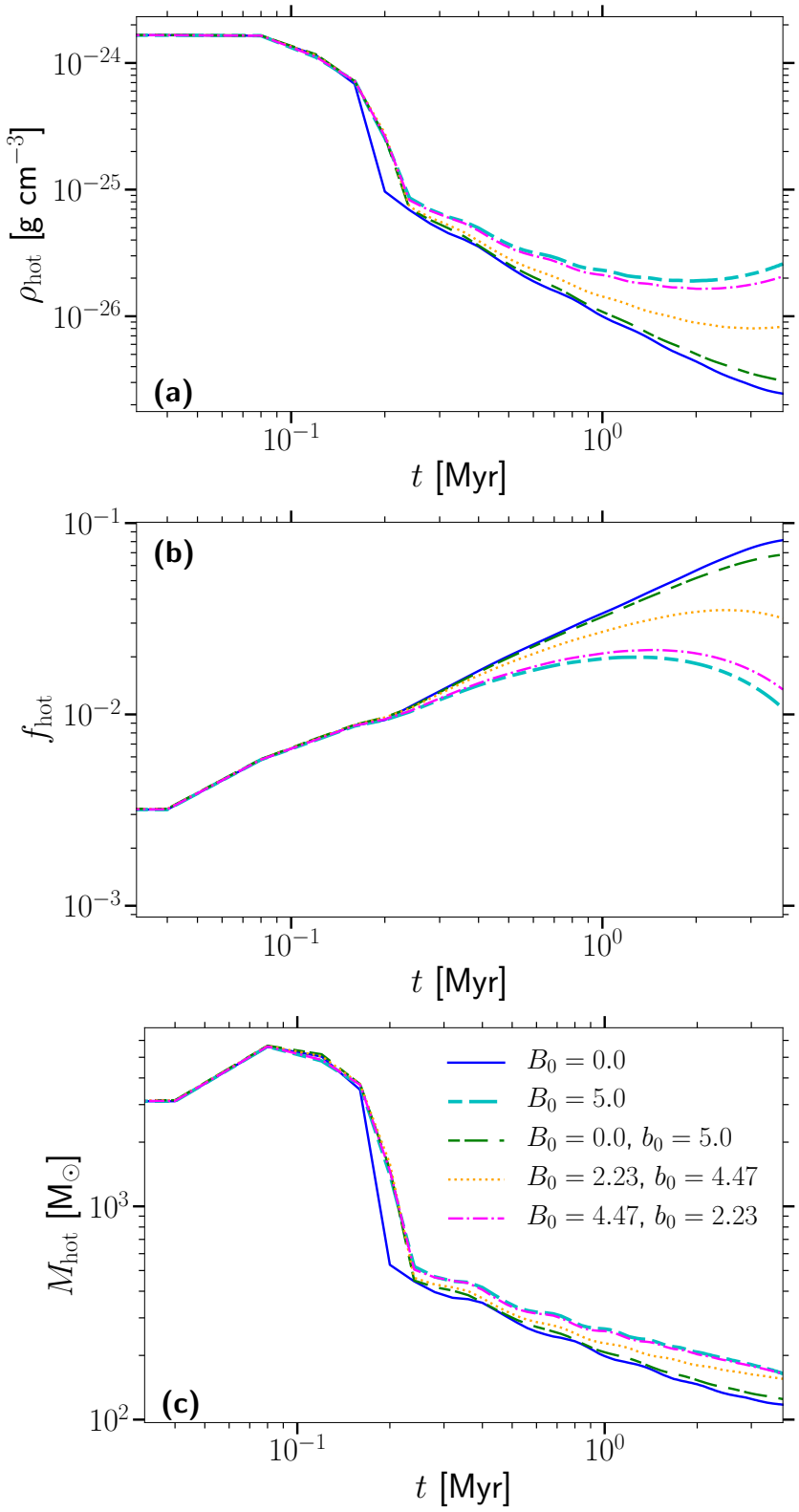

Figure A.8: Time profile of **(a)** Median density **(b)** fractional volume, and **c** mass of hot gas.

enhancement of hot gas density is clearly due to the presence of the large-scale field. A similar effect is seen for the fractional volume of hot gas and mass of hot gas, indicating that the majority of effects on hot gas are due to the large-scale field. The exception to this is that Ohmic heating is much stronger in the early stage of SN evolution for stronger random magnetic field components.

A.5 Summary

While large-scale magnetic effects become noticeable after a few hundred kyr, the effects of random fields are seen from an earlier stage of SN remnant evolution. I find that:

1. There is an initial increase in thermal energy where random fields are present, due to enhanced Ohmic heating, which is not found for large-scale magnetic fields.
2. Momentum injection is enhanced by the presence of random fields by 5%.
3. A purely random magnetic field is not found to affect the aspect ratio of the remnant, the properties of hot gas (any more than marginally). It also does not inhibit the formation of cold dense gas. These effects can be attributed to the presence of a large-scale magnetic field.

Appendix B

Comparing averaging methods

I seek to provide an example to demonstrate the important differences between the mean and fluctuating fields as obtained from horizontal averaging and Gaussian smoothing. Gent *et al.* (2013) show that both the large-scale and random magnetic fields obtained with different averaging procedures grow exponentially at different rates at the kinematic stage of the dynamo action. This difference is important as the growth rate is one of the key parameters used to compare theory with simulations. Horizontal (or volume) averaging interprets any variation of a physical variable in a horizontal plane (or the whole volume) as a fluctuation, and thus underestimates the magnitude of the mean part. Since the relative contributions of the mean and fluctuating parts change with time, this affects the rate of change inferred. In this section, we discuss differences between the spatial distributions of the mean and fluctuating outflow velocities obtained from horizontal averaging (denoted $U_{\mathrm{h},z}$ and $u_{\mathrm{h},z}$ for the mean velocity and the fluctuations, respectively) and Gaussian smoothing (with the notation $U_{\ell,z}$ and $u_{\ell,z}$).

The x–profiles of the total, mean and fluctuating vertical velocities at fixed y and z are shown in Fig. B.1. We note that the velocity is small in magnitude at $x < 0$ for this snapshot. However, there is a region of larger positive vertical velocity at $x > 0$. Under horizontal averaging, the mean vertical gas velocity is $U_{\mathrm{h},z} \approx 20\,\mathrm{km\,s^{-1}}$ throughout the plane (Fig. B.1b), whereas the Gaussian smoothing reveals a region of about 200 pc in size where systematic outflow speed reaches 40–80 $\mathrm{km\,s^{-1}}$. Even more significantly, as shown in Fig. B.1a, horizontal averaging implies local inflow in a broad region at $-0.5 \lesssim x \lesssim 0.1\,\mathrm{kpc}$, whereas such local inflows are much weaker

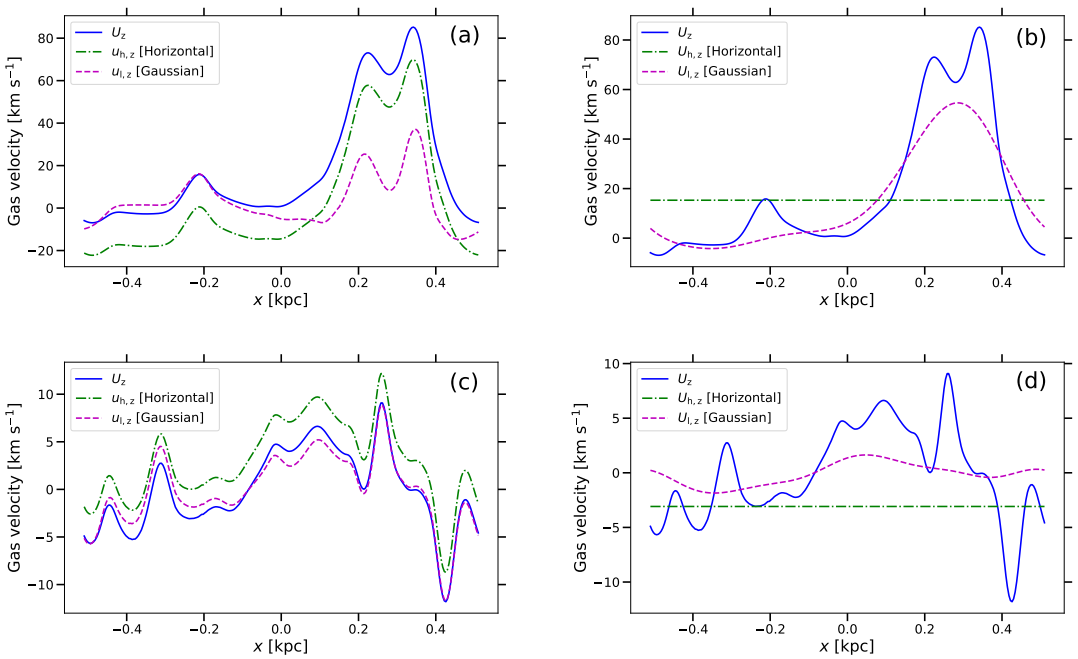

Figure B.1: The vertical component of gas velocity as a function of x (galactocentric radius) at fixed y and z, obtained under horizontal averaging and Gaussian smoothing. **(a)**: The total vertical gas velocity u_z (blue, solid) and the random vertical velocity inferred using horizontal averaging $u_{\mathrm{h},z}$ (green, dash-dotted) and Gaussian smoothing $u_{\ell,z}$ (purple, dashed). **(b)**: the total vertical gas velocity (blue, solid) and the mean vertical velocity from horizontal averaging $U_{\mathrm{h},z}$ (green, dash-dotted) and Gaussian smoothing $U_{\ell,z}$ (purple, dashed. Panels (c) and (d) present the same variables in the same format but for another time in the system evolution.

and occupy a much smaller region under Gaussian smoothing. Such differences can affect strongly the interpretation of the outflow dynamics, and we believe that Gaussian smoothing provides a more appealing physical picture.

Similar differences can be seen in Figs B.1c,d that represents another snapshot in the system evolution. Here the mean vertical velocity inferred using horizontal averaging is about $-3\,\mathrm{km\,s^{-1}}$ whereas Gaussian smoothing implies $U_{\ell,z}$ weakly varying around zero. The fluctuation parts have similar spatial distributions but different magnitudes.

Figure B.2 shows the vertical distribution of root-mean-square random velocity, as calculated using Gaussian smoothing and horizontal averaging, in Panels (a) and (b), respectively. In the kinematic (Early) stage, featuring stronger systematic outflows, the inferred random velocity is consistently larger under horizontal averaging. In

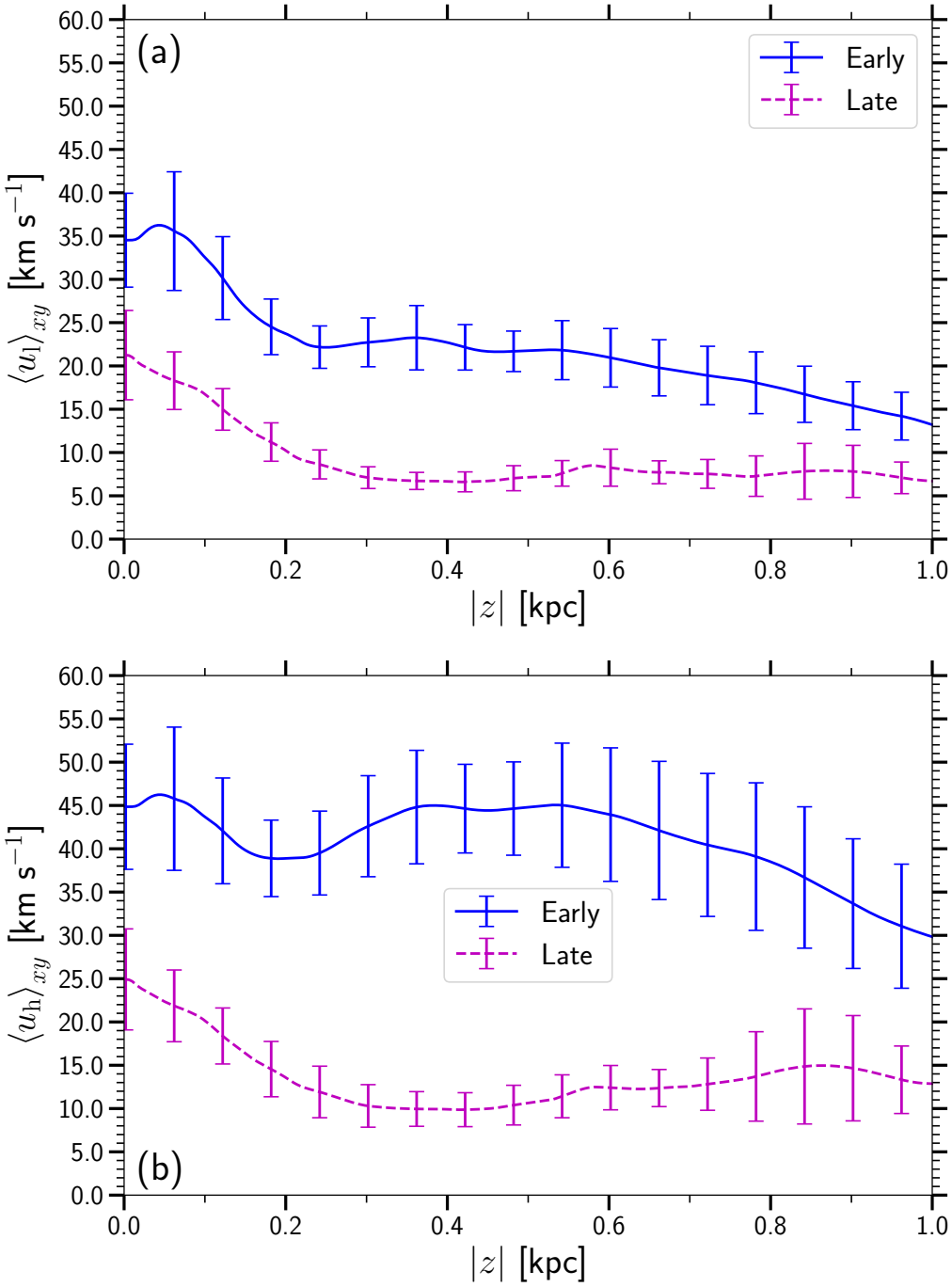

Figure B.2: Vertical profile of rms random velocity calculated at each altitude z, using **(a)** Gaussian smoothing, $\langle u_\ell^2 \rangle_{xy}^{1/2}$ and **(b)** horizontal averaging, $\langle u_\mathrm{h}^2 \rangle_{xy}^{1/2}$, for the Early (solid, blue) and Late (dashed, magenta) stages of evolution, when magnetic field is negligible and dynamically significant, respectively.

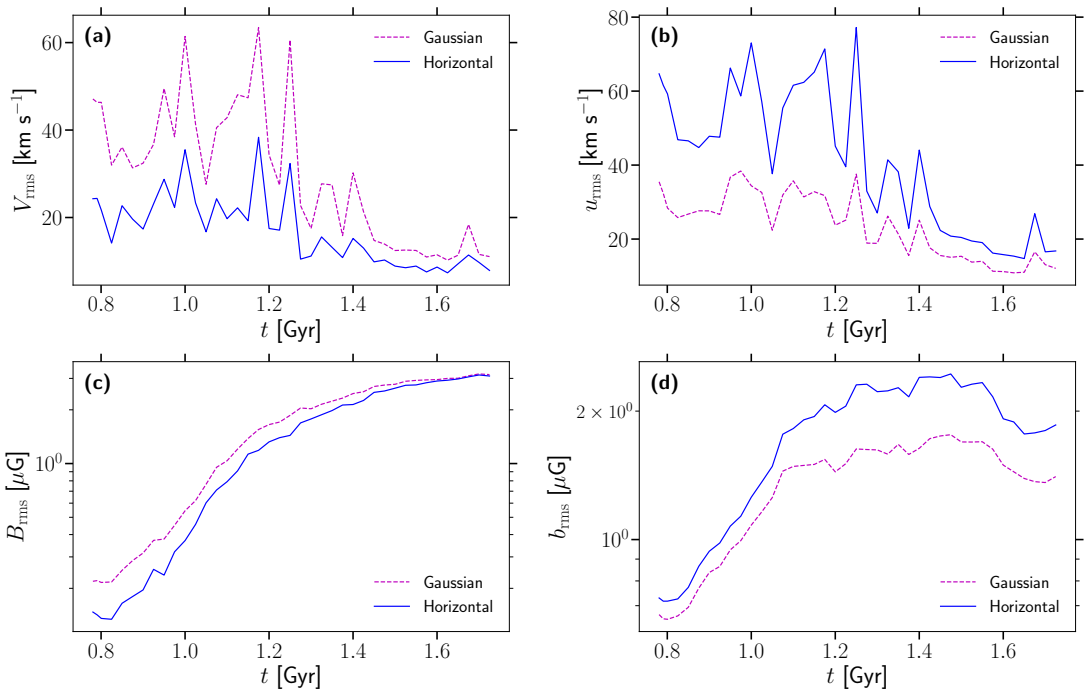

Figure B.3: Time evoution of the volume averages of rms **(a)** large-scale velocity, $V_{\rm rms}$, **(b)** turbulent velocity, $u_{\rm rms}$, **(c)** large-scale magnetic field strength, $B_{\rm rms}$, and **(d)** random magnetic field strength, $b_{\rm rms}$, calculated using both Gaussian smoothing (magenta dashed) and horizontal averaging (blue solid).

the non-linear stage of magnetic field evolution, the vertical distributions of the random velocity are similar for both averaging methods. The similarity between the vertical distributions in the non-linear stage can be explained by the reduction in the strength of the perturbations perpendicular to the horizontal plane in the non-linear stage (see Evirgen *et al.*, 2019).

Figure B.3 shows the evolution of rms values for the mean and random magnetic field and velocity field for the ISM simulations. These are called separately using Gaussian smoothing and horizontal averaging. Mean velocity obtained using Gaussian smoothing is consistently higher than that obtained using horizontal averaging, whereas the opposite is true for the turbulent velocity.

For the mean magnetic field, Gaussian smoothing produces a larger rms value until 1.5 Gyr. However, both averaging methods converge to the same value. On the other hand, horizontal averaging estimates the random magnetic field to be consistently higher than that obtained using Gaussian smoothing. This convergence to the same value for the mean-field is because the total magnetic field becomes more strongly

aligned with the azimuthal direction, making the magnetic field more strongly parallel to the midplane. Since horizontal averaging makes the inherent assumption that a mean field is uniform within the averaging plane, it is plausible that it converges the profile obtained using Gaussian smoothing, which captures large-scale structure more reliably, and without imposing a strong spatial assumption on the mean-field. This also explains why the random magnetic field has a higher rms value when calculated using horizontal averaging; while the total magnetic field is less planar, horizontal averaging treats systematic magnetic field which is not in the plane as a deviation from the mean-field, or random field. Subsequently, the rms value is inflated in comparison with Gaussian smoothing.

Appendix C

The momentum equation

The z-component of the Navier-Stokes equation, neglecting dissipation, and the continuity equation are given by

$$\partial_t U_z = -\left(\boldsymbol{U}\cdot\nabla\right)U_z - \frac{1}{\rho}\partial_z p_{\rm th} + \frac{1}{4\pi\rho}\left[\boldsymbol{j}\times\boldsymbol{B}\right]_z + g_z \tag{C.1}$$

$$\partial_t \rho = -\nabla\cdot\left(\rho\boldsymbol{U}\right), \tag{C.2}$$

where vertical gravitational acceleration, g_z, due to stellar and dark halo matter follows Kuijken & Gilmore (1989), and

$$\frac{1}{4\pi}\boldsymbol{j}\times\boldsymbol{B} = \frac{1}{4\pi}(\boldsymbol{B}\cdot\nabla)\boldsymbol{B} - \nabla\left(\frac{|\boldsymbol{B}|^2}{8\pi}\right), \tag{C.3}$$

Equations C.1 and C.2 can be combined into

$$\begin{aligned}\partial_t\left(\rho U_z\right) = &-\left[\rho\left(\boldsymbol{U}\cdot\nabla\right)U_z + U_z\nabla\cdot\left(\rho\boldsymbol{U}\right)\right] - \partial_z p_{\rm th}\\ &+\frac{1}{4\pi}\left[\boldsymbol{j}\times\boldsymbol{B}\right]_z + \rho g_z.\end{aligned}$$

We then use the identity

$$\nabla\cdot\left(\rho U_z\boldsymbol{U}\right) = \rho\left(\boldsymbol{U}\cdot\nabla\right)U_z + U_z\nabla\cdot\left(\rho\boldsymbol{U}\right),$$

to obtain

$$\partial_t\left(\rho U_z\right) = -\nabla\cdot\left(\rho U_z\boldsymbol{U}\right) - \partial_z p_{\rm th} + \frac{1}{4\pi}\left[\boldsymbol{j}\times\boldsymbol{B}\right]_z + \rho g_z.$$

Now, we substitute the z-component of Equation C.3 into this equation:

$$\begin{aligned}\partial_t\left(\rho U_z\right) =& \rho g_z - \partial_z\left(p_{\mathrm{th}} + \frac{|\boldsymbol{B}|^2}{8\pi}\right) \\ &+ \frac{1}{4\pi}(\boldsymbol{B}\cdot\nabla)B_z - \nabla\cdot\left(\rho U_z \boldsymbol{U}\right)\end{aligned} \tag{C.4}$$

This equation is horizontally averaged to give

$$\begin{aligned}\partial_t\left(\langle\rho U_z\rangle\right) = \langle\rho g_z\rangle - \partial_z\left(\langle p_{\mathrm{th}}\rangle + \left\langle\frac{|\boldsymbol{B}|^2}{8\pi}\right\rangle\right) \\ + \left\langle\frac{1}{4\pi}(\boldsymbol{B}\cdot\nabla)B_z\right\rangle - \langle\nabla\cdot\left(\rho U_z\boldsymbol{U}\right)\rangle\,.\end{aligned}$$

The following term is expanded, which gives

$$\begin{aligned}\langle\nabla\cdot\left(\rho U_z\boldsymbol{U}\right)\rangle = \langle\partial_x\left(\rho U_z U_x\right)\rangle + \langle\partial_y\left(\rho U_z U_y\right)\rangle \\ + \left\langle\partial_z\left(\rho U_z^2\right)\right\rangle\,.\end{aligned}$$

However, horizontal averages of x and y derivatives are zero due to periodic boundary conditions in x and y. Thus, we have

$$\langle\nabla\cdot\left(\rho U_z\boldsymbol{U}\right)\rangle = \partial_z\left(\left\langle\rho U_z^2\right\rangle\right)\,.$$

Substituting this term into Equation C.4 produces

$$\begin{aligned}\partial_t\left(\langle\rho U_z\rangle\right) = \langle\rho g_z\rangle - \partial_z\left(\langle p_{\mathrm{th}}\rangle + \left\langle\frac{|\boldsymbol{B}|^2}{8\pi}\right\rangle\right) \\ + \left\langle\frac{1}{4\pi}(\boldsymbol{B}\cdot\nabla)B_z\right\rangle - \partial_z\left(\left\langle\rho U_z^2\right\rangle\right)\,.\end{aligned} \tag{C.5}$$

Appendix D

Fitting a time profile for SNr radii

The time evolution of the parallel and perpendicular radii of the SN remnants can be approximated well using a linear regression fit for $\log(R(t)/R_0) = \alpha \log(t/t_0)(+c)$, where R_0 is a fit parameter representing a characteristic SN radius, t_0 is a characteristic time length and c is a fit parameter indicating the intercept of the linear fit. The latter is subsumed by the R_0 parameter, and thus the profile can be represented by

$$R(t) = R_0 t^{\alpha}.$$

While linear regression is well-established, with many numerical robust implementations available, it is also possible to user a simpler approach. If we take the (t, R) pair at two times: (t_1, R_1) and (t_2, R_2), such that $R_1 = R_0 t_1^{\alpha}$ and $R_2 = R_0 t_2^{\alpha}$, we can use

$$\frac{R_2}{R_1} = \left(\frac{t_2}{t_1}\right)^{\alpha},$$

to calculate

$$\alpha = \frac{\log(R_2/R_1)}{\log(t_2/t_1)}.$$

The known values can then be substituted into either pair to obtain

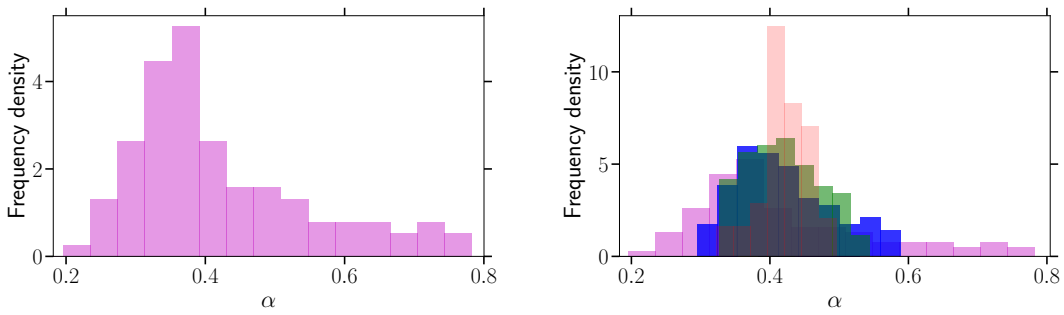

Figure D.1: The frequency density histogram for fitted alpha values using successive points only (left panel), and using window length 1 (magenta), 2 (blue), 3 (green) and 10 (shaded red) in the right panel.

$$R_0 = \frac{R_i}{t_i^\alpha}.$$

I prefer this method in this particular case, as it can be applied 'locally' for two successive points in time, which renders the method more sensitive to subtle changes in local rate. One issue that I have had with fitting a straight line to the 'log-log' equation presented at the beginning of this Appendix is that a single straight line (albeit one which minimises the error) is fitted to a cluster of points. In Figure 5.3, it is reasonable to use the assumption that a single linear fit to the log-log plot will suffice for $B_0 < 3\mu$G. However, particularly for $B_0 = 5\mu$G, the log-log plot seems subtly non-linear in the later stages for $R_\perp$.

I use the $R_\perp(t)$ profile for $B_0 = 5\mu$G as an example and calculate the parameters using directly successive points (t_i, R_i) and (t_{i+1}, R_{i+1}). It is also possible to use points further apart, for example (t_i, R_i) and (t_{i+5}, R_{i+5}). I call this example a window of length five, since the point pair used to calculate the parameters are separated by five data points in time. This has an effect analogous to using a moving average (or kernel smoothing) on noisy data (or signals). Using directly succesive points in time are susceptible to 'local noise' whereas using greater time separation focuses on the trend in the data. In reference to the actual $R_\perp$ profile, the trend is immediately discernible to the human eye[1] but the numerical method is 'fooled' by small-scale noise in the trend at a much smaller scale. The resulting histogram of fitted alpha values is provided in Figure D.1 shows the result of using

[1] and brain, which employ far more sophisticated image analysis than the author.

a window of one alone in the left panel. The estimates of *alpha* have a wide spread between 0.2 and 0.8, which is of little use. However, the right panel shows the result with windows of different length, which are more tightly distributed around 0.4. The values reported in Table 5.1 have all been calculated using this method. However, I would like to state tentatively that this is an educated guess informed by a lot of number-crunching. I believe that more precise values should come from arguments based on the underlying physics. I plan to pursue this in future work.

Calculating SNr shock speed

Once the time profile for $R(t)$ has been calculated, it is straightforward to calculate the shock speed, $v_{\rm sh}(t) \equiv \dot{R}(t)$:

$$\dot{R}(t) = \alpha R_0 t^{(\alpha-1)}.$$

However, given the variability of the actual value of α at different times in the evolution of the remnant, I use direct numerical differentiation of $R(t)$ to calculate $v_{\rm sh}(t)$.

Appendix E

Testing effects of physical parameters on SN simulations

E.1 Effects of changing diffusivity

To verify that the significant qualitative effects I identify from the MHD blast waves are attributable to the physics rather than the numerics, I examine the impact of employing artificial diffusivities compared to the impact of a magnetic field on the solutions. For numerical economy I use a set of 1D shock-tube tests. The numerical solutions for adiabatic shocks with parameters relevant to SN blast waves are compared to the system originally described by Sod (1978), and its exact analytical solution derived by Hawley *et al.* (1984). I extend the analysis applied to the HD solutions of Gent *et al.* (2019) to consider specifically whether MHD or numerical effects account for the differences in the MHD solutions

Figure E.1 shows that for an adiabatic shock the HD numerical solution reliably produces the analytic solution. Even the MHD solution has only marginally enhanced gas density in the shock. Hence, neither numerical parameters nor the presence of the magnetic field have a significant effect on the solution in the adiabatic system, and this is consistent with most previous assessments.

I next consider the effect radiative cooling and UV heating on the shock-tube solution. In Figure E.2 the non-adiabatic HD and MHD numerical solutions are contrasted to the adiabatic analytic solution. I do not have a non-adiabatic analytic

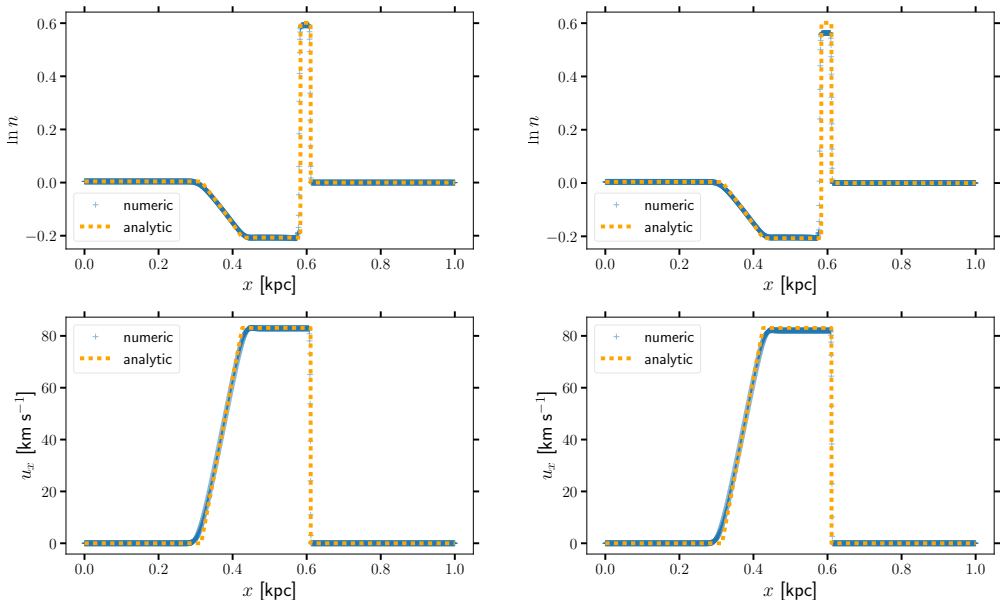

Figure E.1: Shock-tube simulations for HD (left panels) and MHD (right panels) with ν and η as applied to the 3D simulations. The spatial resolution is 0.5 pc. The MHD simulation features a 5μG uniform magnetic field perpendicular to the shock tube. Upper panels show log gas number density and lower panels gas velocity at $t = 1$ Myr.

shock-tube solution. The inclusion of cooling and heating processes has a noticeable effect on both HD and MHD shock tubes; both shocks propagate more slowly through the ambient gas. This is not unexpected, since these processes extract energy which would otherwise be used up in the propagation of the shock. I note that the MHD shock propagates faster than the HD shock, as also seen in the 3D simulations presented in this Paper. The gas density behind the shock tube is higher than the standard set up for both HD and MHD shock tubes with cooling and heating. However, as seen in the 3D simulations, the gas density is higher behind the shock for the MHD shock tube. In addition, the shock density is lower in the MHD shock. This is evidence that the nonlinear interaction between the MHD and non-adiabatic effects is a significant factor in the divergence of the HD and MHD solutions.

For the 1D shock-tube tests an artificial shock-dependent mass diffusion is unnecessary, but I include it in these experiments to verify that its inclusion in SN-driven turbulence simulations does not induce excessive numerical diffusion. I consider a range of mass shock diffusivity $\zeta_{\rm D} \in [0, 10] f_{\rm shock}$. From Figure E.3 I show that adding mass diffusion, while providing numerical stability, produces a minor quantitative difference in the gas density shock profile. The profiles are otherwise qualitatively

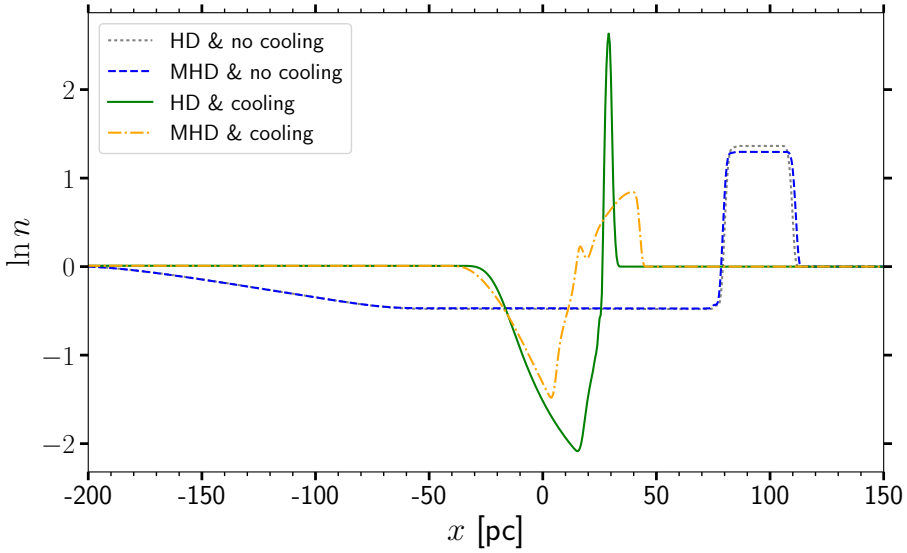

Figure E.2: Comparison of the numerical non-adiabatic HD and MHD shock-tube solutions, alongside the adiabatic analytic solution.

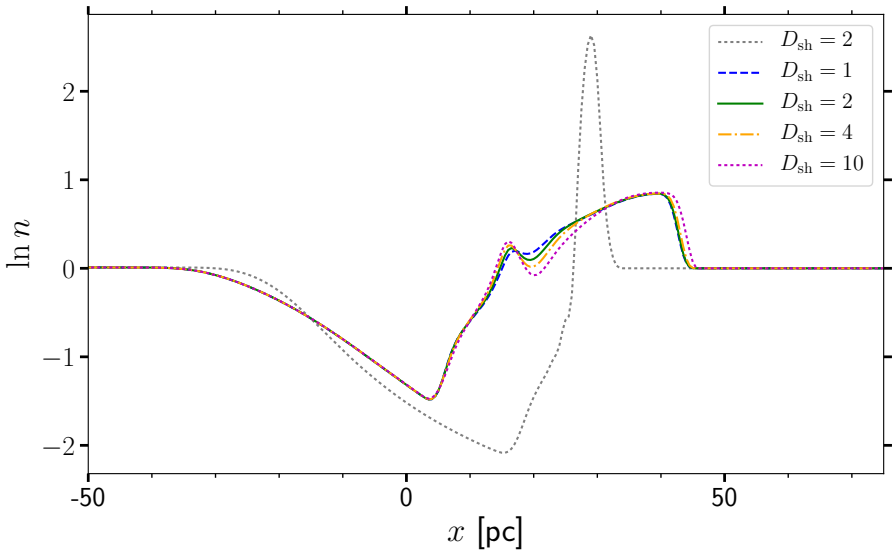

Figure E.3: The non-adiabatic MHD shock-tube solution is contrasted with the HD solution (gray dashed) for a range of mass diffusion rates, $\zeta_D = [0, 2, 4, 10] f_{shock}$.

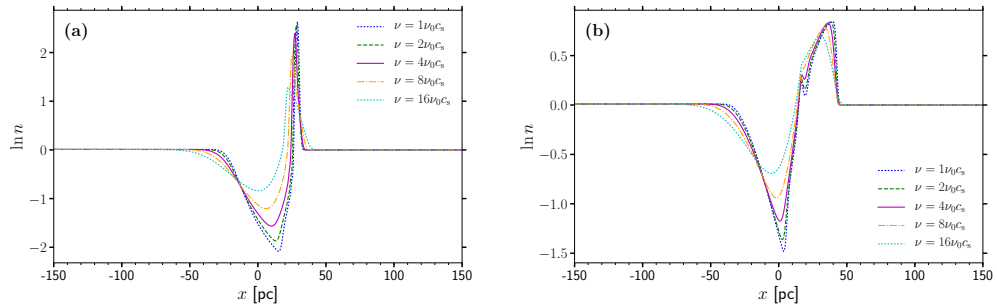

Figure E.4: HD (left) and MHD (right) non-adiabatic shock-tube solutions for $\nu \in [\nu_0, 2\nu_0, 4\nu_0, 8\nu_0, 16\nu_0]$.

the same and the contrast with the HD profile is clearly down to the presence of the magnetic effects rather than the mass diffusion. A remaining concern is that the broadening of the mass profile in the MHD blast wave may arise from the high value of the viscosity, $\nu = \nu_0$ with $\nu_0 = 0.0005 c_s \,\mathrm{kpc\,km\,s^{-1}}$ in the 3D SN blast waves. Although the estimates of microscopic viscosity in the real ISM are orders of magnitude lower, the viscosity in the model represents instead a turbulent viscosity. To model turbulence I require this dissipation scale applies above the grid scale, but sufficiently below the SN forcing scale to accurately capture the energy spectrum down to the smallest scales of interest in the model. I vary $\nu = [\nu_0, 2\nu_0, 4\nu_0, 8\nu_0, 16\nu_0]$ with $\zeta_\mathrm{D} = 2 f_\mathrm{shock} \,\mathrm{kpc\,km\,s^{-1}}$ and $\eta = 0.0008 \,\mathrm{kpc\,km\,s^{-1}}$ for the non-adiabatic 1D shock-tube tests. This also effectively changes the magnetic Prandtl number in the MHD simulations, defined as $\mathrm{P_m} = \nu/\eta$, which yields $\mathrm{P_m} = [0.625, 1.25, 2.5, 5, 10]\,\mathrm{c_s}$. Given that in these solutions $c_s \gg 1 \,\mathrm{km\,s^{-1}}$, I also have $\mathrm{P_m} \gg 1$

Some resulting density profiles are shown in Figure E.4. Both HD and MHD are affected similarly by increasing viscosity. The shock front does not propagate as fast for higher values of ν and the region behind the shock is smoothed. However both HD and MHD shocks are not affected qualitatively as viscosity is increased. The difference between the HD and MHD solutions cannot be explained by high diffusivity.

E.2 Changing the ambient gas density

There is a significant change to the HD SN evolution when a moderately strong uniform magnetic field is embedded in the ambient ISM. I conclude that this is in

part due to the alteration of the radiative cooling and UV-heating characterstics in response to the retrograde flow of gas into the remnant. The cooling and heating profile of the ISM is highly sensitive to the gas density and temperature. I would like to explore the response to varying ambient ISM density in the 3D MHD SN remnant evolution in future work, but here I perform a preliminary low budget experiment with 1D shock-tube tests of varying ambient gas density. I apply ambient gas number density, $n_0 = 10^{-2}, 10^{-1}, 1, 10, 100\,\mathrm{cm}^{-1}$ to assess whether the magnetic effects described in this Paper may be generalised beyond $1\,\mathrm{cm}^{-3}$. The range of densities chosen reflect the range from diffuse, hot gas to dense, cold gas. The initial entropy of the ambient gas is adjusted such that the ambient temperature remains constant with net heating at zero appropriate to the initial gas density. Specfic gas entropy is expressed as

$$s = c_\mathrm{V} \left[\ln T - (\gamma - 1) \ln \rho\right],$$

with T and ρ expressed in dimensionless code units, $\gamma = 5/3$ is the adiabatic index, and c_V is the specific heat capacity. Some initial configuration is represented by T_0, ρ_0 and,

$$s_0 = c_\mathrm{V} \left[\ln T_0 - (\gamma - 1) \ln \rho_0\right].$$

I change the gas density such that $\rho_1 = k\rho_0$, where $k > 0$, but keep the temperature constant, such that $T_0 = T_1$. The two entropies, the new entropy s_1 can be related to the old value s_0:

$$\begin{aligned} s_1 &= s_0 + c_\mathrm{V}(\gamma - 1) \left[\ln \rho_0 - \ln k\rho_0\right], \\ s_1 &= s_0 + c_\mathrm{V}(1 - \gamma) \ln k. \end{aligned} \tag{E.1}$$

I use this expression to change gas density while keeping initial temperature constant. In Figure E.5, I present the time profiles of distance travelled by the non-adiabatic shock (analogous to remnant shell radius) for a range of ambient gas densities. The effect of the magnetic field is measured by the difference between the profiles for HD and MHD shocks of identical ambient gas density. As in the 3D SN simulations, divergence of the MHD shock profile from the HD profile indicates the effect of magnetic field. I find that the effect of the magnetic field increases as the ambient density becomes more diffuse, due to decreasing plasma-β. Magnetic effects are seen for all ambient densities apart from $n = 100$ cm^{-3}. Magnetic effects

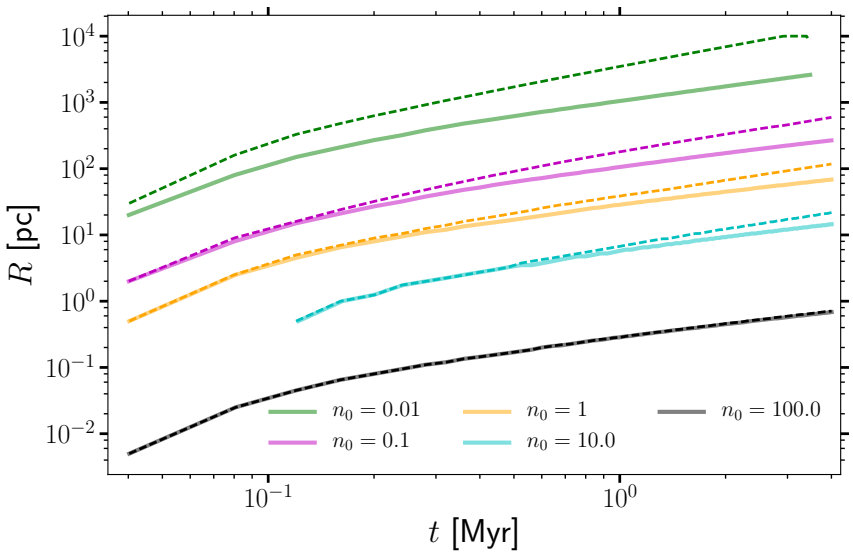

Figure E.5: Shock radius for 1D non-adiabatic MHD shock-tube simulations ($B_0 = 5\mu$G), for a range of ambient gas densities. Solid lines indicate the profiles for HD models at the given background density, while dashed lines of the same colour represent MHD models of the same background density.

appear earlier in the lower ambient gas densities.

E.3 Effect of choice of cooling function

I have recently been running new SN simulations, using different cooling functions. Preliminary results indicate that MHD effects with each cooling function considered. However, I need to finish running the full suite of simulations, analyse the data and then report the full results.

Bibliography

Alves, M. I. R., Boulanger, F., Ferrière, K. & Montier, L. 2018 The Local Bubble: a magnetic veil to our Galaxy. *A&A* **611**, L5.

Arshakian, T. G., Beck, R., Krause, M. & Sokoloff, D. 2009 Evolution of magnetic fields in galaxies and future observational tests with the Square Kilometre Array. *A&A* **494** (1), 21–32.

Beck, A. M., Lesch, H., Dolag, K., Kotarba, H., Geng, A. & Stasyszyn, F. A. 2012 Origin of strong magnetic fields in Milky Way-like galactic haloes. *MNRAS* **422** (3), 2152–2163.

Beck, R. 2001 Galactic and Extragalactic Magnetic Fields. *SSRv* **99**, 243–260.

Beck, R. 2007 Magnetism in the spiral galaxy NGC 6946: magnetic arms, depolarization rings, dynamo modes, and helical fields. *A&A* **470**, 539–556.

Beck, R. 2015 Magnetic fields in spiral galaxies. *A&A Rev.* **24**, 4.

Beck, R., Brandenburg, A., Moss, D., Shukurov, A. & Sokoloff, D. 1996 Galactic Magnetism: Recent Developments and Perspectives. *ARA&A* **34**, 155–206.

Beck, R., Poezd, A. D., Shukurov, A. & Sokoloff, D. D. 1994 Dynamos in evolving galaxies. *A&A* **289**, 94–100.

Bendre, A., Gressel, O. & Elstner, D. 2015 Dynamo saturation in direct simulations of the multi-phase turbulent interstellar medium. *Astron. Nachr.* **336**, 991.

Bertone, S., Vogt, C. & Ensslin, T. 2006 Magnetic field seeding by galactic winds. *MNRAS* **370** (1), 319–330.

Birnboim, Y., Balberg, S. & Teyssier, R. 2015 Galaxy evolution: modelling the role of non-thermal pressure in the interstellar medium. *MNRAS* **447** (4), 3678–3692.

Bloemen, J. B. G. M. 1987 On stable hydrostatic equilibrium configurations of the galaxy and implications for its halo. *ApJ* **322**, 694–705.

Boulares, A. 1988 High energy particles in supernova remnants and the interstellar medium. PhD thesis, Wisconsin Univ., Madison.

Boulares, A. & Cox, D. P. 1990 Galactic hydrostatic equilibrium with magnetic tension and cosmic-ray diffusion. *ApJ* **365**, 544–558.

Brandenburg, A., Korpi, M. J. & Mee, A. J. 2007 Thermal instability in shearing and periodic turbulence. *ApJ* **654**, 945–954.

Brandenburg, A. & Subramanian, K. 2005 Astrophysical magnetic fields and nonlinear dynamo theory. *Phys. Rep.* **417**, 1–209.

Breitschwerdt, D., McKenzie, J. F. & Völk, H. J. 1991 Galactic winds. I - Cosmic ray and wave-driven winds from the Galaxy. *A&A* **245**, 79–98.

Breitschwerdt, D., McKenzie, J. F. & Völk, H. J. 1993 Galactic winds. II - Role of the disk-halo interface in cosmic ray driven galactic winds. *A&A* **269**, 54–66.

Cardillo, M., Tavani, M., Giuliani, A., Yoshiike, S., Sano, H., Fukuda, T., Fukui, Y., Castelletti, G. & Dubner, G. 2014 The supernova remnant W44: Confirmations and challenges for cosmic-ray acceleration. *A&A* **565**, A74.

Caunt, S. E. & Korpi, M. J. 2001 A 3D MHD model of astrophysical flows: Algorithms, tests and parallelisation. *A&A* **369**, 706–728.

Chevalier, R. A. 1974 The Evolution of Supernova Remnants. Spherically Symmetric Models. *ApJ* **188**, 501–516.

Chevalier, R. A. & Clegg, A. W. 1985 Wind from a starburst galaxy nucleus. *Nature* **317**, 44.

Chyży, K. T. & Beck, R. 2004 Magnetic fields in merging spirals - the Antennae. *A&A* **417**, 541–555.

Cioffi, D. F., McKee, C. F. & Bertschinger, E. 1988 Dynamics of radiative supernova remnants. *ApJ* **334**, 252–265.

Cox, D. P. 2005 The three-phase interstellar medium revisited. *Annual Review of Astronomy and Astrophysics* **43** (1), 337–385.

Crutcher, R. M. 2012 Magnetic Fields in Molecular Clouds. *ARA&A* **50**, 29–63.

de Avillez, M. A. 2000 Disc-halo interaction - i. three-dimensional evolution of the galactic disc. *MNRAS* **315**, 479–497.

de Avillez, M. A. & Berry, D. L. 2001 Three-dimensional evolution of worms and chimneys in the Galactic disc. *MNRAS* **328**, 708–718.

de Avillez, M. A. & Breitschwerdt, D. 2004 Volume filling factors of the ism phases in star forming galaxies. i. the role of the disk-halo interaction. *A&A* **425**, 899–911.

de Avillez, M. A. & Breitschwerdt, D. 2005 Global dynamical evolution of the ism in star forming galaxies. i. high resolution 3d simulations: Effect of the magnetic field. *A&A* **436**, 585–600.

de Avillez, M. A. & Breitschwerdt, D. 2007 The generation and dissipation of interstellar turbulence: Results from large-scale high-resolution simulations. *ApJ* **665**, L35–L38.

de Gasperin, F., Evoli, C., Brüggen, M., Hektor, A., Cardillo, M., Thorman, P., Dawson, W. A. & Morrison, C. B. 2014 Discovery of the supernova remnant G351.0-5.4. *A&A* **568**, A107.

Deharveng, L., Zavagno, A., Samal, M. R., Anderson, L. D., LeLeu, G., Brevot, D., Duarte-Cabral, A., Molinari, S., Pestalozzi, M., Foster, J. B., Rathborne, J. M. & Jackson, J. M. 2015 Bipolar H II regions - Morphology and star formation in their vicinity. I. G319.88+00.79 and G010.32-00.15. *A&A* **582**, A1.

Duronea, N. U., Cappa, C. E., Bronfman, L., Borissova, J., Gromadzki, M. & Kuhn, M. A. 2017 Triggered massive star formation associated with the bubble Hii region Sh2-39 (N5). *A&A* **606**, A8.

Durrer, R. & Neronov, A. 2013 Cosmological magnetic fields: their generation, evolution and observation. *A&A Rev.* **21**, 62.

Elmegreen, B. G. 1993 Star Formation at Compressed Interfaces in Turbulent Self-gravitating Clouds. *ApJL* **419**, L29.

Elmegreen, B. G. & Lada, C. J. 1977 Sequential formation of subgroups in OB associations. *ApJ* **214**, 725–741.

Elstner, D., Beck, R. & Gressel, O. 2014 Do magnetic fields influence gas rotation in galaxies? *A&A* **568**, A104.

Everett, J. E., Zweibel, E. G., Benjamin, R. A., McCammon, D., Rocks, L. & Gallagher, III, J. S. 2008 The Milky Way's Kiloparsec-Scale Wind: A Hybrid Cosmic-Ray and Thermally Driven Outflow. *ApJ* **674**, 258–270.

Evirgen, C. C., Gent, F. A., Shukurov, A., Fletcher, A. & Bushby, P. 2017 The distribution of mean and fluctuating magnetic fields in the multiphase interstellar medium. *MNRAS* **464**, L105–L109.

Evirgen, C. C., Gent, F. A., Shukurov, A., Fletcher, A. & Bushby, P. J. 2019 The supernova-regulated ISM - VI. Magnetic effects on the structure of the interstellar medium. *MNRAS* **488** (4), 5065–5074.

Ferrière, K. 1996 Alpha-tensor and diffusivity tensor due to supernovae and superbubbles in the Galactic disk near the Sun. *A&A* **310**, 438–455.

Ferrière, K. 2005 The origin of galactic magnetic fields and their impact on the interstellar medium. In *The Magnetized Plasma in Galaxy Evolution* (ed. K. T. Chyzy, K. Otmianowska-Mazur, M. Soida & R.-J. Dettmar), pp. 147–155.

Ferrière, K. M. 2001 The interstellar environment of our galaxy. *Rev. Mod. Phys.* **73**, 1031–1066.

Ferrière, K. M., Mac Low, M.-M. & Zweibel, E. G. 1991 Expansion of a superbubble in a uniform magnetic field. *ApJ* **375**, 239–253.

Fletcher, A., Beck, R., Berkhuijsen, E. M., Horellou, C. & Shukurov, A. 2004 Magnetic Fields and Spiral Structure. In *How Does the Galaxy Work?* (ed. E. J. Alfaro, E. Pérez & J. Franco), *Astrophysics and Space Science Library*, vol. 315, p. 299.

Fletcher, A., Beck, R., Shukurov, A., Berkhuijsen, E. M. & Horellou, C. 2011*a* Magnetic fields and spiral arms in the galaxy M51. *MNRAS* **412**, 2396–2416.

Fletcher, A., Beck, R., Shukurov, A., Berkhuijsen, E. M. & Horellou, C. 2011*b* Magnetic fields and spiral arms in the galaxy M51. *MNRAS* **412**, 2396–2416.

Fletcher, A. & Shukurov, A. 2001 Hydrostatic equilibrium in a magnetized, warped Galactic disc. *MNRAS* **325**, 312–320.

Gatto, A., Walch, S., Naab, T., Girichidis, P., Wünsch, R., Glover, S. C. O., Klessen, R. S., Clark, P. C., Peters, T., Derigs, D., Baczynski, C. & Puls, J. 2017 The SILCC project - III. Regulation of star formation and outflows by stellar winds and supernovae. *MNRAS* **466**, 1903–1924.

Gazol-Patiño, A. & Passot, T. 1999 A Turbulent Model for the Interstellar Medium. III. Stratification and Supernova Explosions. *ApJ* **518** (2), 748–759.

Gent, F. 2012 Supernovae driven turbulence in the interstellar medium. PhD thesis, Newcastle University, `http://hdl.handle.net/10443/1755`.

Gent, F. A., Mac Low, M.-M., Käpylä, M. J., Sarson, G. R. & Hollins, J. F. 2019 Pencil-Code special edition: modelling supernova driven turbulence. *GAFD, in press* p. arXiv:1806.01570.

Gent, F. A., Shukurov, A., Fletcher, A., Sarson, G. R. & Mantere, M. J. 2013 "The supernova-regulated ISM - I. The multiphase structure. *MNRAS* **432**, 1396–1423.

Gent, F. A., Shukurov, A., Sarson, G. R., Fletcher, A. & Mantere, M. J. 2013 The supernova-regulated ISM - II. The mean magnetic field. *MNRAS* **430**, L40–L44.

Germano, M. 1992 Turbulence – The filtering approach. *J. Fluid Mech.* **238**, 325–336.

Girichidis, P., Walch, S., Naab, T., Gatto, A., Wünsch, R., Glover, S. C. O., Klessen, R. S., Clark, P. C., Peters, T., Derigs, D. & Baczynski, C. 2016 The SILCC (SImulating the LifeCycle of molecular Clouds) project - II. Dynamical evolution of the supernova-driven ISM and the launching of outflows. *MNRAS* **456**, 3432–3455.

Gressel, O., Bendre, A. & Elstner, D. 2013 On the magnetic quenching of mean-field effects in supersonic interstellar turbulence. *MNRAS* **429** (2), 967–972.

Gressel, O., Elstner, D., Ziegler, U. & Rüdiger, G. 2008 Direct simulations of a supernova-driven galactic dynamo. *A&A* **486**, L35–L38.

Hanasz, M., Lesch, H., Naab, T., Gawryszczak, A., Kowalik, K. & Wóltański, D. 2013 Cosmic Rays Can Drive Strong Outflows from Gas-rich High-redshift Disk Galaxies. *ApJL* **777** (2), L38.

Hanasz, M., Wóltański, D. & Kowalik, K. 2009 Global Galactic Dynamo Driven by Cosmic Rays and Exploding Magnetized Stars. *ApJ* **706** (1), L155–L159.

Hanayama, H. & Tomisaka, K. 2006 Long-Term Evolution of Supernova Remnants in Magnetized Interstellar Medium. *ApJ* **641**, 905–918.

Haverkorn, M. 2015 Magnetic Fields in the Milky Way. In *Magnetic Fields in Diffuse Media* (ed. A. Lazarian, E. M. de Gouveia Dal Pino & C. Melioli), p. 483. Berlin: Springer.

Hawley, J. F., Smarr, L. L. & Wilson, J. R. 1984 A numerical study of nonspherical black hole accretion. I Equations and test problems. *ApJ* **277**, 296–311.

Heiles, C. 1996 The Local Direction and Curvature of the Galactic Magnetic Field Derived from Starlight Polarization. *ApJ* **462**, 316.

Henley, D. B., Shelton, R. L., Kwak, K., Hill, A. S. & Mac Low, M.-M. 2015 The Origin of the Hot Gas in the Galactic Halo: Testing Galactic Fountain Models' X-Ray Emission. *ApJ* **800**, 102.

Hill, A. S., Joung, M. R., Mac Low, M.-M., Benjamin, R. A., Haffner, L. M., Klingenberg, C. & Waagan, K. 2012 Vertical Structure of a Supernova-driven Turbulent, Magnetized Interstellar Medium. *ApJ* **750**, 104–122.

Hollins, J. F., Sarson, G. R., Evirgen, C. C., Shukurov, A., Fletcher, A. & Gent, F. A. (in prep.) Separating the scales in a compressible interstellar medium. *arXiv e-prints* .

Hollins, J. F., Sarson, G. R., Shukurov, A., Fletcher, A. & Gent, F. A. 2017*a* Space- and time-correlations in the supernova driven interstellar medium. *ArXiv e-prints* .

Hollins, J. F., Sarson, G. R., Shukurov, A., Fletcher, A. & Gent, F. A. 2017*b* Supernova-regulated ISM. V. Space and Time Correlations. *ApJ* **850** (1), 4.

Hunter, J. H., J., Sandford, M. T., I., Whitaker, R. W. & Klein, R. I. 1986 Star Formation in Colliding Gas Flows. *ApJ* **305**, 309.

Joung, M. K. R. & Mac Low, M.-M. 2006 Turbulent structure of a stratified supernova-driven interstellar medium. *ApJ* **653**, 1266–1279.

Jun, B.-I. & Norman, M. L. 1996 On the origin of radial magnetic fields in young supernova remnants. *The Astrophysical Journal* **472** (1), 245.

Kalberla, P. M. W. & Kerp, J. 2009 The Hi Distribution of the Milky Way. *ARA&A* **47**, 27–61.

Kim, C.-G., Kim, W.-T. & Ostriker, E. C. 2006 Interstellar Turbulence Driving by Galactic Spiral Shocks. *ApJL* **649** (1), L13–L16.

Kim, C.-G. & Ostriker, E. C. 2015 Momentum Injection by Supernovae in the Interstellar Medium. *ApJ* **802**, 99.

Kim, J., Balsara, D. & Mac Low, M.-M. 2001 Turbulence Driven by Supernova Explosions in a Radiatively-Cooling Magnetized Interstellar Medium. *Journal of Korean Astronomical Society* **34**, 333–335.

Klein, U. & Fletcher, A. 2015 *Galactic and Intergalactic Magnetic Fields*.

Klein, U., Wielebinski, R. & Morsi, H. W. 1988 Radio continuum observations of M82. *A&A* **190**, 41–46.

Klessen, R. S. & Glover, S. C. O. 2016 Physical Processes in the Interstellar Medium. *Saas-Fee Advanced Course* **43**, 85.

Korpi, M. J., Brandenburg, A., Shukurov, A. & Tuominen, I. 1999*a* Evolution of a superbubble in a turbulent, multi-phased and magnetized ISM. *A&A* **350**, 230–239.

Korpi, M. J., Brandenburg, A., Shukurov, A., Tuominen, I. & Nordlund, Å. 1999*b* A Supernova-regulated Interstellar Medium: Simulations of the Turbulent Multiphase Medium. *ApJL* **514**, L99–L102.

Kotarba, H., Lesch, H., Dolag, K., Naab, T., Johansson, P. H. & Stasyszyn, F. A. 2009 Magnetic field structure due to the global velocity field in spiral galaxies. *MNRAS* **397** (2), 733–747.

Krause, F. & Wielebinski, R. 1991 Dynamos in Galaxies. *Reviews in Modern Astronomy* **4**, 260–286.

Kuijken, K. & Gilmore, G. 1989 The mass distribution in the galactic disc - ii - determination of the surface mass density of the galactic disc near the sun. *MNRAS* **239**, 605–649.

Kulsrud, R. M. 1999 A Critical Review of Galactic Dynamos. *ARA&A* **37**, 37–64.

Kulsrud, R. M., Cen, R., Ostriker, J. P. & Ryu, D. 1997 The Protogalactic Origin for Cosmic Magnetic Fields. *ApJ* **480** (2), 481–491.

Kulsrud, R. M. & Zweibel, E. G. 2008 On the origin of cosmic magnetic fields. *Reports on Progress in Physics* **71** (4), 046901.

Lazar, M., Schlickeiser, R., Wielebinski, R. & Poedts, S. 2009 Cosmological Effects of Weibel-Type Instabilities. *ApJ* **693** (2), 1133–1141.

Li, M., Bryan, G. L. & Ostriker, J. P. 2017 Quantifying Supernovae-driven Multiphase Galactic Outflows. *ApJ* **841** (2), 101.

Li, M., Li, Y., Bryan, G. L., Ostriker, E. C. & Quataert, E. 2019 The Impact of Type Ia Supernovae in Quiescent Galaxies: I. Formation of the Multiphase Interstellar medium. *arXiv e-prints* p. arXiv:1909.03138.

Loren, R. B. 1976 Colliding clouds and star formation in NGC 1333. *ApJ* **209**, 466–488.

Mac Low, M.-M., Balsara, D. L., Kim, J. & de Avillez, M. A. 2005*a* The distribution of pressures in a supernova-driven interstellar medium. i. magnetized medium. *ApJ* **626**, 864–876.

Mac Low, M.-M., Balsara, D. S., Kim, J. & de Avillez, M. A. 2005*b* The distribution of pressures in a supernova-driven interstellar medium. i. magnetized medium. *ApJ* **626**, 864–876.

Mac Low, M.-M. & Klessen, R. S. 2004 Control of star formation by supersonic turbulence. *Reviews of Modern Physics* **76**, 125–194.

Makarenko, I., Shukurov, A., Henderson, R., Rodrigues, L. F. S., Bushby, P. & Fletcher, A. 2018 Topological signatures of interstellar magnetic fields - I. Betti numbers and persistence diagrams. *MNRAS* **475**, 1843–1858.

Mao, S. A., Carilli, C., Gaensler, B. M., Wucknitz, O., Keeton, C., Basu, A., Beck, R., Kronberg, P. P. & Zweibel, E. 2017 Detection of microgauss coherent magnetic fields in a galaxy five billion years ago. *Nature Astronomy* **1**, 621–626.

McKee, C. F. & Ostriker, J. P. 1977 A theory of the interstellar medium - three components regulated by supernova explosions in an inhomogeneous substrate. *ApJ* **218**, 148–169.

Moffatt, H. K. 1978 *Magnetic field generation in electrically conducting fluids*.

Murray, N., Quataert, E. & Thompson, T. A. 2005 On the Maximum Luminosity of Galaxies and Their Central Black Holes: Feedback from Momentum-driven Winds. *ApJ* **618**, 569–585.

Niklas, S. 1995 PhD thesis, Univ. Bonn, (1995).

Nordlund, Å. & Padoan, P. 2003 *Star Formation and the Initial Mass Function*, pp. 271–298. Berlin, Heidelberg: Springer Berlin Heidelberg.

Pakmor, R., Gómez, F. A., Grand , R. J. J., Marinacci, F., Simpson, C. M., Springel, V., Campbell, D. J. R., Frenk, C. S., Guillet, T., Pfrommer, C. & White, S. D. M. 2017 Magnetic field formation in the Milky Way like disc galaxies of the Auriga project. *MNRAS* **469** (3), 3185–3199.

Paron, S. 2018 The interstellar medium: from molecules to star formation. *Boletin de la Asociacion Argentina de Astronomia La Plata Argentina* **60**, 176–182.

Passot, T., Vazquez-Semadeni, E. & Pouquet, A. 1995 A Turbulent Model for the Interstellar Medium. II. Magnetic Fields and Rotation. *ApJ* **455**, 536.

Peters, T., Banerjee, R., Klessen, R. S. & Mac Low, M.-M. 2011 The Interplay of Magnetic Fields, Fragmentation, and Ionization Feedback in High-mass Star Formation. *ApJ* **729**, 72.

Piontek, R. A., Gressel, O. & Ziegler, U. 2009 Multiphase ISM simulations: comparing NIRVANA and ZEUS. *A&A* **499**, 633–641.

Rand, R. J. & Kulkarni, S. R. 1989 The local Galactic magnetic field. *ApJ* **343**, 760–772.

Rees, M. J. 2005 *Magnetic Fields in the Early Universe*, , vol. 664, p. 1.

Reipurth, B. 1983 Star formation in BOK globules and low-mass clouds. *A&A* **117**, 183–198.

Rieder, M. & Teyssier, R. 2016 A small-scale dynamo in feedback-dominated galaxies as the origin of cosmic magnetic fields - I. The kinematic phase. *MNRAS* **457** (2), 1722–1738.

Roberts, P. H. & Soward, A. M. 1975 A unified approach to mean field electrodynamics. *Astron. Nachr.* **296**, 49–64.

Rodrigues, L. F. S., Shukurov, A., Fletcher, A. & Baugh, C. M. 2015 Galactic magnetic fields and hierarchical galaxy formation. *MNRAS* **450** (4), 3472–3489.

Rosen, A. & Bregman, J. N. 1995 Global Models of the Interstellar Medium in Disk Galaxies. *ApJ* **440**, 634.

Rosen, A., Bregman, J. N. & Kelson, D. D. 1996 Global Models of the Galactic Interstellar Medium: Comparison to X-Ray and H i Observations. *ApJ* **470**, 839.

Rosner, R. & Deluca, E. 1989 On the Galactic Dynamo. In *The Center of the Galaxy* (ed. M. Morris), *IAU Symposium*, vol. 136, p. 319.

Ruzmaikin, A. A., Shukurov, A. M. & Sokoloff, D. D. 1989 Book-Review - Magnetic Fields of Galaxies. *Journal of the British Astronomical Association* **99**, 313.

Sánchez-Salcedo, F. J., Vázquez-Semadeni, E. & Gazol, A. 2002 The Nonlinear Development of the Thermal Instability in the Atomic Interstellar Medium and Its Interaction with Random Fluctuations. *ApJ* **577**, 768–788.

Sarazin, C. L. & White, III, R. E. 1987*a* Steady state cooling flow models for normal elliptical galaxies. *ApJ* **320**, 32–48.

Sarazin, C. L. & White, III, R. E. 1987*b* Steady state cooling flow models for normal elliptical galaxies. *ApJ* **320**, 32–48.

Schlickeiser, R. & Felten, T. 2013 Strength of the Spontaneously Emitted Collective Aperiodic Magnetic Field Fluctuations in the Reionized Early Intergalactic Medium. *ApJ* **778** (1), 39.

Sedov, L. I. 1959 *Similarity and Dimensional Methods in Mechanics*. New York: Academic Press.

Shukurov, A. 2007 In *Mathematical Aspects of Natural Dynamos* (ed. E. Dormy & A. M. Soward), pp. 313–359. Chapman & Hall/CRC.

Shukurov, A., Evirgen, C. C., Fletcher, A., Bushby, P. J. & Gent, F. A. 2018 Magnetic field effects on the ISM structure and galactic outflows. *arXiv e-prints* p. arXiv:1810.01202.

Siejkowski, H., Otmianowska-Mazur, K., Soida, M., Bomans, D. J. & Hanasz, M. 2014 3D global simulations of a cosmic-ray-driven dynamo in dwarf galaxies. *A&A* **562**, A136.

Simpson, C. M., Bryan, G. L., Hummels, C. & Ostriker, J. P. 2015 Kinetic Energy from Supernova Feedback in High-resolution Galaxy Simulations. *ApJ* **809** (1), 69.

Slavin, J. D. & Cox, D. P. 1992 Completing the evolution of supernova remnants and their bubbles. *ApJ* **392**, 131–144.

Slyz, A. D., Devriendt, J. E. G., Bryan, G. & Silk, J. 2005 Towards simulating star formation in the interstellar medium. *MNRAS* **356**, 737–752.

Sod, G. A. 1978 A survey of several finite difference methods for systems of nonlinear hyperbolic conservation laws. *Journal of Computational Physics* **27**, 1–31.

Spitzer, L. 1978 *Physical processes in the interstellar medium*.

Steenbeck, M., Krause, F. & Rädler, K. H. 1966 Berechnung der mittleren LORENTZ-Feldstärke für ein elektrisch leitendes Medium in turbulenter, durch CORIOLIS-Kräfte beeinflußter Bewegung. *Zeitschrift Naturforschung Teil A* **21**, 369.

Tabatabaei, F. S., Krause, M., Fletcher, A. & Beck, R. 2008 High-resolution radio continuum survey of m 33. *A&A* **490** (3), 1005–1017.

Taylor, G. 1950 The Formation of a Blast Wave by a Very Intense Explosion. I. Theoretical Discussion. *Royal Society of London Proceedings Series A* **201**, 159–174.

Tomisaka, K. 1998 Superbubbles in magnetized interstellar media: blowout or confinement? *MNRAS* **298**, 797–810.

Tomisaka, K., Habe, A. & Ikeuchi, S. 1981 Sequential explosions of supernovae in an OB association and formation of a superbubble. *Ap&SS* **78**, 273–285.

Vazquez-Semadeni, E., Passot, T. & Pouquet, A. 1995 A Turbulent Model for the Interstellar Medium. I. Threshold Star Formation and Self-Gravity. *ApJ* **441**, 702.

Wada, K., Meurer, G. & Norman, C. A. 2002 Gravity-driven turbulence in galactic disks. *ApJ* **577**, 197–205.

Wada, K. & Norman, C. A. 2001 Numerical models of the multiphase interstellar matter with stellar energy feedback on a galactic scale. *ApJ* **547**, 172–186.

Wada, K. & Norman, C. A. 2007 Density structure of the interstellar medium and the star formation rate in galactic disks. *ApJ* **660**, 276–287.

Walch, S., Girichidis, P., Naab, T., Gatto, A., Glover, S. C. O., Wünsch, R., Klessen, R. S., Clark, P. C., Peters, T., Derigs, D. & Baczynski, C. 2015 The SILCC (SImulating the LifeCycle of molecular Clouds) project - I. Chemical evolution of the supernova-driven ISM. *MNRAS* **454**, 238–268.

Wang, P. & Abel, T. 2009 Magnetohydrodynamic Simulations of Disk Galaxy Formation: The Magnetization of the Cold and Warm Medium. *ApJ* **696** (1), 96–109.

Whitworth, A. P., Bhattal, A. S., Chapman, S. J., Disney, M. J. & Turner, J. A. 1994*a* Fragmentation of shocked interstellar gas layers. *A&A* **290**, 421–427.

Whitworth, A. P., Bhattal, A. S., Chapman, S. J., Disney, M. J. & Turner, J. A. 1994*b* The Preferential Formation of High-Mass Stars in Shocked Interstellar Gas Layers. *MNRAS* **268**, 291.

Widrow, L. M. 2002 Origin of galactic and extragalactic magnetic fields. *Reviews of Modern Physics* **74** (3), 775–823.

Wiener, J., Zweibel, E. G. & Oh, S. P. 2013 Cosmic Ray Heating of the Warm Ionized Medium. *ApJ* **767** (1), 87.

Wolfire, M. G., Hollenbach, D., McKee, C. F., Tielens, A. G. G. M. & Bakes, E. L. O. 1995*a* The neutral atomic phases of the interstellar medium. *ApJ* **443**, 152–168.

Wolfire, M. G., Hollenbach, D., McKee, C. F., Tielens, A. G. G. M. & Bakes, E. L. O. 1995*b* The neutral atomic phases of the interstellar medium. *ApJ* **443**, 152–168.

Wood, K., Hill, A. S., Joung, M. R., Mac Low, M.-M., Benjamin, R. A., Haffner, L. M., Reynolds, R. J. & Madsen, G. J. 2010 Photoionization of High-altitude Gas in a Supernova-driven Turbulent Interstellar Medium. *ApJ* **721**, 1397–1403.

Yadav, N., Mukherjee, D., Sharma, P. & Nath, B. B. 2017 How multiple supernovae overlap to form superbubbles. *MNRAS* **465**, 1720–1740.

Zavagno, A., Anderson, L. D., Russeil, D., Morgan, L., Stringfellow, G. S., Deharveng, L., Rodón, J. A., Robitaille, T. P., Mottram, J. C., Schuller, F., Testi, L., Billot, N., Molinari, S., di Gorgio, A., Kirk, J. M., Brunt, C., Ward-Thompson, D., Traficante, A., Veneziani, M., Faustini, F. & Calzoletti, L. 2010 Star formation triggered by H II regions in our Galaxy. First results for N49 from the Herschel infrared survey of the Galactic plane. *A&A* **518**, L101.

Zeldovich, Y. B. 1957 The magnetic field in the two-dimensional motion of a conducting turbulent fluid. *JETP* **4**, 460–462.

Zeldovich, Ya. B., Ruzmaikin, A. A. & Sokoloff, D. D. 1990 *The Almighty Chance*. Singapore: World Scientific.

Zirakashvili, V. N. & Ptuskin, V. S. 2008 Diffusive shock acceleration with magnetic amplification by nonresonant streaming instability in supernova remnants. *The Astrophysical Journal* **678** (2), 939.